INVESTIGATIONS OF CONDENSED MATTER BY MODERN NEUTRON SCATTERING METHODS

2015-2017 Activity Report (theme 04-4-1121-2015/2017)

Theme Code:	04-4-1121-2015/2017
Laboratory:	Frank Laboratory of Neutron Physics
Department:	Neutron Investigations of Condensed Matter (NICM)
Field of Research:	Condensed Matter Physics
Theme Title:	Investigations of Condensed Matter by Modern Neutron Scattering Methods
Leaders:	D.P.Kozlenko, V.L.Aksenov, A.M.Balagurov

ANNOTATION

The JINR basic facility — the IBR-2 high-flux pulsed reactor — is the leading Russian and one of the best neutron pulsed sources in the world. At the reactor, a suite of neutron spectrometers has been constructed and successfully employed in a wide range of fundamental and applied condensed matter investigations by neutron scattering techniques. In 2012, after completion of modernization, regular research activities and the realization of the FLNP User Program were resumed on the IBR-2 reactor. In 2012-2016, the complex of IBR-2 spectrometers has been significantly upgraded, and the number of instruments has increased from 11 to 15. The research activities using neutron scattering techniques, the operation and modernization of the spectrometer complex of the IBR-2 reactor were carried out by the employees of the FLNP NICM Department. Some experimental investigations were performed in neutron and synchrotron centers in Russia and abroad in accordance with the existing cooperation agreements and accepted beam time application proposals. The primary goals within the framework of activities on the modernization of the IBR-2 spectrometers' complex were the realization of top-priority projects aimed at constructing a new DN-6 diffractometer for studying microsamples, a multipurpose GRAINS reflectometer and modernizing the available spectrometers, as well as the development and construction of a prototype of a facility for neutron radiography and tomography.

The present report covers the period from 2015 to 2017 and provides information on the most important results of conducted scientific investigations and activities on the modernization of the IBR-2 spectrometers' complex.

1. THEME 1121: OBJECTIVES AND ORGANIZATION OF RESEARCH ACTIVITIES IN 2015 – 2017

The main objectives of research in the framework of the theme involved the application of neutron scattering techniques and complementary methods to investigate the structure, dynamics and microscopic properties of nanosystems and novel materials, which are of interest from the standpoint of fundamental investigations or of great importance for the development of nanotechnologies in the fields of electronics, pharmacology, medicine, chemistry, modern condensed matter physics and interdisciplinary sciences.

The experimental research activities conducted by the personnel of the FLNP NICM Department were carried out mainly on the spectrometers of the IBR-2 reactor. In addition, some experimental investigations were performed in neutron and synchrotron centers in Russia and abroad including steady-state and pulsed neutron sources in RRC KI, PNPI, IMP UB RAS, ISIS RAL, ILL, PSI, LLB, FRM-2, HMI, BNC, as well as synchrotron sources KSRS, ESRF and PETRA-III. This work was performed in accordance with the Topical Plan for JINR Research and International Cooperation under the existing cooperation agreements and accepted beam time application proposals.

The activities on the modernization of the IBR-2 spectrometers' complex were focused on the realization of the top priority projects aimed at constructing a new DN-6 diffractometer for studying microsamples, a multipurpose GRAINS reflectometer and modernizing the available spectrometers, as well as the development and construction of a prototype of a facility for neutron radiography and tomography.

Within the framework of investigations under the theme, the employees of the NICM Department maintained broad cooperation with many scientific organizations in JINR Member States and other countries. The cooperation, as a rule, was documented by joint protocols or agreements. In Russia, particularly active collaboration was with the thematically close organizations, such as RRC KI, PNPI, MSU, IMP UB RAS, IC RAS, INR RAS and others. A complete list of organizations cooperating with the NICM Department is given in Appendix 1.

2. FLNP DEPARTMENT OF NEUTRON INVESTIGATIONS OF CONDENSED MATTER

The NICM Department structurally consists of two sectors (Diffraction and Neutron Optics) and two groups (Small-Angle Scattering and Inelastic Scattering) (**Fig. 1**). In its turn, the Diffraction Sector comprises 4 groups (HRFD/FSD, DN-2, DN-12, SKAT/EPSILON) and the Neutron Optics Sector consists of 3 groups (REMUR, REFLEX, GRAINS). In 2016, the Department's staff comprised 101 employees; among them are 9 Doctors of Science, 36 Candidates of Science, 1 Laureate of State Prize. 34 employees are from the JINR Member States and 6 employees are by-workers. As may be seen from **Fig. 2** illustrating the age distribution of the NICM Department employees, the personnel of the Department is well balanced in age and harmoniously combines highly skilled scientists with young and middle-aged specialists.

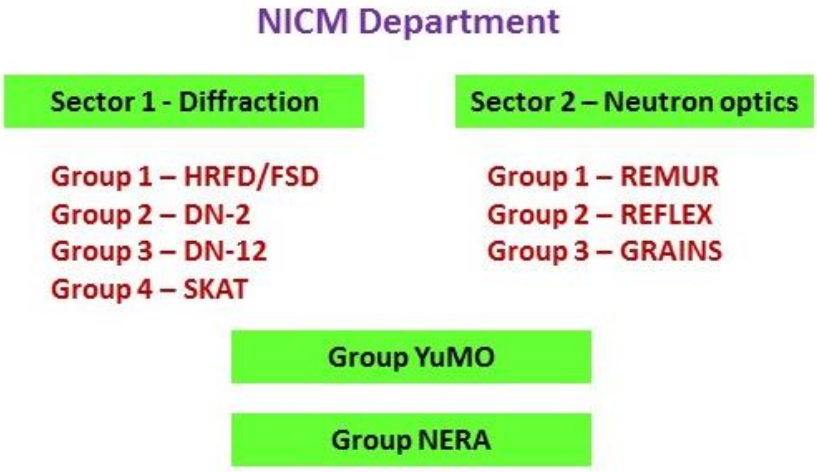

Fig. 1. Structure of the NICM Department.

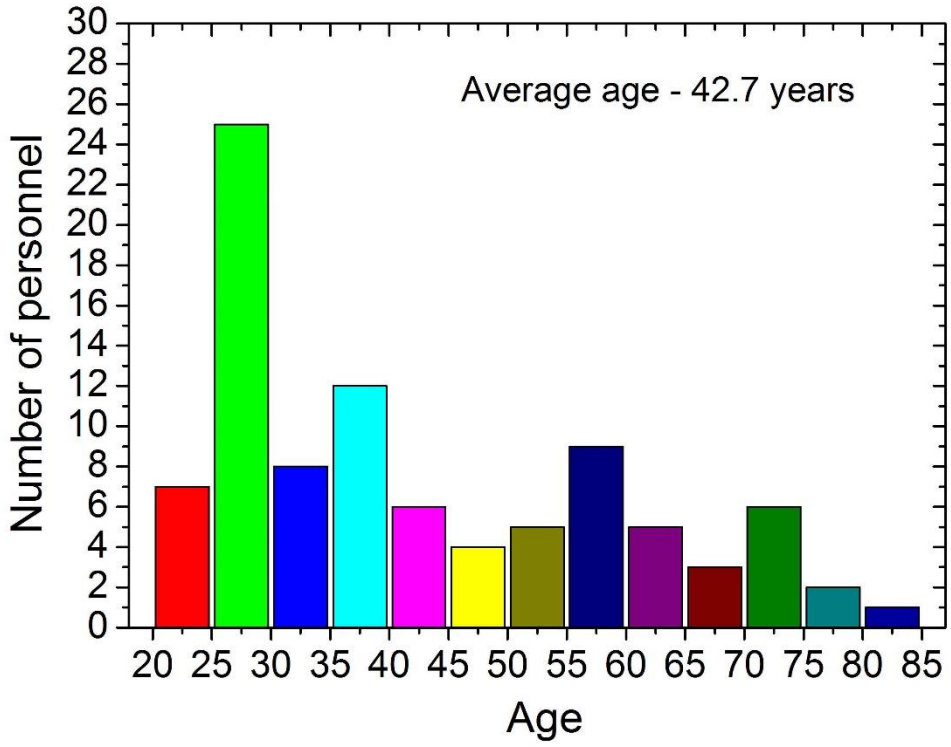

Fig. 2. Age distribution of the NICM Department employees (as of 2017).

In the reporting period, investigations of the NICM Department employees were regularly awarded with the JINR and FLNP prizes. Young employees of the Department were granted I.M.Frank's and F.L.Shapiro's scholarships, as well as JINR fellowships for young scientists and specialists; they repeatedly became prizewinners at the JINR Scientific Conferences of Young Scientists and Specialists. The list of most important prizes awarded to the NICM Department employees in the reporting period is given in Appendix 2.

A considerable number of grants and state contracts supervised or executed with the participation of the Department employees is a significant indicator of a high level of the research being conducted and the topical importance of the scientific directions being realized. A list of

grants and state contracts is given in Appendix 3. All in all, during the reported period the Department employees published 287 papers, presented 324 reports at conferences, and received 1 patent for inventions.

3. MAIN SCIENTIFIC RESULTS IN 2015 – 2017

The NICM Department employees are specialists in performing neutron scattering studies of condensed matter using neutron diffraction from poly- and single crystals, small-angle neutron scattering in substances with nano-scale inhomogeneities, inelastic incoherent nuclear and magnetic neutron scattering, reflection and scattering of polarized neutrons at interfaces.

A list of main scientific topics studied by the employees of the NICM Department includes:

- Investigation of the structure and properties of novel functional materials;
- Investigation of the structure and properties of materials under extreme conditions;
- Investigation of fundamental regularities of real-time processes in condensed matter;
- Investigation of atomic dynamics of materials for nuclear power engineering;
- Computer simulation of physical and chemical properties of novel crystalline and nanostructured materials;
- Investigation of magnetic properties of layered nanostructures;
- Investigation of structural characteristics of carbon- and silicon-containing nanomaterials;
- Investigation of molecular dynamics of nanomaterials;
- Investigation of magnetic colloidal systems in bulk and at interfaces;
- Structural analysis of polymer nanodispersed materials;
- Investigation of supramolecular structure and functional characteristics of biological materials;
- Investigation of structure and properties of lipid membranes and lipid complexes;
- Investigation of texture and physical properties of Earth’s rocks, minerals and construction materials;
- Non-destructive control of internal stresses in industrial products and construction materials;
- Introscopy of internal structure and processes in industrial products, rocks and natural heritage objects.

A characteristic feature of these studies is their interdisciplinary character involving both condensed matter physics and various allied fields of science — materials science, chemistry, biology, geology, engineering sciences.

Because of a large amount of scientific investigations carried out during the reporting period, their results are presented below as brief reviews of the main studies and supplemented by a list of related publications.

3.1. Structure investigations of novel oxide, intermetallic and nanostructured materials.

Iron oxides play an important role in the formation of magnetic and other physical properties of the Earth, and find a wide range of technological applications. Recently, a new iron oxide, Fe_4O_5, which can presumably exist in the layers of the Earth's upper mantle, has been synthesized under the combined effect of high pressures and temperatures. A comprehensive study of its physical properties, as well as atomic and magnetic structure using neutron diffraction techniques at the IBR-2 reactor, has revealed a new type of the charge-ordering state with the formation of dimeric and trimeric electronic states in this compound. The phase transition into this state is accompanied by a sharp increase in the electrical resistance and a subsequent change in the symmetry of the magnetic order, namely from a collinear antiferromagnetic (AFM) order to a

canting AFM order with a ferromagnetic (FM) component, as well as by a change in the nature of the modulation of the atomic structure, **Fig. 1** [1].

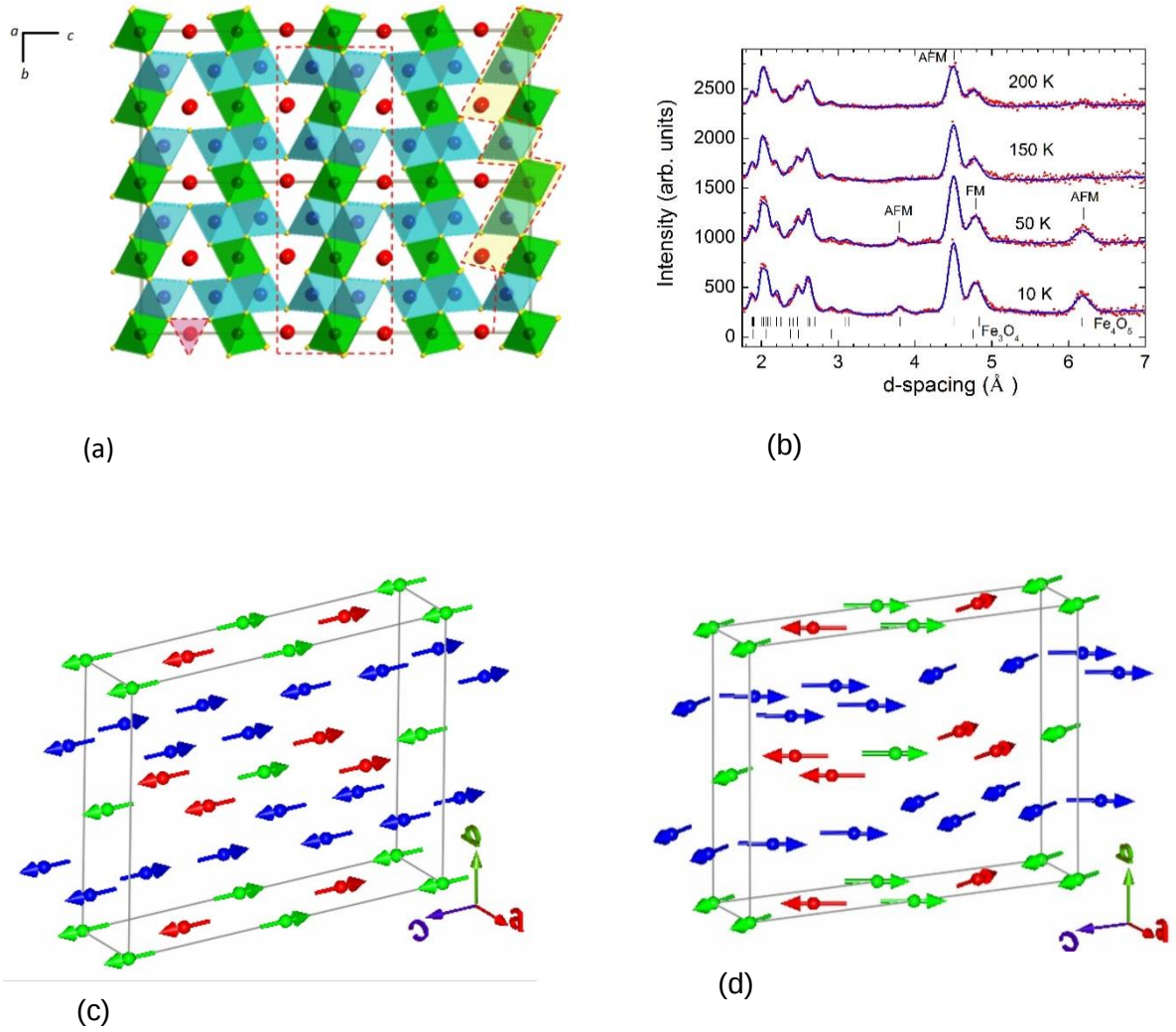

Fig. 1. Crystal structure of Fe_4O_5 (a), neutron diffraction spectra obtained at different temperatures and treated by the Rietveld method (b), the magnetic structure at T = 150 K (c) and T = 10 K (d).

The magnetic, structural, and vibrational properties of YMn_2O_5 multiferroic with a strong magnetoelectric coupling have been studied by means of neutron, x-ray diffraction, and Raman spectroscopy at pressures up to 30 GPa in a temperature range from 10 to 300 K [2] (**Fig. 2**). The application of high pressure (P > 1 GPa) resulted in a suppression of commensurate and incommensurate antiferromagnetic (AFM) phases with a propagation vector q = (~1/2, 0, ~1/4) and appearance of a new commensurate AFM phase with q_p = (1/2, 0, 1/2). This observation is in sharp contrast to a general trend towards the stabilization of the commensurate AFM phase with the propagation vector q = (1/2, 0, 1/4) found in other RMn_2O_5 compounds under pressure. At higher pressures P > 16 GPa a structural phase transition accompanied by anomalies in the pressure behavior of some unit cell parameters and vibrational modes was observed. The obtained data allowed us to analyze the role of competing magnetic interactions in the formation of the magnetic ground state of RMn_2O_5 multiferroics.

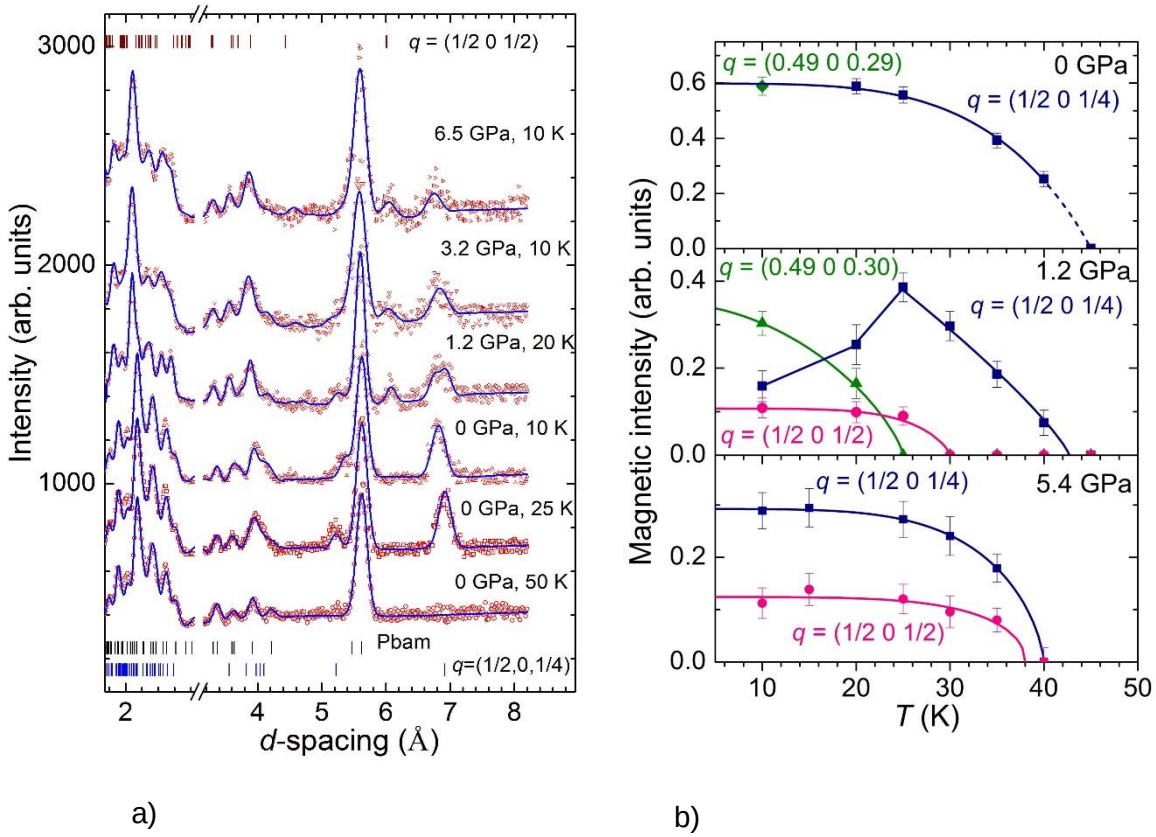

a) b)

Fig. 2. Neutron diffraction spectra of YMn_2O_5 obtained at different pressures and temperatures on the DN-12 diffractometer and treated with the Rietveld method (a). Temperature dependences of integrated intensity of peaks $(1-q_x, -1, -q_z)/(1-q_x, 1, -q_z)/(\pm q_x, 1, \pm q_z)$ of commensurate and incommensurate AFM phases with a propagation vector q = (~1/2, 0, ~1/4) and a peak $(-q_x, 1, 1-q_z)$ of commensurate AFM phase with a propagation vector q_p = (1/2 0 1/2) under various pressures (b).

The search for new multiferroics and magnetoelectrics is of current interest in modern condensed matter physics and materials science. A promising system is $BaMn_{1-x}Ti_xO_3$ whose end members are a classical ferroelectric $BaTiO_3$ with a high Curie temperature (T_C = 395 K) and $BaMnO_3$ – a compound exhibiting a giant magnetoelectric effect and having a relatively high temperature of magnetic ordering (T_N = 230 K). The studies of $BaMn_{1-x}Ti_xO_3$ over the entire concentration range $0 < x < 1$ have revealed a very rich structural polymorphism. An increase in the titanium concentration was followed by a sequence of phase transitions between different rhombohedral and hexagonal phases differing by the ratio of oxygen octahedra connected through the corners and edges, 15R - 8H - 9R - 10H - 12R, **Fig. 3**. [3]. It has been found that the formation of a long-range magnetic order is possible only in structures: 9R, 8H, 15R and at concentrations of Ti $x < 0.25$, and the Neel temperature has a very sharp concentration dependence and drops from 230 to 100 K in the given x-range.

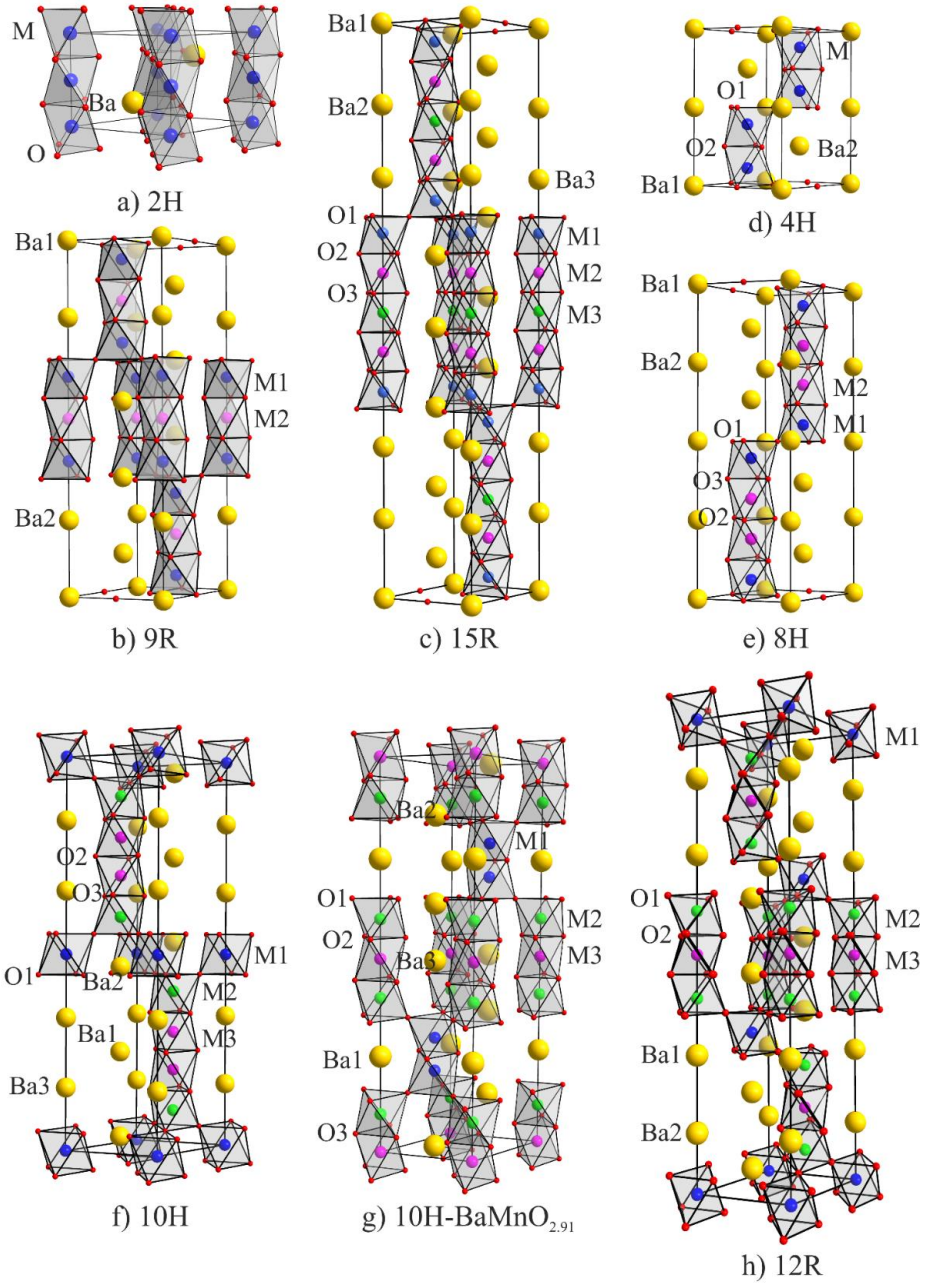

Fig. 3. Structure of polymorphic phases in the system $BaMn_{1-x}Ti_xO_3$.

The structural characteristics of promising high-voltage cathode materials on the basis of $LiNi_{0.5}Mn_{1.5}O_4$ - $LiNi_{0.5-x}Mn_{1.5-y}M_{x+y}O_4$ (M=Co, Cr, Ti, Al, Mg; x+y=0.05) synthesized in the Institute of Solid State Chemistry and Mechanochemistry, SB RAS (Novosibirsk) have been studied in order to improve their electrochemical properties [4]. Unsubstituted $LiNi_{0.5}Mn_{1.5}O_4$ is characterized by a high potential (4.7 V) corresponding to a flat plateau in a charge-discharge characteristic at an average capacity of 120 mAh/g, which significantly increases the specific stored energy of the battery compared to other materials ($LiCoO_2$ ~3.8 V, $LiFePO_4$ ~3.2 V at the same capacity). Depending on the method of synthesis $LiNi_{0.5}Mn_{1.5}O_4$ may have either a primitive cubic $P4_332$ symmetry with an ordered arrangement of cations (in this case the synthesis temperature should not exceed 700°C) or a face-centered cubic Fd-3m symmetry and disordered arrangement of cations (formed at temperatures above 800°C). Due to the structural transformations during cycling the $LiNi_{0.5}Mn_{1.5}O_4$ compound with a $P4_332$ space group shows poorer electrochemical behavior than $LiNi_{0.5}Mn_{1.5}O_4$ with a Fd-3m structure. Samples for the study were synthesized at T < 800°C by means of a small substitution of other transition metals

for Ni and Mn cations and mechanical activation of the reagent mixture in a planetary mill. As a result of the treatment of the neutron diffraction spectra using the Rietveld method it has been revealed that all the samples under study have a two-phase structure, with a phase having an Fd-3m space group being a dominant one and a secondary phase with a $P4_332$ space group ranging from 1 to 20% depending on the substitution metal and the synthesis temperature. It has been found that the dopants preferably substitute for Ni ions, which in turn results in the appearance of a NiO impurity phase in a small amount (1-2%). The average crystal size was 70-80 nm for the samples synthesized at 700°C, and 100-150 nm for the samples synthesized at 800°C. As expected, large microstrains were found to be more frequent in the samples with lower synthesis temperature.

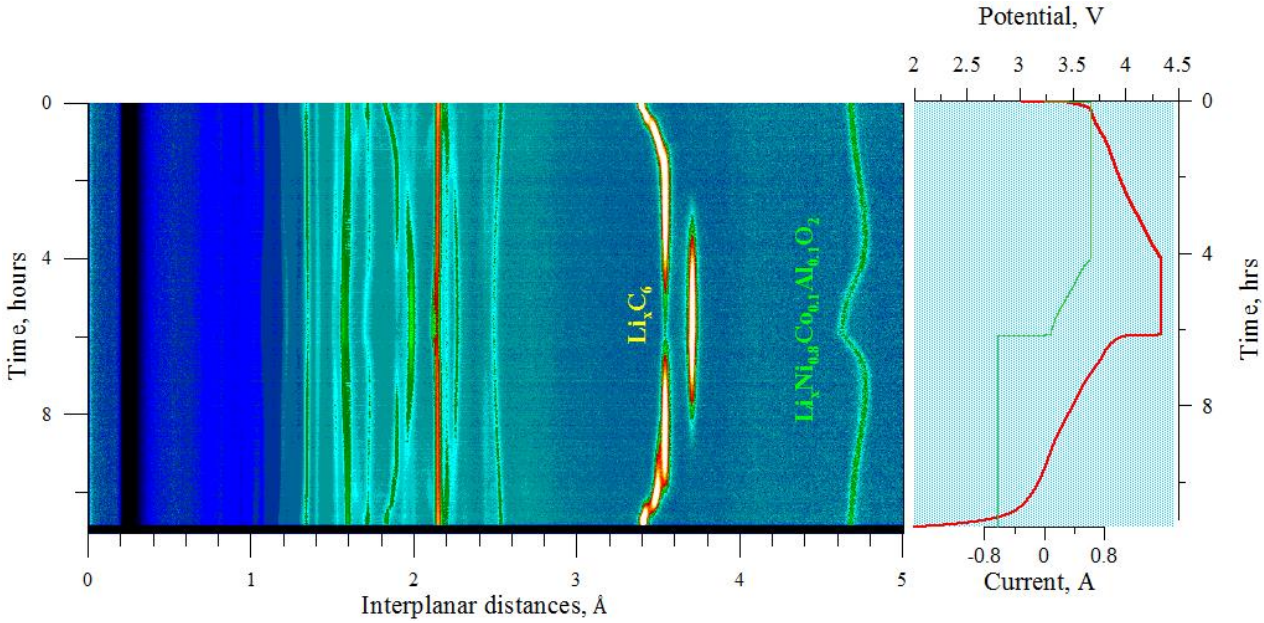

Fig. 4. The evolution of neutron diffraction spectra obtained in the real-time (*operando*) study of $LiNi_{0.8}Co_{0.1}Al_{0.1}O_2$ cathode material using high-intensity neutron diffraction. At the right: charge-discharge curve of the power source during the experiment.

A study of the evolution of the crystalline structure of the cathode material $LiNi_{0.8}Co_{0.1}Al_{0.1}O_2$ in the process of electrochemical cycling has been carried out using neutron diffraction (**Fig. 4**). The experiments were performed on the RTD (Real-Time-Diffractometer) diffractometer. Compositions of $LiNi_xCo_yAl_{1-x-y}O_2$ type are just starting to be introduced in mass production of lithium-ion batteries as a positive electrode (cathode) gradually replacing the widespread lithium cobaltate. Earlier such compounds were studied in real time during electrochemical cycling only in model cells by x-ray diffraction. Neutron diffraction makes it possible to study structural changes in the electrode materials both in specialized electrochemical cells and immediately in finished products. This study investigated a Li-Ion 18650 cylindrical rechargeable battery, where graphite is used as a negative electrode and $LiNi_xCo_yAl_{1-x-y}O_2$ with $x \approx 0.8$ and $y \approx 0.1$ (these values were specified in the treatment of the obtained diffraction data) as a positive electrode. The crystal structure of $LiNi_xCo_yAl_{1-x-y}O_2$ in a completely discharged battery corresponds to a space group *R*-3*m* with unit cell parameters $a = 2.8453(1)$ and $c = 14.1878(2)$ Å. On the basis of the analysis of experimental data obtained in the course of several charge-discharge cycles performed at different rates (C/3 and C/10, where C is the full capacity) it has been shown that the intercalation of lithium into graphite proceeds with the successive formation of several LiC_n phases. The formation of final LiC_6 phase during charging is easily detected by a step-like appearance of a diffraction peak at $d \approx 3.67$ Å. The phase separation in the cathode material $LiNi_{0.8}Co_{0.1}Al_{0.1}O_2$, which can be observed, for example, in $LiNi_{0.8}Co_{0.15}Al_{0.05}O_2$, has not been found. At the same time, the unit cell parameters of the two materials change during charging in a

similar manner, and the expansion and subsequent contraction of the unit cell proceed anisotropically. When charging, at first the cell expands along the hexagonal *c* axis and slightly contracts in the basal plane (*a* and *b* axes). Towards the end of charging, there occur an abrupt contraction along the *c* axis and some expansion along the *a* and *b* axes.

Using high-resolution neutron diffraction the structural (from the cubic phase to the rhombohedral phase) and magnetic (from the paramagnetic phase to the antiferromagnetic phase) phase transitions in NiO and MnO have been studied, **Fig. 5**, [5]. Despite the already long history of the study of phase transitions in simple antiferromagnets of NiO type by various experimental methods, the literature data about them are quite contradictory. It has been shown that in MnO the structural and magnetic transitions occur simultaneously, their temperatures are the same within the experimental error: $T_{str} \approx T_{mag} \approx (119 \pm 1)$ K. For NiO the measurements were performed on powders with different mean crystallite sizes (~ 1500 nm and ~ 138 nm), and in both cases it has been found that the transition temperatures differ by ~ 50 K: $T_{str} = (471 \pm 3)$ K, $T_{mag} = (523 \pm 2)$ K.

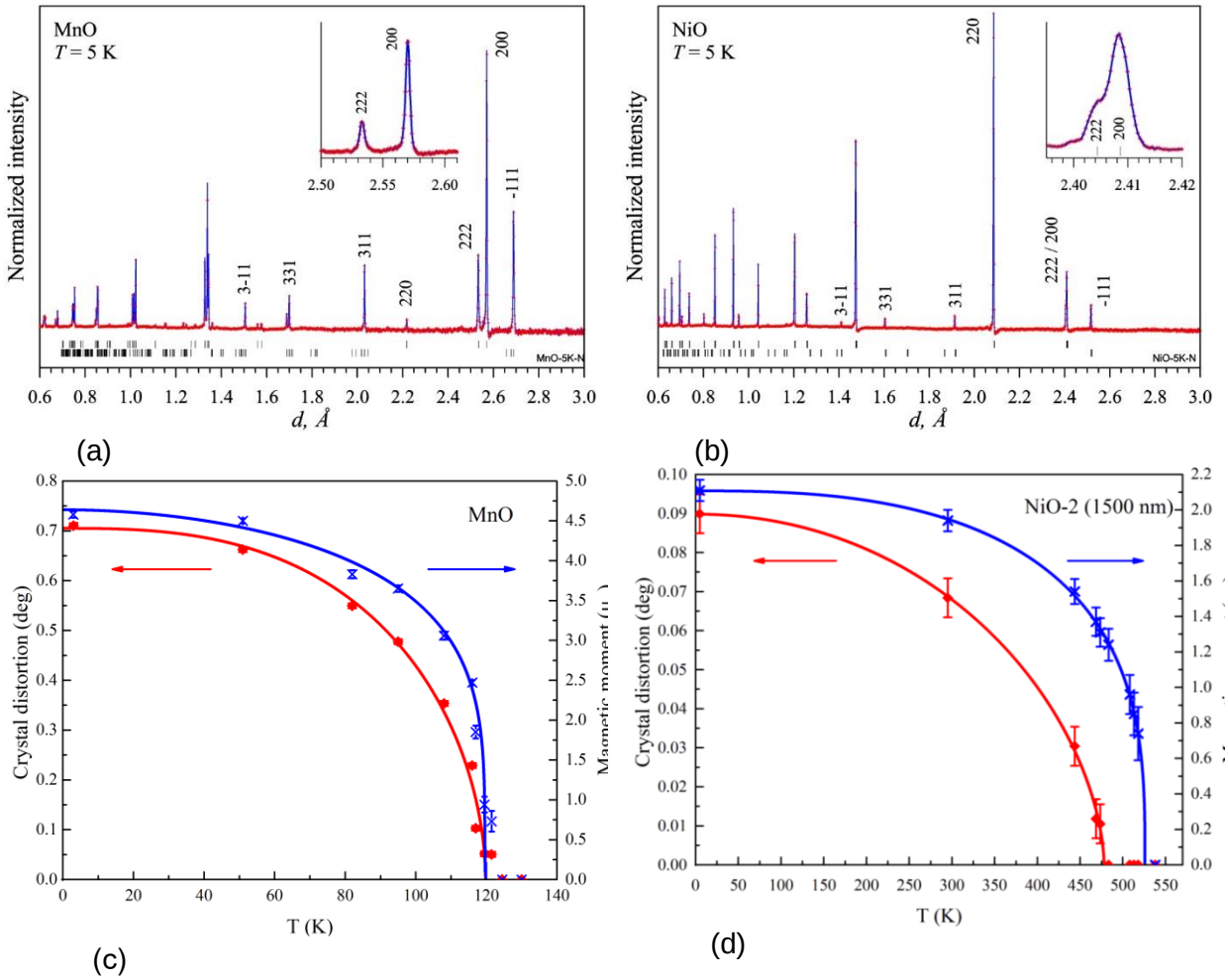

Fig. 5. Neutron diffraction spectra of high resolution at T = 5 K for MnO (a) and NiO (b) obtained at HRFD. Dashes indicate the positions of crystal (top row) and magnetic (bottom row) diffraction peaks. Miller indices (for a large R-lattice) are shown for several magnetic and first crystalline diffraction peaks. The inset shows the splitting of the peaks (200) and (222) due to the rhombohedral distortion. The dependence of the angle of rhombohedral distortion (left scale, red points) and magnetic moment (right scale, blue points) on temperature for MnO (c) and NiO-2 sample with the mean crystallite size of 138 nm (d).

$La_{1-x}Sr_xFe_{2/3}Mo_{1/3}O_3$ ($0 \le x \le 1$) perovskites allow exceptionally wide variation of the Mo charge state from +3 (x = 0) to +6 (x = 1) while the charge state of Fe^{3+} remains virtually unchanged. The end members of this series show antiferromagnetic ordering in $LaFe_{2/3}Mo_{1/3}O_3$ at

T_N = 520 K and ferrimagnetic ordering in $SrFe_{2/3}Mo_{1/3}O_3$ at T_C = 420 K. In both cases, the magnetic structure is dictated by antiferromagnetic superexchange between localized magnetic moments. At intermediate compositions, an interplay of antiferromagnetic-superexchange and double-exchange interactions results in nonmonotonous variations of both the magnetic-ordering temperature and saturation magnetization. To determine the magnetic phase diagram (**Fig. 6**) and the cation charge states, neutron diffraction spectra were measured, and XANES data and data on magnetic susceptibility and magnetization were obtained. Also, the magnetic moment per formula unit was determined (**Fig. 6**). On the basis of all experimental data, a detailed analysis of the emerging interactions was carried out [6].

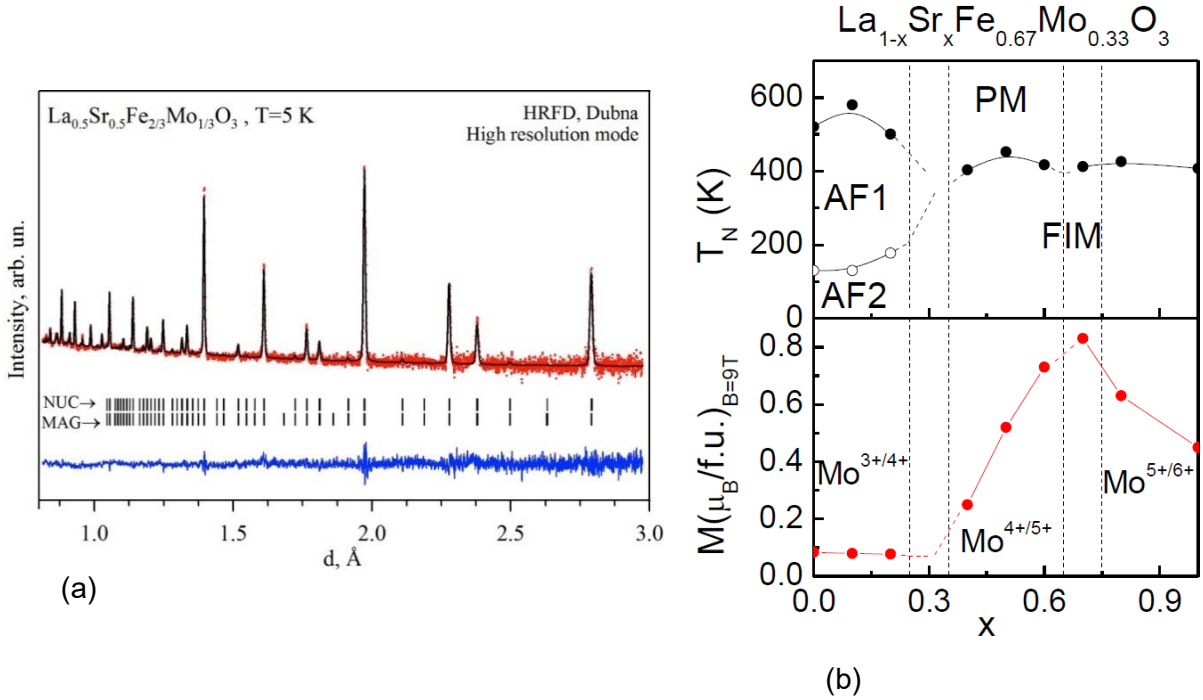

Fig. 6. Neutron diffraction spectrum from $La_{0.5}Sr_{0.5}Fe_{2/3}Mo_{1/3}O_3$ treated by the Rietveld method (a). Experimental points, calculated function and difference curve are shown. Dashes show the calculated positions of the nuclear (top row) and magnetic (bottom row) diffraction peaks. The magnetic phase diagram (top) and the magnetic moment value measured at 2 K in a field of 9 T for the $La_{1-x}Sr_xFe_{2/3}Mo_{1/3}O_3$ series (b). Vertical lines separate the regions with different charge states of molybdenum.

Methods for obtaining different compounds in the nanostructured state have been developing in recent years. The $VC_{0.875}$ compound was the first carbide in whose coarse-grained powder a nanostructure was created as a result of the disorder-order transformation ($VC_{0.875} \rightarrow V_8C_7$). The atomic-vacancy ordering makes it possible to create the nanostructure in the $VC_{0.875}$ bulk carbide. However, until recently it was unclear whether the superstructure V_8C_7 remains after milling the ordered vanadium carbide to a nanopowder with the average particle size of 400-500 Å and less. The crystal structure and microstructure of coarse- and nanocrystalline disperse ordered carbide V_8C_7, which was prepared by milling the initial coarse-crystalline powder for 10 h in a planetary ball mill, were studied on the HRFD diffractometer [7], **Fig. 7**. According to the scanning electron microscopy data, the initial powder ~V_8C_7 consists of large particles with the size of 3–5 μm, the microstructure of which is a set of curved lobes with diameters from 400 to 600 nm and thicknesses of about 15–20 nm. The nanopowder V_8C_7 obtained by milling for 10 h consists of nanoparticles with sizes of 20–60 nm united in friable agglomerates with the size from ~400 nm to ~1 μm. All obtained spectra of the coarse-grained powder ~V_8C_7 include weak superstructure reflections of the ordered phase V_8C_7. For the coarse-grained vanadium carbide

~$VC_{0.875}$ (V_8C_7), the dependence of the width of diffraction peaks on the interplanar distances, $\Delta d^2(d^2)$, is linear, indicating that there is no size effect. For the nanopowder the diffraction peaks are strongly broadened and the dependence $\Delta d^2(d^2)$ is parabolic, from which it follows that the average size of particles of the nanopowder is about 190 Å. Also, the presence of the disordered phase $VC_{0.875}$ with the structure B1, the lattice period of which is $a_{B1} < a_{V_8C_7}/2$, was found in the samples under study. The analysis revealed that the disordered phase represents small-size inclusions (~500 Å) in the matrix of the ordered phase V_8C_7, and its content in the coarse-crystalline powder is (21 ± 3) wt %. The real structure of the ordered phase is characterized by a lowered content of carbon as compared to the ideal one, which corresponds to the chemical composition $V_8C_{7-\delta}$, where $\delta \cong 0.03$.

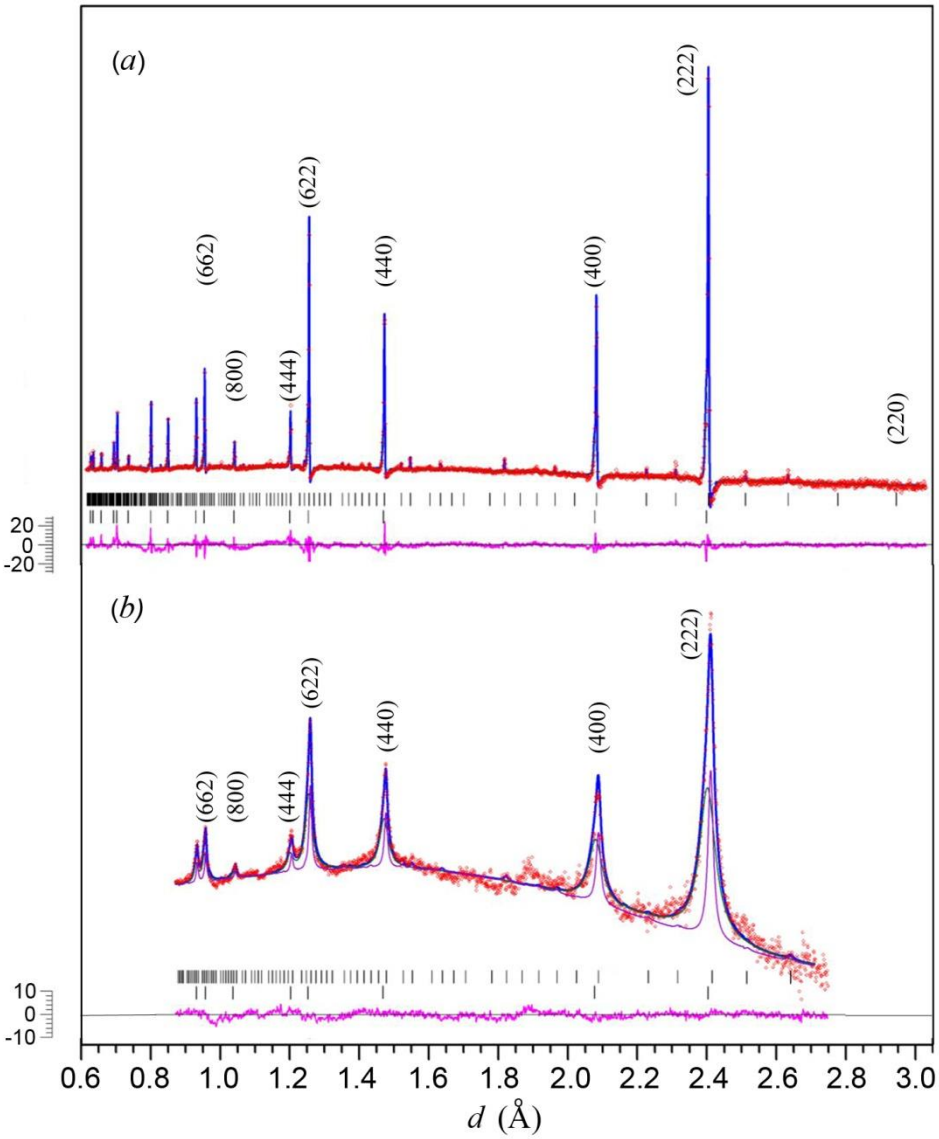

Fig. 7. Refinement of the neutron diffraction patterns of vanadium carbide powders (measurements in the high-resolution mode by detectors placed at the scattering angle $2\theta = 152°$): (a) initial coarse-grained powder and (b) nanopowder. The disordered phase is present in the samples along with the main ordered phase. Contributions of the ordered (narrow peaks) and disordered (wide peaks) are shown for the nanopowder. Vertical marks in the upper and lower rows indicate the positions of reflections of the ordered phase $V_8C_{7-\delta}$ ($\delta \cong 0.03$) and the disordered phase $VC_{0.875}$, respectively.

The vanadium carbide nanopowder also contains the ordered and disordered phases (**Fig. 7**), but as a result of milling, the amount of the latter is (45 ± 10) wt %. The periods of cubic unit cells of phases V_8C_7 and $VC_{0.875}$ in the nanopowder are slightly smaller than in the coarse-crystalline powder. Taking into account the limitations on the accuracy of determination of the filling of positions of C atoms it is believed that the nanocrystalline ordered phase has the same composition $V_8C_{7-\delta}$, $\delta \cong 0.0$ as that the coarse-grained powder. The displacements of carbon atoms C3 and C4 in the lattice of the nanocrystalline ordered phase $V_8C_{7-\delta}$ are small. At the same time, the displacements of the same atoms are larger in the coarse-grained ordered phase. This is due to the noticeable deformation distortions of the lattice during milling of the powder.

Neutron diffraction studies of the $Fe_{0.735}Al_{0.265}$ compound were carried out in a wide temperature range (20-900°C) to determine its structural states and atomic ordering mechanism [8], **Fig. 8**. The combination of high-resolution diffraction and real-time diffraction made it possible to establish that, in contrast to traditional approaches, the structure of this compound at room temperature is a phase with only partially ordered arrangement (B2) of Fe and Al in a unit cell. A completely ordered phase (Fe_3Al - $D0_3$ type) is present as clusters of mesoscopic size (~ 200 Å) coherently incorporated into the matrix of the main phase. After the transition to a disordered state ($T > 740$°C) and slow cooling to room temperature, the dimensions of the structurally ordered clusters increased to ~ 900 Å.

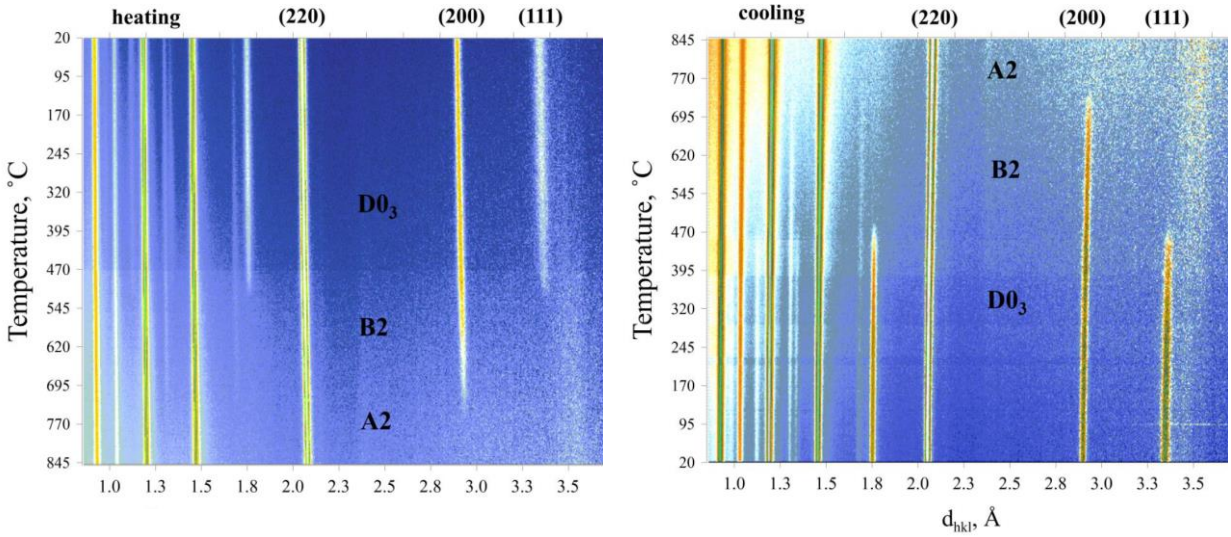

(a) (b)

Fig. 8. 2D representation of structural transitions in Fe-27Al under heating (a) and cooling (b). The initial (before heating) and final (after cooling) conditions – $D0_3$ phase characterized by the presence of peaks (111) and (200). In the B2 phase the peak (111) is absent, while the peak (200) remains. In the A2 phase both of these peaks are absent. The rates of heating and cooling were ±2 °C/min, the measurement time of one spectrum – 1 min, i.e. each picture contains about 400 spectra.

A high contrast between the coherent neutron scattering lengths of iron and aluminum made it possible to determine with a good accuracy the temperature dependence of the occupancy factors of sites by Fe and Al atoms up to a phase transition to the disordered state. The obtained results call for further analysis of the equilibrium phase diagram for the Fe-Al system.

The crystal and magnetic structure of nanostructured manganites $La_{1-x}Sr_xMnO_3$ (x = 0.28, 0.37) has been studied in the pressure range of 0 - 4.5 GPa and temperature range of 5 - 300 K [9]. The physical properties of these compounds in the nanostructured state differ significantly from those in the bulk holding much promise for applications in biomedical technologies. In both

compounds the ferromagnetic ordering is formed at temperatures close to room temperature, and at low temperatures (T < 270 K) the appearance of an additional A-type AFM phase is observed (**Fig. 9**). At higher pressures the volume fraction of AFM phase increases and that of FM phase decreases. The obtained results were interpreted in the framework of the "core-shell" model of the formation of nanoparticles in which the core is ferromagnetic and the shell is antiferromagnetic. The observed behavior of the volume of magnetic phases points to an increase in the thickness of the shell of nanoparticles under pressure.

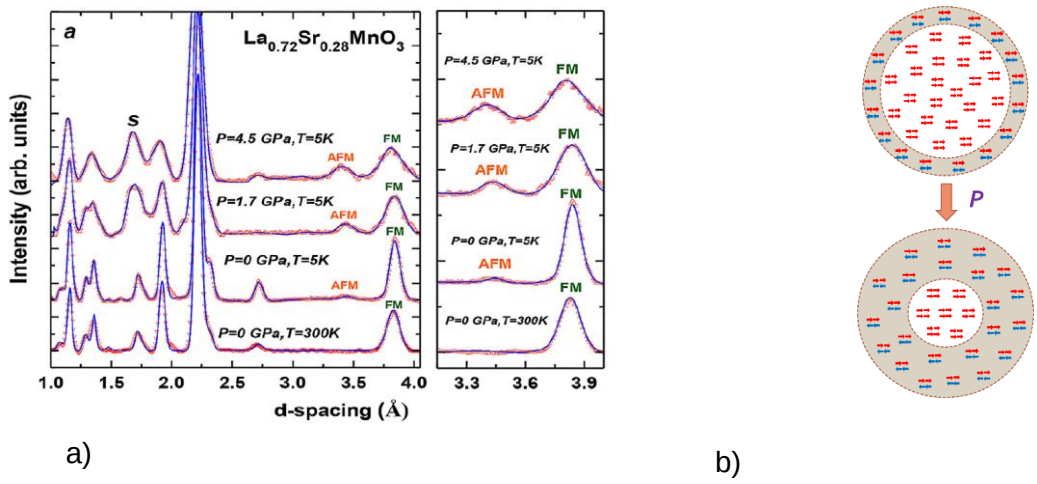

Fig. 9. Neutron diffraction spectra of nanostructured manganite $La_{0.72}Sr_{0.28}MnO_3$ obtained at different pressures and temperatures on the DN-12 diffractometer and treated using the Rietveld method (a). "Core-shell" model of nanoparticles and their structural evolution under pressure (b).

3.2. Investigations of magnetic fluids and nanoparticles

In the framework of the study of the adsorption of magnetic nanoparticles on solid surfaces the experiments on neutron reflectometry with a horizontal sample plane were continued for the interface of magnetic fluids with crystalline silicon using different treatment of the surface of the solid support. Thus, when contacting a solid hydrophilic surface, aqueous magnetic fluids characterized by the presence of a number of stable aggregates in solution form a single adsorption layer of non-aggregated nanoparticles at the interface [10]. Moreover, in the experiments with different configurations ('crystal on top' or 'crystal at bottom') a substantial difference in the critical angle of total reflection is observed pointing in the second case to an increase in the concentration of nanoparticles of the magnetic fluid at the interface due to the gravitational effect (**Fig. 10**). One can conclude that in contrast to magnetic fluids on weakly polar solvents, where the adsorption mechanism is mainly determined by gravitational sedimentation, in the aqueous magnetic fluids adsorption occurs mainly due to the electrostatic interaction between the nanoparticles with the substrate surface.

The study has been carried out in collaboration with the Institute of Experimental Physics, Slovak Academy of Sciences (Kosice, Slovakia), Faculty of Physics of the Taras Shevchenko National University of Kiev (Kiev, Ukraine), research Institutes of the Romanian Academy of Sciences (Bucharest-Timisoara, Romania) and the Max Planck Institute for Solid State Physics (Stuttgart, Germany).

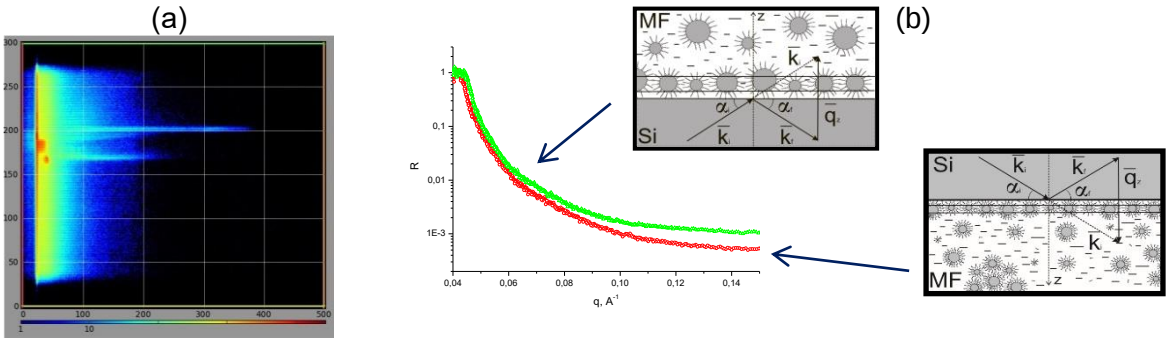

Fig. 10. (a) 2D spectrum (GRAINS, IBR-2) of the reflected beam of unpolarized neutrons at the interface of the aqueous magnetic fluid (magnetite/sodium oleate/D_2O) with silicon in the coordinates "height of the detector Z - time of flight"; (b) Reflectivity as a function of the momentum transfer for the system magnetic fluid/silicon crystal measured in configurations 'crystal on top' and 'crystal at bottom' with corresponding representations of the structural organization of nanoparticles of the magnetic fluid at the interface with silicon.

Experiments on small-angle neutron scattering (SANS) and neutron reflectometry with a horizontal sample plane for the interface of magnetic fluids with silicon (GRAINS) have been carried out in the framework of investigations of the structure and stability of magnetic nanoparticles in bulk and at interfaces, **Fig. 11** [11]. It has been found that in the bulk of aqueous ferrofluids stabilized by sodium oleate there are comparatively small (size ~ 30 nm) and compact aggregates of magnetic particles. When magnetic fluids are modified by biocompatible polymer polyethylene glycol (PEG), cluster reorganization in the bulk of magnetic fluids is observed, namely large and branched clusters (size > 130 nm, fractal dimension of 2.7) appear. The observed in-bulk reorganization of the magnetic fluids is correlated with the neutron reflectometry data, which is indicative of the formation of a single adsorption layer of magnetic particles on the surface of oxidized silicon in the initial magnetic fluid and the absence of any layer at the ferrofluid/silicon interface after the polymer modification. The study has been performed in collaboration with the Institute of Experimental Physics, Slovak Academy of Sciences (Kosice, Slovakia); the Faculty of Physics of the Taras Shevchenko Kyiv National University (Kiev, Ukraine); the National Institute of Physics and Nuclear Engineering (Bucharest, Romania); Timisoara Branch of the Romanian Academy of Sciences (Timisoara, Romania) and the Max-Planck Institute for Solid State Physics (Stuttgart, Germany).

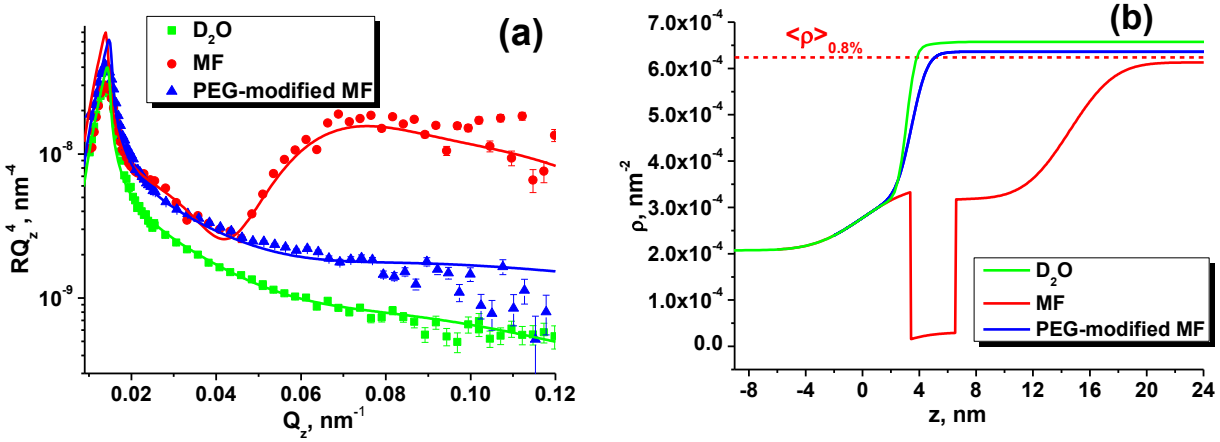

Fig. 11. (*a*) Experimental reflectivity curves for heavy water and magnetic fluids; (*b*) resulting scattering length density profiles.

With the help of small-angle neutron scattering changes in the structural organization of transformer-oil-based magnetic fluids have been observed under the action of an external DC and AC electric field (**Fig. 12**) [12]. The investigations have been carried out to clarify the effect of the voltage breakdown enhancement in liquid transformers when adding nanoparticles, in particular magnetite nanoparticles stabilized by oleic acid, to a liquid carrier. It has been shown that after the application of a DC electric field along with a macroscopic phase separation the aggregation at the size level of 100 nm takes place strongly dependening on the field strength. After the electric field is switched off, after a time (of the order of a few hours) the system returns to its original structural state. In the case of an AC electric field, the aggregates also appear at sufficiently low frequencies, and the process terminates when the frequency exceeds a certain critical value.

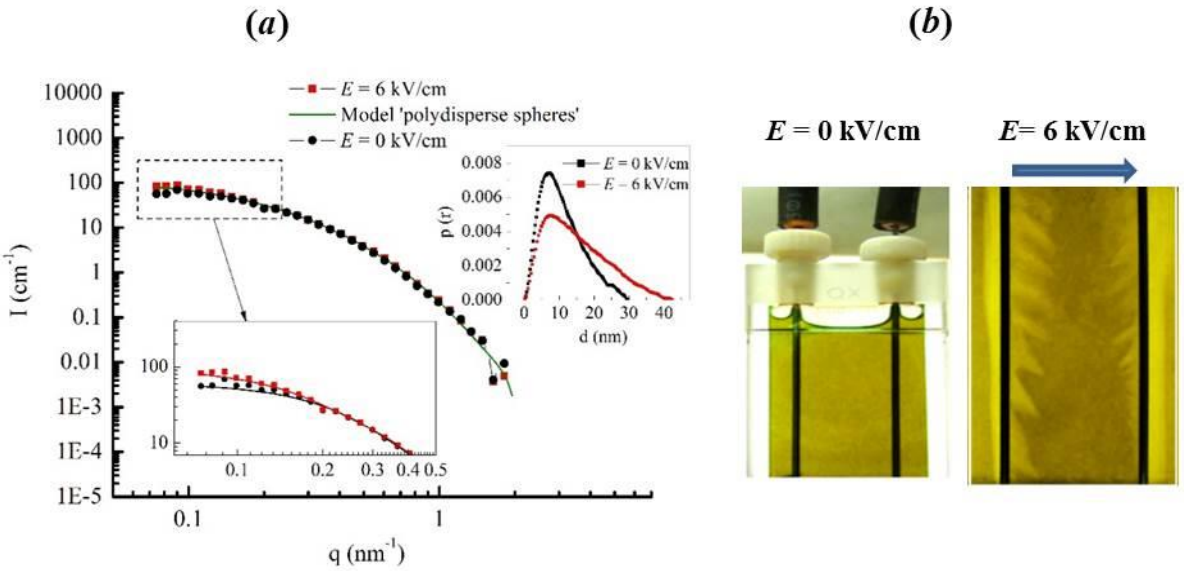

Fig. 12. The effect of an external electric field on the structure of the magnetic fluid magnetite/oleic acid/transformer oil for (a) nanoscale: small-angle neutron scattering (YuMO, IBR-2), magnetite concentration of 1%, and (b) macrolevel: visual observation of phase separation in a quartz cell (1 mm thick), magnetite concentration of 0.05%. The inset in (a) shows the correlation functions reconstructed from the scattering curves (in the form of pair distance distribution functions) for a fluid in two states with "no field" and "in a field", which point to an increase in the characteristic size as a result of aggregate formation under the applied field, as well as the presence of anisotropy in the aggregate shape.

Thus, in addition to the effects of aggregation in an external magnetic field, which is typical for magnetic fluids, a similar sensitivity to the electric field for magnetic fluids based on dielectric carriers has been detected, which opens up new potential possibilities for regulating the properties of these complex systems using external control parameters. The study has been carried out in collaboration with the Institute of Experimental Physics, Slovak Academy of Sciences (Kosice, Slovakia), Faculty of Physics of the Taras Shevchenko National University of Kiev (Kiev, Ukraine), and the Research Centre of Jülich - Department of Neutron Research (Munich, Germany).

In order to improve the synthesis procedure for biocompatible magnetic fluids, SANS (YuMO) and SAXS experiments have been carried out for magnetic fluids prepared using three different methods (**Fig. 13**). An important feature of the ferrofluids under study was the addition of a specific component (polysaccharide agarose) to the water-based carrier, which complemented the stabilization effect and also provided biocompatibility of the initial fluids. It has been demonstrated that all investigated magnetic fluids have a complicated and highly aggregated

structure, but nevertheless are stable in time. The structures of the magnetic fluids obtained by two methods of synthesis are similar to each other and different from that synthesized using the third method. In the last case two power-law type scattering levels corresponding to mass and surface fractals were observed along with an increase in the characteristic size of magnetic particles. The study [13] has been performed in collaboration with the V.I.Vernadsky Institute of General and Inorganic Chemistry (Kiev, Ukraine) and the Department of Physics of the Taras Shevchenko Kyiv National University (Kiev, Ukraine).

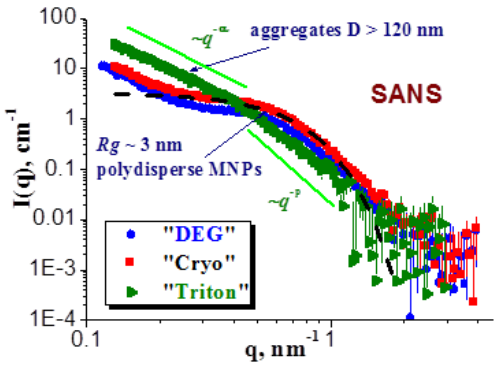

Fig. 13. SANS curves for magnetic fluids with agarose synthesized by three different methods. The concentration of magnetite is ~8.8. %; agarose – 0.1 vol. %.

As a part of a comprehensive study of the interaction of magnetic nanoparticles with amyloid protein formations, the experiments on small-angle scattering of synchrotron radiation, transmission electron microscopy, atomic force microscopy and magneto-optical methods have been carried out for the mixtures of fibril amyloid aggregates of protein lysozyme (egg white) with magnetite nanoparticles in the concentration range of 0.01-0.1 vol. % [14, 15]. The analysis of the complementary data has revealed that the magnetic nanoparticles are adsorbed onto the surface of amyloids, and the adsorption mode depends on the concentration ratio between the magnetic particles and the protein in solution. Thus, with increasing concentration of magnetic nanoparticles in solution there appear particle aggregates repeating a cylindrical shape of the amyloids. The observed effect has been considered in connection with the formation of an amyloid liquid crystal phase under an external magnetic field which can be used in practice. The study has been performed in collaboration with the Institute of Experimental Physics, Slovak Academy of Sciences (Kosice, Slovakia), Department of Physics, Taras Shevchenko National University of Kyiv (Kiev, Ukraine) and Helmholtz Centre Geesthacht (Geesthacht, Germany).

In the framework of the investigation of factors affecting the stability of magnetic fluids, studies of the effect of the surfactant excess on the stability of ferrofluids have been continued [16]. In particular, using SANS the structure of magnetic fluids based on non-polar solvent decalin and stabilized by saturated monocarboxylic acids of different alkyl chain lengths (C16, palmitic acid; C12, lauric acid), with an excess of acid molecules has been studied. It has been shown that the addition of the acid to the initial stable system with an optimum composition results in structural changes associated with the more significant aggregation than that previously observed for this class of magnetic fluids. By comparing the impact of mono-carboxylic acids on the stability of non-polar ferrofluids, one can conclude that the aggregation growth is substantially more evident in excess of palmitic acid. This confirms the findings of the previous studies that an increase in the length of saturated acids reduces their stabilization efficiency in respect to magnetic fluids. The study has been carried out in collaboration with the Department of Physics, Taras Shevchenko National University of Kyiv (Kiev, Ukraine) and the Wigner Research Centre of the Hungarian Academy of Sciences (Budapest, Hungary).

Molecular dynamic (MD) simulations of the low-polarity organic solutions of saturated mono-carboxylic acids with alkyl chain lengths C14 (myristic acid) and C18 (stearic acid) used in the stabilization of magnetic fluids have been applied for the interpretation of the experimental curves of small-angle neutron scattering (SANS) from these systems [17]. In particular, the comparison of the acid structural parameters obtained in the analysis of the SANS curves from the solutions in deuterated benzene and decaline has revealed that in the second solvent there is a significant (up to 15%) increase in the limiting partial volume of the acid molecules despite their close effective conformational lengths. Thus, it has been found that the considered C14 and C18 acids due to the rapid attenuation of the dispersive interaction with distance are characterized by a lower affinity (lyophilic properties) to decalin which exhibits a more complex structure as compared to benzene. Also, the formation of a liquid crystalline phase in concentrated solutions (concentration ranges of 7 – 25 vol.% for C14 and 3 - 10 vol.% for C18) based on deuterated solvents has been considered. The lower values observed in the experiments for the formation of the liquid crystal phase in the solutions based on decalin as compared to benzene can be explained by the structural features of the solvate shells around the acids obtained from the MD simulations. The study has been carried out in collaboration with the Wigner Research Centre for Physics of the Hungarian Academy of Sciences (Budapest, Hungary) and Faculty of Physics of the Taras Shevchenko National University of Kiev (Kiev, Ukraine).

3.3. Investigations of carbon nanomaterials

Small-angle neutron scattering has been applied to characterize the structure of commercial aqueous dispersions of detonation nanodiamonds (DND) [18]. It has been found (**Fig. 14**) that the fractal organization of clusters in the solutions repeats the results of the previous similar experiments on the DNA dispersions of different types, which is indicative of a unique mechanism of the cluster formation during the dispersion synthesis. To explain this mechanism, a modified model of diffusion-limited aggregation (DLA-model) extended for the first time to the case of clusters of polydisperse structural units (DNA particles) has been proposed. It has been shown that along with a polydispersity of the DNA particles a sufficiently high polydispersity of the clusters is required to fit the scattering curves by this model. The "light" and "heavy" cluster fractions separated by centrifugation reveal the same kind of clusters at different size scales. The effect of the scattering structure-factor characterizing the cluster-cluster interaction in concentrated suspensions of "light" and "heavy" cluster fractions has been described. The study has been carried out in collaboration with the Department of Chemistry of the Moscow State University (Moscow, Russia) and the Faculty of Physics of the Taras Shevchenko National University of Kiev (Kiev, Ukraine).

In addition, the investigations related to the structural characterization of aqueous dispersions of detonation nanodiamonds (DND) have been continued [19]. In particular, the structures of DND hydrogels with a positive ζ-potential have been studied. The results of the SANS contrast variation have been compared with the data of the previous similar experiments for DND suspensions with a negative ζ-potential. No principal differences from a structural viewpoint between ζ+ and ζ- stabilizations of aqueous DND suspensions have been found. The identity of the structure on the size scale up to 100 nm has been proved with respect to the developed clusters characterized by similar values of fractal dimensions, as well as to the DND particles characterized by polydispersity (above 30%) and diffuse surface. This demonstrates the existence of a common mechanism for DND cluster formation and growth in suspensions, regardless of the method of stabilization. It has been assumed that nanosystems are stabilized by the formation of a charged interface around the whole clusters rather than around individual particles in them. The study has been carried out in collaboration with the Ioffe Physical-Technical Institute RAS (Saint-Petersburg, Russia) and the Department of Physics, Taras Shevchenko National University of Kyiv (Kiev, Ukraine).

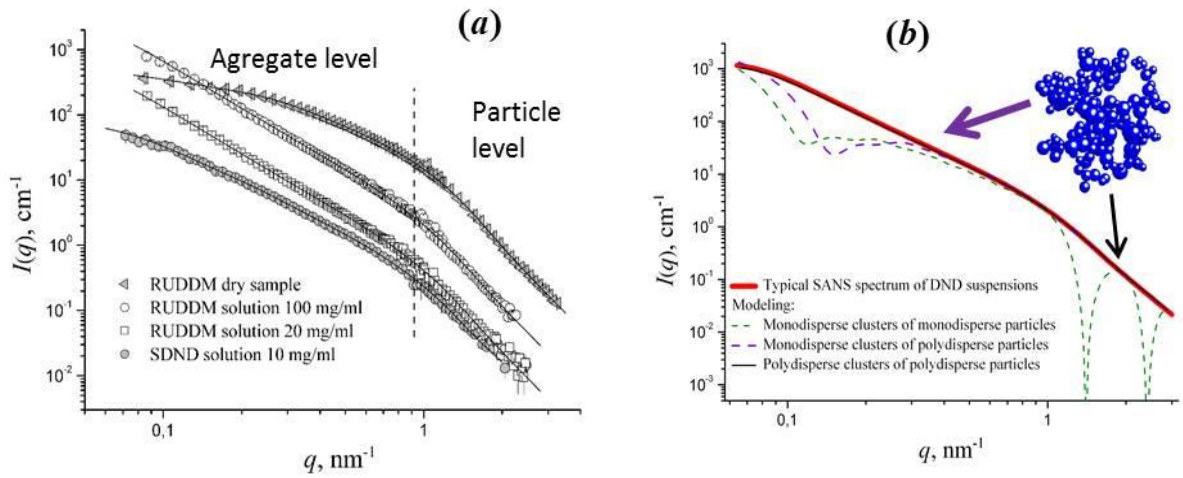

a) b)

Fig. 14. (a) Experimental curves of small-angle neutron scattering (YuMO, IBR-2) from commercial aqueous dispersions of detonation nanodiamonds, RUDDM (Real-Dzerzhinsk Ltd.) and SDND (PlasmaChem GmbH), are compared with the model curves (solid lines) calculated in the exponential/power-law approximation for the two structural levels (indicated in the graph). (b) Calculated curves of small-angle scattering for the model of diffusion-limited aggregation with monodisperse/polydisperse structural units and monodisperse/polydisperse clusters are compared with the curve calculated in the exponential/power-law approximation with the parameters obtained from the analysis of experimental data.

In the frame of biophysical research of fullerene solutions, aqueous solutions of C60 and C70, has been continued. They included the analysis of the cluster structure when placing fullerenes in physiological environment and the study of the interaction of C60 fullerene with antitumor antibiotics, **Fig. 15** [20, 21]. Using SANS and tests on mutagenic activity of Doxorubicin and C60 admixture with Doxorubicin on Salmonella Typhimurium TA98 cells it has been shown that fullerene C60 can act as an interceptor of the antitumor antibiotic Doxorubicin and form hetero-complexes with this drug. The research on the interaction of C60 with Doxorubicin, including SANS, scanning electron (SEM) and atomic force (AFM) microscopy, calorimetry, dynamic light scattering (DLS) and UV-Vis spectroscopy, has been extended to include other aromatic drugs with a similar to Doxorubicin spatial structure such as Landomycin and Cisplatin. New effects of the biological interaction of fullerene C60 in combination with various anticancer drugs have been discovered and described. The work was carried out in collaboration with the Departments of Biology and Physics, Taras Shevchenko National University of Kyiv (Kiev, Ukraine).

In the framework of the research of cluster formation in fullerene solutions the kinetics of dissolution of C60 in a polar solvent, N-methyl-2-pyrrolidone (NMP), has been studied by varing temperature and speed of the component stirring during the solution preparation [22]. This system is characterized by a transition from a molecular solution to a colloidal solution, whose detailed description is of great interest from both fundamental and practical viewpoints. Based on the proposed model of the evolution of the C60/NMP solution, as a result of the competition between dissolution and complex formation, a diagram of the corresponding rates depending on the conditions of the solution preparation has been plotted (**Fig. 16**).

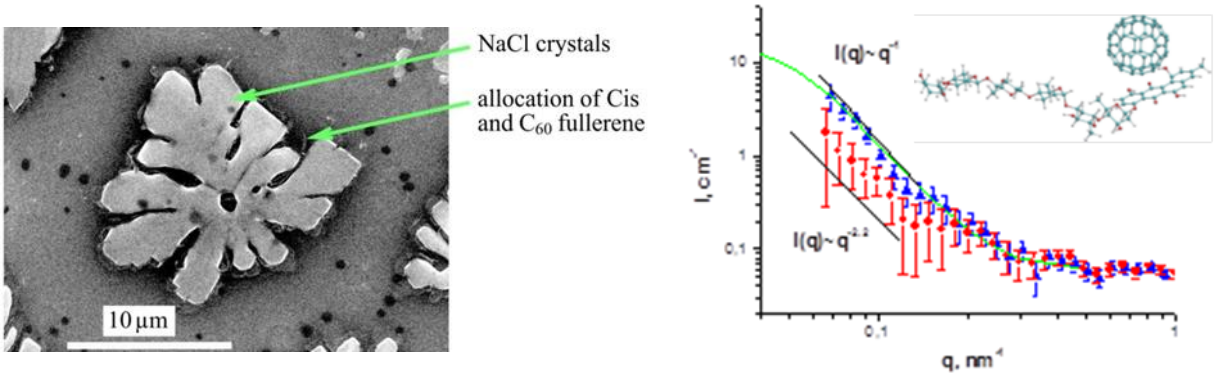

Fig. 15. SEM data for C60/Cisplatin solution (a). SANS for aqueous C60 solution (blue triangles) and mixture of C60 with Landomycin A (red circles). The green line corresponds to the model curve obtained from the inverse Fourier transform. Insert: estimated structure of C60 + Landomycin A complex (b).

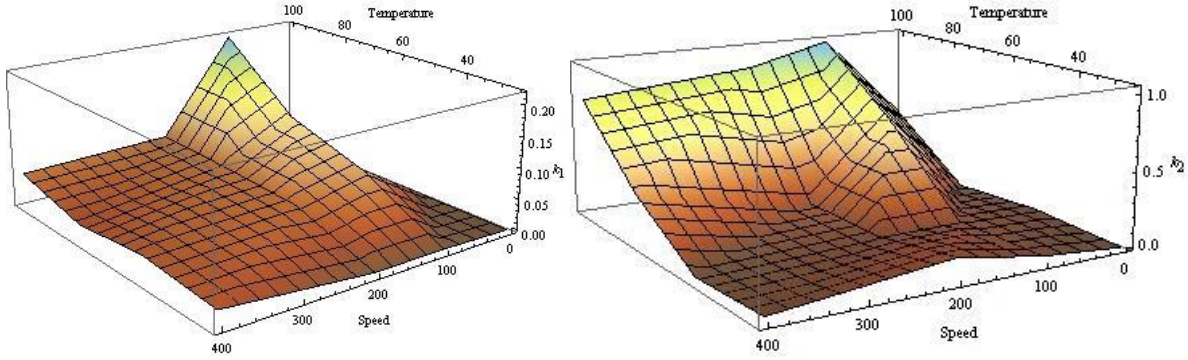

Fig. 16. Diagram of the rates of dissolution (k1) and complex formation (k2) in C60/NMP solution (concentration 0.3 mg/ml) depending on the stirring speed and temperature. The speed values have been obtained from the analysis of the absorption peak intensity in UV-Vis spectra at a wavelength of 330 nm.

3.4. Investigation of layered nanostructures

In the framework of the studies on improving the performance of lithium batteries, a series of experiments on neutron reflectometry (GRAINS reflectometer) to study electrochemical interfaces of liquid electrolyte/solid electrode have been carried out (**Fig. 17**). From the specular reflectivity analysis, the formation of a solid-electrolyte interphase (SEI) on the surface of the electrode (Cu) has been concluded, as well as the lithium electrodeposition and growth of parasitic dendritic structures during the operation of an electrochemical cell have been tracked. The obtained profiles of the scattering length density perpendicular to the electrode surface have made it possible to analyze different modes of SEI formation, as well as the formation and growth of nanometer lithium layers of different roughness on the initially formed SEI. It has been shown that neutron reflectometry can be effectively used for *in situ* characterization of lithium plating on metal electrodes [23]. The study has been performed in collaboration with the Department of Chemistry, Moscow State University (Moscow, Russia).

Neutron studies on the modification of the magnetic state in the ferromagnetic layered nanostructure Ta/V/$Fe_{0.7}V_{0.3}$/V/$Fe_{0.7}V_{0.3}$/Nb/Si under the influence of superconductivity were continued (**Fig. 18**). In the temperature range of 1.5-8 K where niobium and vanadium layers are superconducting, different temperature dependences of neutron scattering from the clusters in this magnetic nanostructure have been detected for the cases of (i) structure in a weak magnetic field of 20 Oe, (ii) structure with residual magnetization after magnetization in a field of 2 kOe, and (iii)

structure in a constant magnetic field of 1 kOe. This indicates that the influence of superconductivity on the state of the magnetic clusters in the layered structure depends on the magnetic field strength. Using the real time reflectometry the temperature dependences of neutron scattering have been measured. They showed a characteristic relaxation time within several tens of minutes for the magnetic state of the layered structure Ta/V/$Fe_{0.7}V_{0.3}$/V/$Fe_{0.7}V_{0.3}$/Nb/Si. The dependences associated with the creep of the magnetic flux in the magnetic non-superconducting structure and oppositely directed creep in the superconducting structure have been observed.

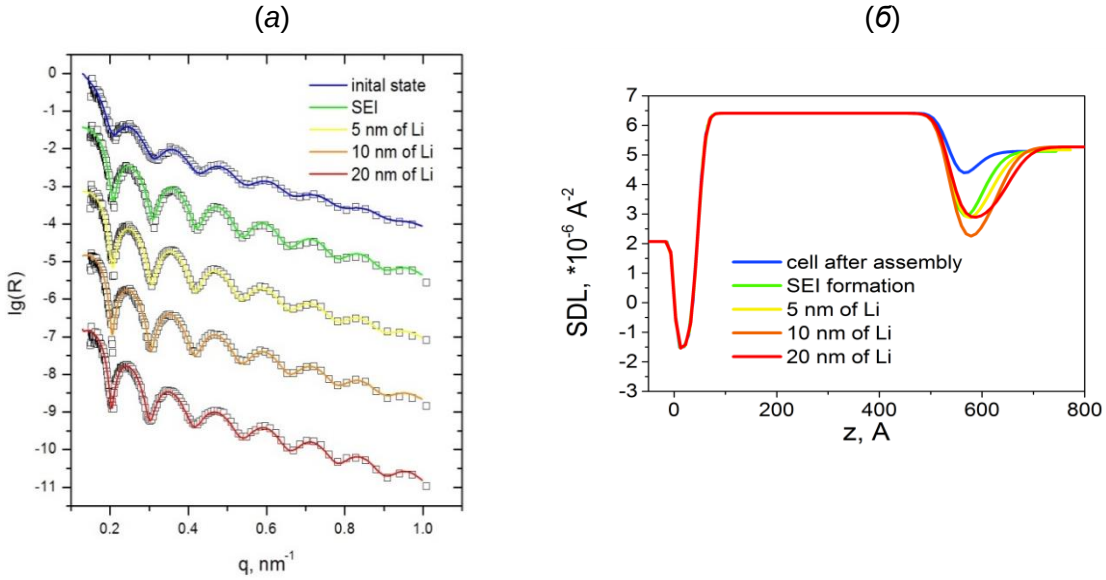

Fig. 17. (a) Experimental neutron specular reflectivity curves (points) for a copper electrode at the interface with the electrolyte at different current and voltage supply modes. (b) Resulting scattering length density profiles for different modes presented in (a) with indicated characteristic thicknesses of deposited lithium.

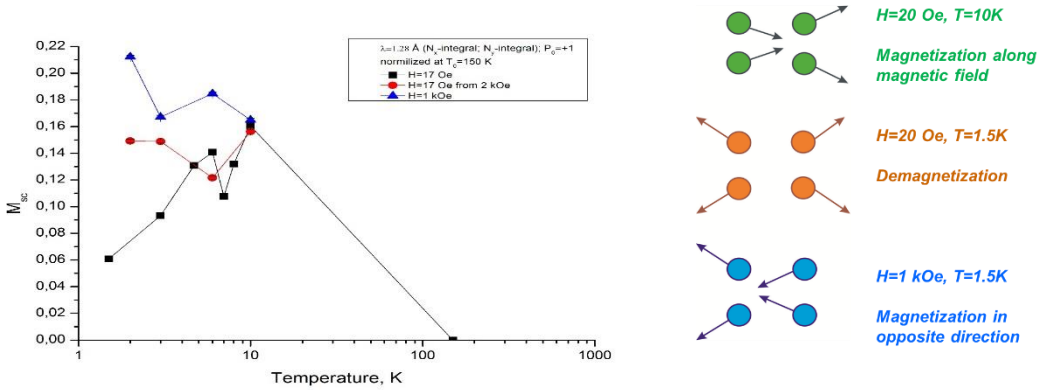

Fig. 18. Temperature dependences of neutron scattering from magnetic clusters in ferromagnetic layered nanostructure Ta/V/$Fe_{0.7}V_{0.3}$/V/$Fe_{0.7}V_{0.3}$/Nb/Si in various magnetic fields (left) and a schematic representation inllustrating the behavior of the magnetic moments of the clusters (right).

In layered structures S1/FM/S2 consisting of ferromagnetic and superconducting layers, the effect of superconductivity on ferromagnetism has been studied by using reflectivity and scattering of polarized neutrons. It has been shown experimentally that at low temperatures magnetic structures with linear dimensions in the range from 5 nm to 30 μm are formed. At temperatures below the superconducting transition, the magnetization of the magnetic structures in the vanadium and niobium layers is suppressed by superconductivity. **Figure 19** demonstrates

for different structures that the neutron scattering diminishes as the temperature decreases from 8 to 1.5 K. Also, **Fig. 19** shows how the structure of the cluster system at 8K is transformed into the structure at 1.5 K.

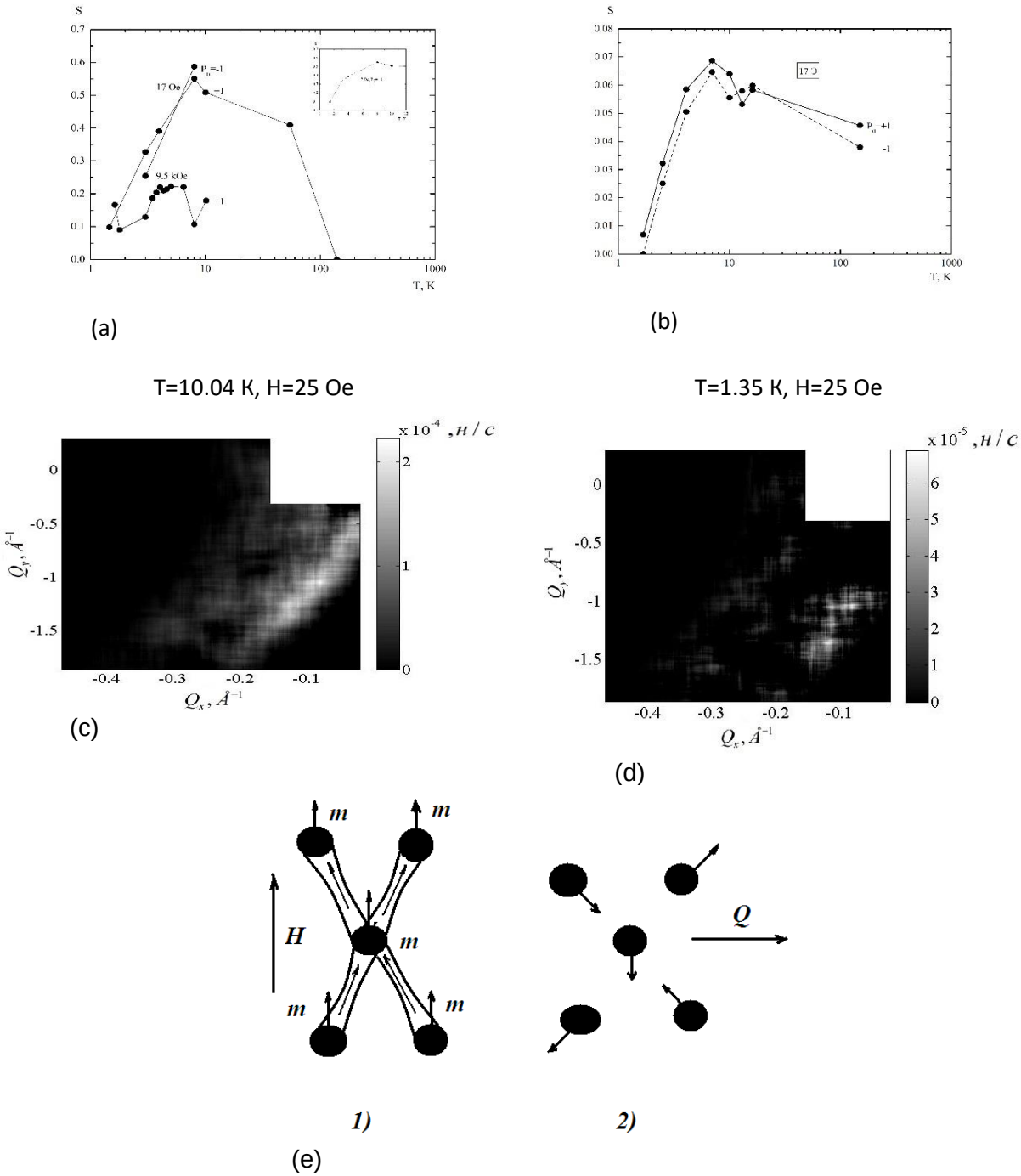

Fig. 19. Dependence of the neutron scattering coefficient $S(T)$ for the structure V(150nm)/(FM(7%)+V(50%)+Nb(43%)(25 nm))/Nb(150 nm) at H = 17 Oe and 9.5 kOe (a). The dependence of the neutron scattering coefficient $S(T)$ for the structure V(150nm)/(FM(7%)+V(43%)+Nb(43%)+Cr(7%))(25 nm)/Nb(150 nm) at H = 17 Oe (b). The contours of the neutron scattering intensity on the plane of transfer wave vectors Qy-Qx at H = 25 Oe and T = 10.04 K (c) and 1.35 K (d). The structure of the cluster system at 8 K (1) and 1.5 K (2) (e).

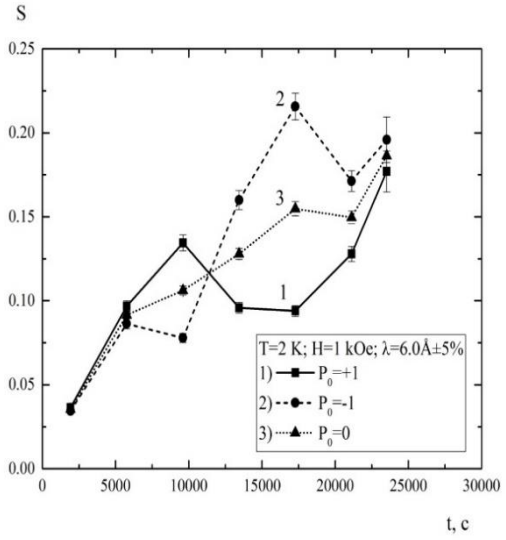

(a)

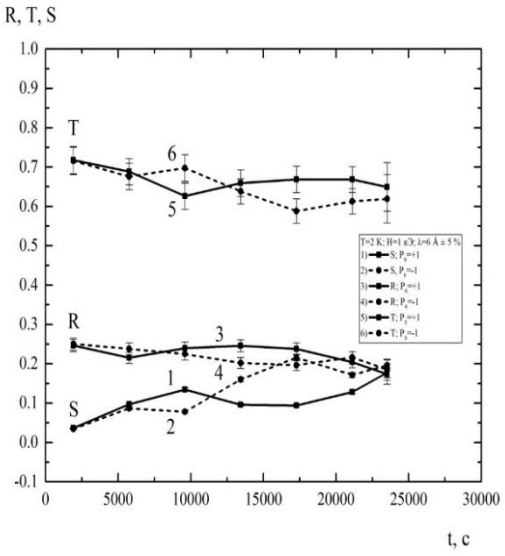

(b)

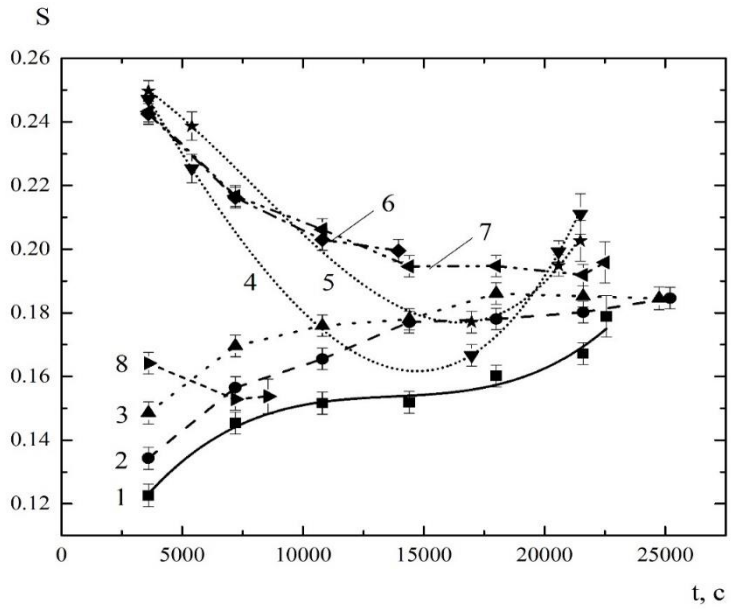

(c)

Fig. 20. Dependence $S(t)$ in magnetic field of 1 kOe at temperature of 2 K for λ = 6 Å and P_0 = +1, −1 and 0 (a). Time dependences for coefficients of transmission T, reflection R and scattering S (b). Dependence $S(t)$ at T = 3 K: P_0 = +1 at H-values: 17 Oe (1), 1 kOe (2), 2 kOe (3), 4 kOe (4), 6 kOe (6), 7 kOe (7) and 8 kOe (8); P_0 = −1 and H = 4 kOe (5) (c).

Using the *in situ* reflectometry of polarized neutrons the magnetic state of a superconducting-ferromagnetic layered structure Ta/V/FM/Nb/Si has been studied. The relaxation of a non-uniform magnetic state of the structure with a characteristic time of a few hours was observed at temperatures both above and below the superconducting transition points in the structure layers. The character of the time dependence of the neutron scattering depends on the magnitude of the magnetic field H, temperature and neutron polarization. **Figure 20** shows the time dependence for the coefficient of neutron scattering. The dependence on polarization due to the scattering from magnetic clusters can be seen. The moments of the clusters are reoriented from the initial direction along the field to the direction against the field. There is also a scattering

contribution which is independent of polarization and caused by the formation of a domain structure with time.

At a large field of 4 kOe (curves 4 and 5, **Fig. 20c**), in early stages there is a depinning of superconducting vortices in the mixed state of superconducting layers of vanadium and niobium, which is changed to the motion of cluster moments. Thus, apparently it was for the first time when neutron reflectometry (coherent propagation - reflection and transmission, as well as GISANS) was used to study the relaxation of the magnetic state and observe relaxation in a hybrid structure consisting of ferromagnetic and superconducting layers. In this case, the characteristic time of the change in the magnetic state of the systems of clusters, domains and vortices was a few hours with a several percent accuracy in the time dependence measurement. The measurement of the time dependences for the coefficients of scattering, reflection and transmission occurring under changes in the average and local potentials of the interaction of neutrons with the medium, was an effective method for identifying types of magnetic systems in the layered structures. In principle, a potential increase in the intensity of the neutron beam at the REMUR spectrometer used in the present study could allow one to achieve time resolution of a few minutes in studies of irreversible processes.

3.5. Investigation of biological nanosystems, lipid membranes and lipid complexes

The visual pigment rhodopsin is a typical representative of the vast family of receptors coupled to G-proteins (GPCR). GPCR in membranes function in dimeric or oligomeric states. However, for rhodopsin and for the whole A class of rhodopsin-like GPCR the functional role of the dimeric state has not yet been established. A supramolecular organization of rhodopsin in photoreceptor membranes is currently much debated. The structural organization of the photoreceptor membranes has been investigated by small-angle neutron scattering with the contrast variation (**Fig. 21**). It has been found that rhodopsin has an unusually high packing density in the photoreceptor membrane with the distance between protein molecules of about 56 Å [24]. With a high probability the data obtained assume a monomeric character of rhodopsin molecules in the photoreceptor membrane.

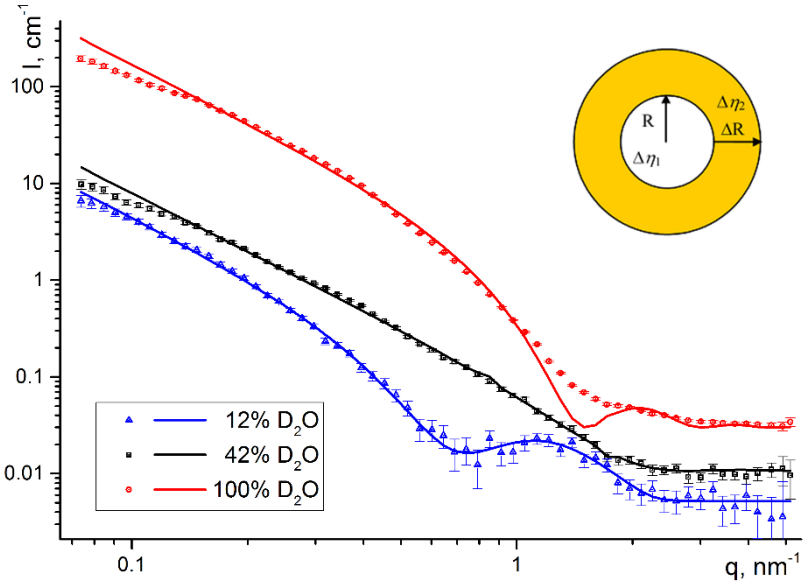

Fig. 21. Small-angle neutron scattering curves from a photoreceptor membrane measured with the contrast variation.

An ability to separate cells from the environment is one of the most important functions of biological membranes. The violation of the membrane integrity causes the cell death. However, local and short-term changes in the membrane integrity leads to the creation of a new structure by

cell fusion/fission. Fusion is the basis of the most important physiological processes such as exocytosis, secretion, formation of secondary lysosomes. In addition, *in vitro* targeting cell fusion by various fusion agents is widely used to solve a number of problems in biomedicine and biotechnology. Dimethyl sulfoxide (DMSO) is one of the fusion agents. In the presence of DMSO, pores in membranes appear, thereby increasing permeability and reducing stiffness of the membrane, which in turn initiates the fusion process. DMSO is toxic to living cells. Diethyl sulfoxide (DESO) is less toxic than, for example, DMSO and glycerol, to *E. coli*. Apparently, the mechanism of the interaction of DESO and DMSO with biological membranes is identical. The SANS analysis of the influence of the DMSO and DESO concentration on structural and phase transitions in phospholipid membranes has been carried out. It has been shown that fusion occurs at a lower molar concentration for DESO than for DMSO. DESO (like DMSO) increases the temperature of the main phase transition (T_f). However, in the presence of DMSO the phase transition occurs at a lower temperature (T_f = 35.2°C and 33.6°C) and in a narrower temperature range than in the presence of DESO at the same molar concentration of sulfoxides.

The process of the spontaneous formation of phospholipid vesicles in the presence of calcium ions has been studied by small-angle neutron scattering. For the first time, the behavior of the intermembrane distance in a transitional region for membranes in both liquid and gel phases has been investigated in detail. It has been shown that the transition of a system from the bound state to the unbound state in both phases is of continuous character. If for the liquid phase this result predicted in many theoretical works was expected, the data obtained for the gel phase contradict most of the previously published works. The theoretical investigations concerning the gel phase indicate that the addition of calcium ions to multilayered lipid membranes should cause for the membranes a sharp transition from the bound state to the unbound state, since there are no ondulations in the gel phase (membrane is "harder" than it is in the liquid phase). However, our studies have shown that the influence of the ondulation forces on the membrane interaction shoud be taken into account. Thus, our experimental results confirm the hypothesis of R. Lipowski (1986) about a possible continious character of the transition. The critical concentrations of calcium ions (0.3 mM for the gel phase and 0.4 mM for the liquid phase) when the analyzed transition takes place have been obtained. In addition, the binding constants for calcium ions with lipid membranes (22 M-1 in the gel phase and 24 M-1 in the liquid phase) have been determined.

It is well known that fermentative systems of oxidative phosphorylation in mitochondria can operate in two states - in a state of supercomplex and in a dissociated state. The comprehensive studies have shown that heart mitochondria operate in the state of supercomplex in a wide range of tonicities of incubation media. This result has been obtained by the polarographic method using the double inhibitor technique by Baum. The investigation of mitochondrial ultrastructure by the methods of electron microscopy (EM) and small-angle neutron scattering (SANS) under conditions of normal tonicity (300 mOsm - isotonia) and low-amplitude swelling (120 mOsm - hypotonia) has proved the existence of two types of mitochondrial ultrastructure. Using EM, it has been found that the mitochondrial cristae in hypotonic and isotonic conditions have different shape and thickness. The tomography method has demonstrated a folded configuration of the cristae. The studies of the ultrastructure of heart mitochondria by methods of EM and inhibition analysis have been carried out on intact functioning mitochondria in the presence of respiratory substrates. Using the SANS method it has been shown that in hypotonic and isotonic media highly-organized lipid-protein lamellar structures are formed in mitochondria. The formation of lipid structures has been demonstrated by using the contrast variation technique (variation of the fraction of heavy water in a solution). Also, it has been shown that the thickness of the mitochondrial cristae depends on the medium tonicity. Thus, the data obtained from the investigation of the functioning and structure of mitochondria suggest the existence of two states for the system of oxidative phosphorylation, which forms cristae with different structural parameters [25].

The passive transport of particles through lipid membranes in different lipid phase states has been investigated by inelastic X-ray scattering. It is known that the passive transport of molecules through a cell membrane depends on thermal motions of lipids. However, the nature of

transmembrane transport and its precise mechanism are not fully understood. The phonon excitations in a lipid bilayer of 1,2-dipalmitoyl-*sn*-glycero-3-phosphocholine above and below the main phase transition temperature have been measured. In the gel phase, for the first time the presence of transverse high-frequency modes has been shown. The modes are terminated when the lipids change into the liquid phase. This termination is apparently due to the formation of short-lived nanometer lipid clusters and transient pores which facilitate the passive molecular transport through the lipid bilayer. The obtained data suggest that the phononic motion of the lipid hydrocarbon tails provides an effective mechanism of passive transport [26].

The investigations (diffraction and small-angle scattering of neutrons and synchrotron radiation) of lipid membranes and nanoparticles on their basis have been continued in collaboration with the University of Messina, Italy, and NRC "Kurchatov Institute". The structural organization of vesicular drug carriers, including a vesicular transport system Phospholipovit, has been studied (**Fig. 22**) [27]. Particular attention has been given to the processes of interaction and aggregation of vesicles. The general principles of the organization of vesicular drug carriers have been formulated.

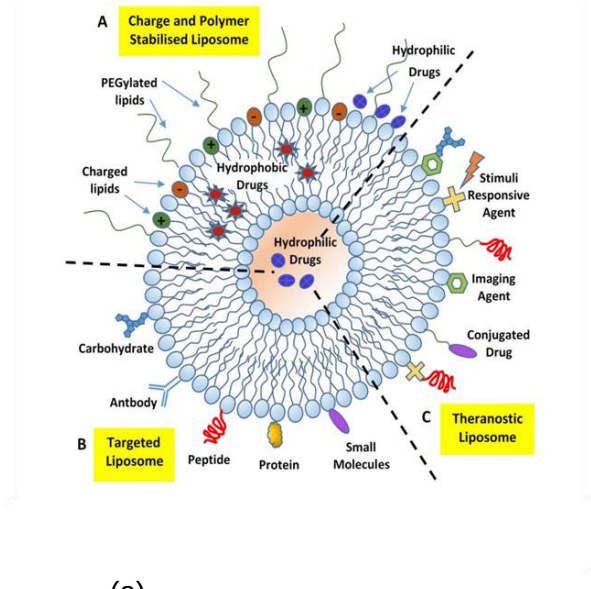

(a)

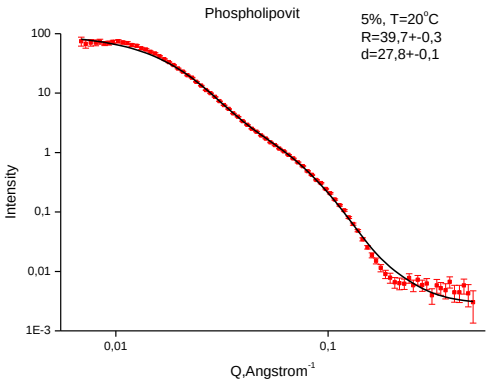

(b)

Fig. 22. Schematic representation of vesicular transport systems of various types for drug delivery (a). Experimental and calculated curves of small-angle neutron scattering (YuMO) for vesicular transport system Phospholipovit (b).

In the framework of the study of the structure and properties of membranes the experiments on molecular dynamics simulation (MD) and SANS for Ca2+ and Zn2+ cations with the gel phase of a model lipid membrane of dipalmitoylphosphatidylcholine (DPPC) have been carried out. As a result, the formation of oriented multilamellar membranes has been studied. An increase in the bilayer thickness has been revealed for both considered cations at a molar ratio of divalent metal ion to lipid (Me2+:DPPC) of ~1:7. The MD simulations have made it possible to reveal a slight difference in the effect of the cations on the gel-phase of membranes. The study [28] has been performed in collaboration with the Comenius University (Bratislava, Slovakia), a number of research laboratories in the USA and LRB JINR.

Comprehensive studies of the phase transitions, morphology and internal structure of an organogel of 4-heptyloxyphenylolithocholic acid (7OPhOLCA) – a derivative of lithocholic acid (LCA) have been carried out. The obtaining of stable organogels with specified chemical and physical properties is a challenging direction regarding the potential applications in optoelectronics, drug delivery in medicine, regeneration of damaged tissues, etc. The samples of 7OPhOLCA in DMSO-d6 with various concentrations have been studied by the SANS method, as

well as temperature ranges for the sol-gel transition have been determined, **Fig. 23** [29]. It has been shown that the transition temperature decreases with increasing concentration of organogel when heated. The reason for the changes in the internal structure around the sol-gel transition is the destruction of hydrogen bonds, as shown by IR spectroscopy. Furthermore, the analysis of small-angle scattering curves has revealed morphological changes of the studied samples in the gel phase, which had not been initially detected by DSC because of low enthalpy (compared to the phase transitions).

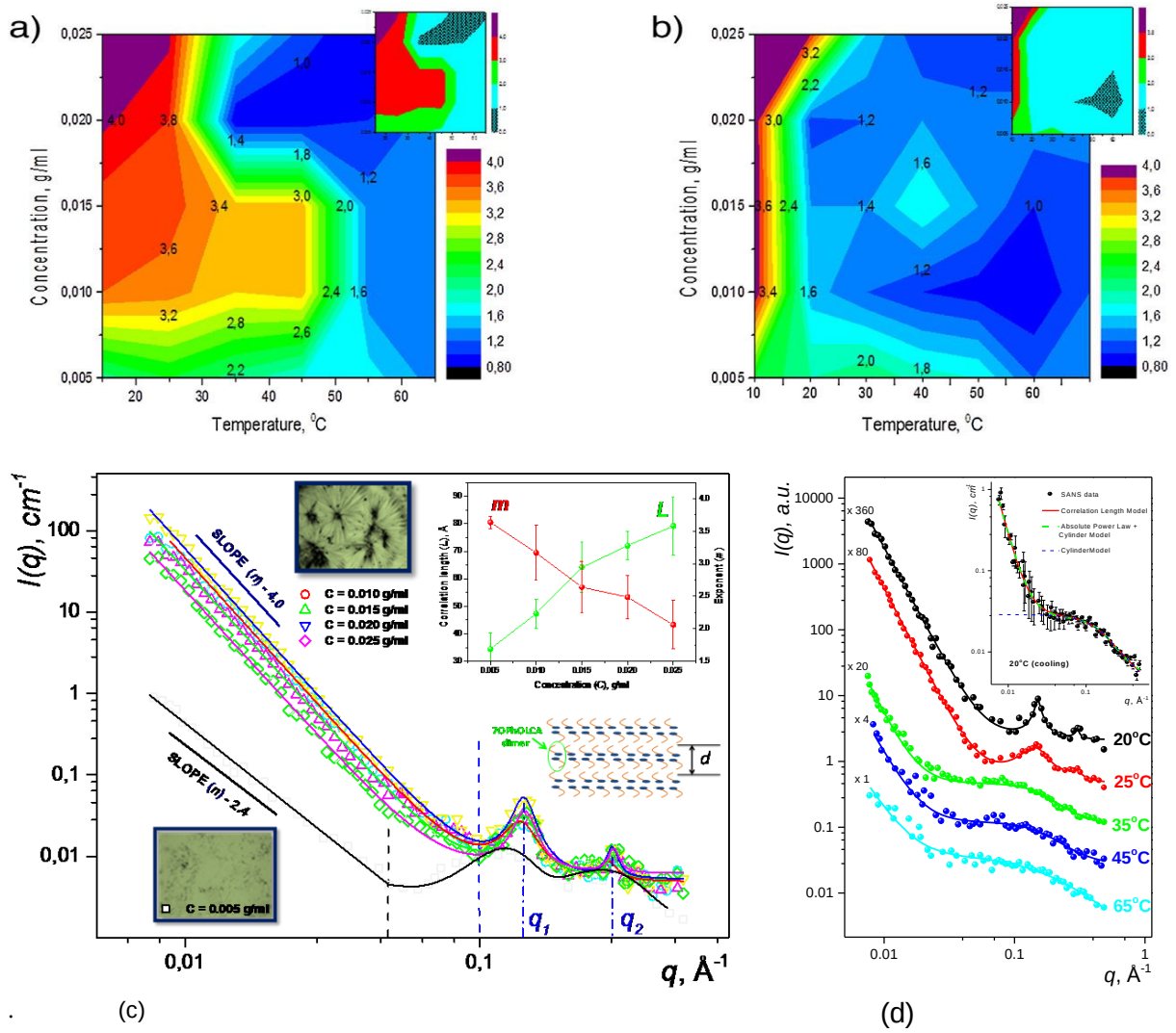

Fig. 23. Sol-gel transition for heating (a) and cooling (b). SANS curves (symbols) with fits (lines) for 7OPhOLCA in DMSO-d6 at concentration C = 0,005, 0,010, 0,015, 0,020, and 0.025 g/ml at T = 10°C after a single heating-cooling cycle (c). Dashed vertical lines divide the ranges of small and large q-values; q_1 and q_2 correspond to the maximum intensity of Bragg peaks. Optical microscopy images were obtained for samples stabilized for 12 hours in quartz cells at T = 10°C. Insert: change in the correlation length, L, and the exponent, m, as a function of concentration of 7OPhOLCA. Changes in the SANS curves with increasing temperature for 7OPhOLCA in DMSO-d6 at C = 0.015g/ml (d). Insert: SANS curves (circles) at T = 20°C during cooling.

In particular, at temperatures above 25°C the lamellar organization of dimers is destroyed. At the same time, no reorganization of hydroxyl groups is observed (IR spectroscopy). In the analysis of the SANS data three models have been proposed. The time stability of organogels has also been studied. It has been found that all the phases observed are reversible and the structure of the studied samples exhibits a memory effect.

3.6. Polymeric materials

Small-angle neutron scattering has been used to study the structural peculiarities of perfluorinated proton conducting polymer samples containing sulfonic groups of Aquivion. A fine structure of polymeric membranes based on a system of proton conducting channels in a perfluorinated polymer matrix has been revealed. The way this fine structure changes has been determined as a function of the equivalent weight of the membrane, and the relation of these changes with the proton conductivity value has also been established. The contrast variation technique has made it possible to study the effect of orientational stretching on the fine structure. It has been found that the stretching is accompanied by an increase in the proton conductivity due to changes in the fine structure of the channel system. Our investigations confirm that a reduction of the side chain length affects the fine structure of the perfluorinated proton conducting membranes. This is accompanied by an improvement in their performance in hydrogen fuel cells [30].

Silver sols synthesized in polymer matrices have been investigated by small-angle X-ray scattering (SAXS) in combination with ultraviolet-visible (UV-VIS) spectroscopy and quasielastic light scattering (QELS). The characteristics of the particle size distribution obtained by each of the methods are in good agreement. It has also been found that there are deviations of the experimentally measured characteristics from the existing theoretical models. The most likely reason for this is that the nanoparticle clusters have a non-spherical shape [31].

The modeling of the glass transition kinetics for polystyrene has been continued. Using different theoretical methods currently applied to polymer systems, a single measurement of the temperature dependence for the heat capacity under heating and cooling has been modeled. It has been shown that for single curves good agreement is achieved, however the resulting model parameters do not allow one to describe correctly the dependence of the glass transition temperature on the cooling rate. In the opposite case, if the dependence $T_g(q)$ is fitted the agreement with a single measurement is of poor quality. Thus, it has been clearly shown that the modeling of glass transition in terms of the general parameters depending on the cooling rate simultaneously with the transition kinetics is impossible within the framework of the existing models [32]. The study has been performed in collaboration with the University of Rostock (Rostock, Germany).

3.7. Atomic and molecular dynamics

In recent years, much interest has been shown in the study of hydrogen-bonded, donor-acceptor type supramolecular co-crystals for their potential use as functional materials with semiconducting and/or ferroelectric properties arising due to the electron- and proton-transfer phenomena. A comprehensive study of the crystal structure and molecular dynamics of co-crystals of bromanilic acid with 2,6-dimethylpyrazine (BrA: 2,6-DMP) 1:1 has been carried out using the methods of single-crystal X-ray diffraction, neutron spectroscopy (NERA spectrometer) and complementary spectroscopic methods, **Fig. 24** [33]. To interpret the experimental results, theoretical calculations have been performed as well.

The structural analysis has revealed that the system under study crystallizes in the monoclinic P21/c space group, with four molecular units per unit cell. The crystal structure can be described as an infinite net of antiparallelly oriented hydrogen bonded molecular chains (**Fig. 25**). The intermolecular analysis has revealed the nonequivalency of the moderate strength hydrogen-bonding interactions and the presence of multiple specific intermolecular forces. The theoretical calculations using Hirschfeld surface approximation and reduced density gradient approaches have exposed the role of stacking interactions and weak van der Waals forces in the stabilization of the crystal structure. The analysis of vibrational properties was performed using the methods of neutron and optical spectroscopy (mid-, far- and terahertz ranges).

The theoretical analysis of the vibrational spectra was made in the framework of DFT in the semilocal approximation taking into account semiempirical van der Waals corrections. Despite the quasiharmonic approximation, good agreement between the theoretical and experimental spectra was achieved. In particluar, the significant influence of the long-range dipole coupling on the IR spectrum and the effect of the structure on the vibrations with small wave numbers have been revealed.

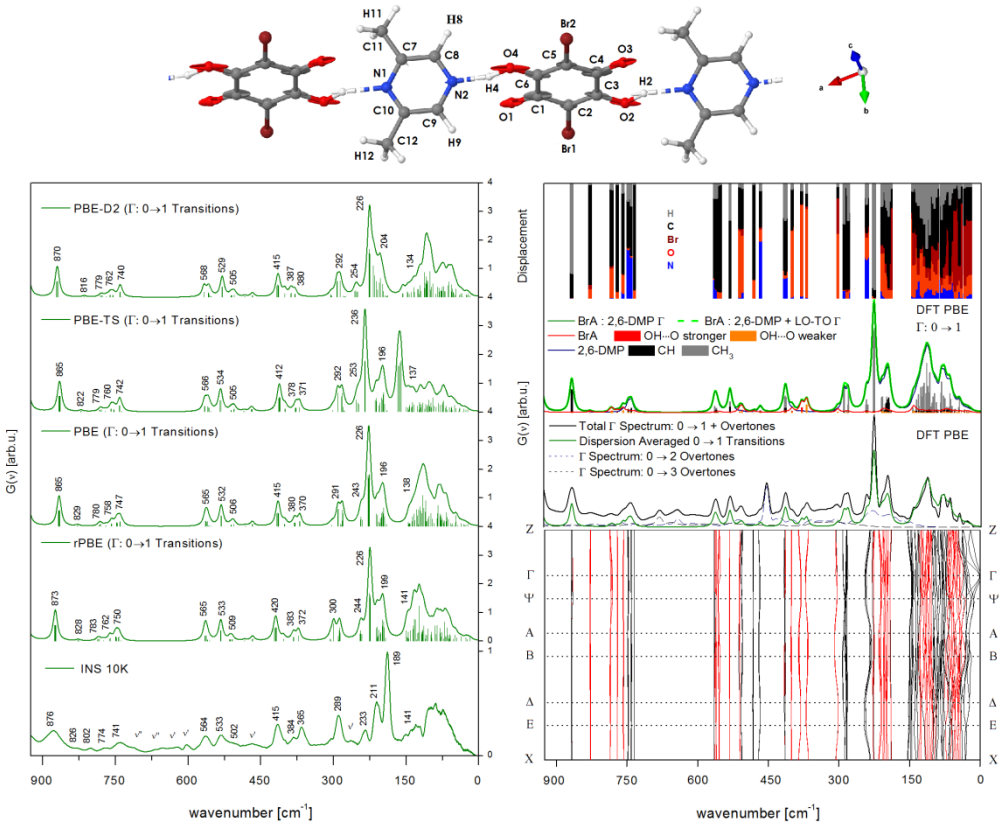

Fig. 24. Molecular structure, inelastic neutron scattering spectra (NERA 10K) and theoretical calculated vibrational spectra (for 0 → 1 transitions) of BrA:2,6-DMP (1:1) in the frequency range below 925 cm^{-1}. The theoretical spectra are given for both constrained (rPBE; PBE) and fully (PBE-TS; PBE-D) optimized crystal structures. Also, calculated phonon dispersion curves along with the vibrational density of states decomposed into partial density contributions of each molecular fragment are selectively presented. In addition, the dispersion averaged spectrum is given along with the total Γ-point spectrum including the overtone contributions.

Inhibitors of 3-hydroxy-3-methylglutaryl coenzyme A (HMG-CoA) reductase are among the most effective and widely used drugs for lowering the cholesterol level, known as statins. Statin monotherapy is generally well tolerated and has minimal side effects. The first HMG-CoA inhibitor approved by FDA (Food and Drug Administration, USA) – lovastatin (MEVACOR®; ALTOCOR® & ALTOPREV®), below referred to as LOV was mainly used to control hypercholesterolemia (**Fig. 25**).

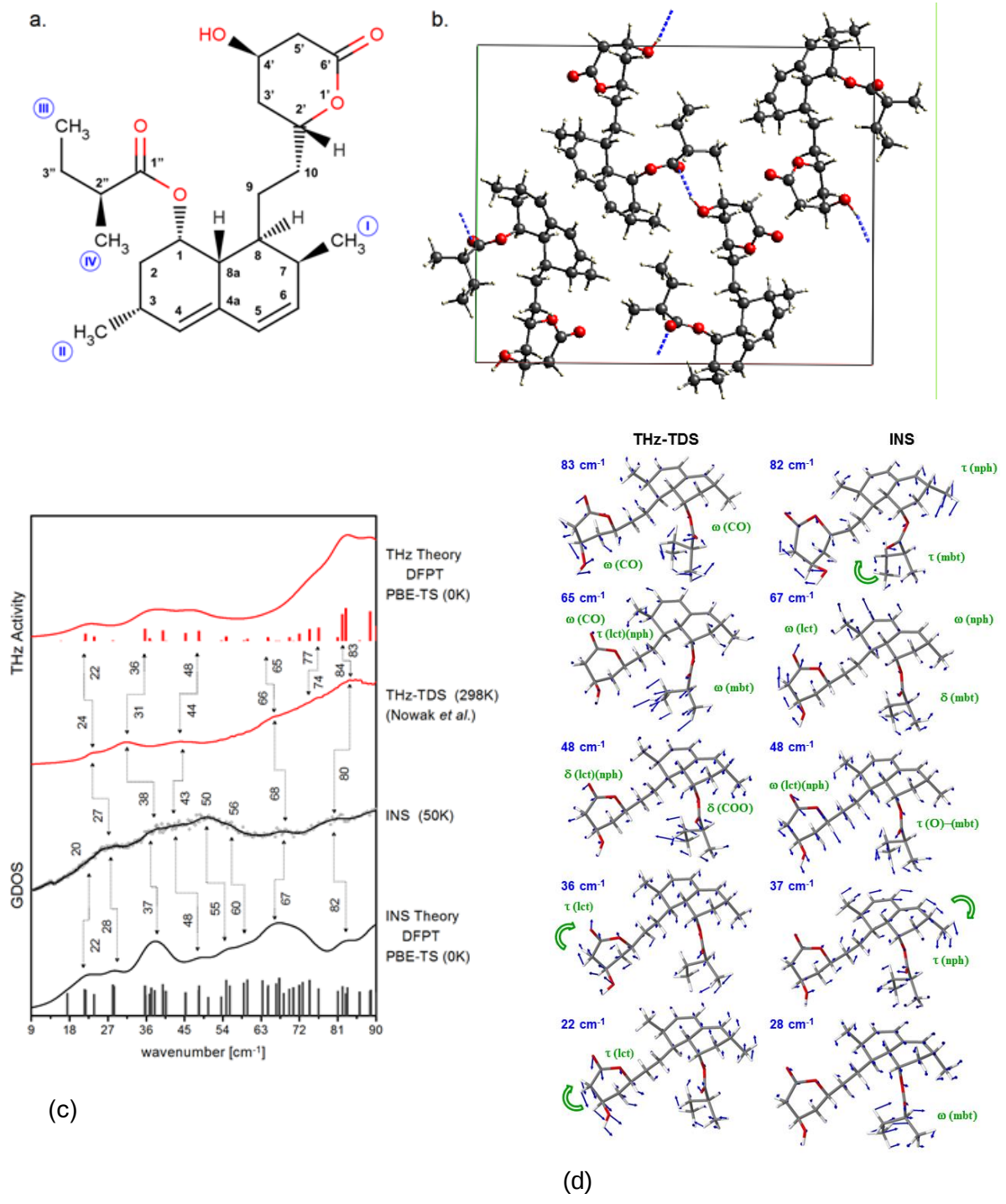

Fig. 25. Molecular formula of lovastatin (LOV; (1S,3R,7S,8S,8aR)-8-{2-[(2R,4R)-4-Hydroxy-6-oxooxan-2-yl]ethyl}-3,7-dimethyl-1,2,3,7,8,8a-hexahydronaphthalen-1-yl (2S)-2-methylbutanoate) with marked methyl groups (I-IV) (a). Crystal structure of lovastatin (space group $P2_12_12_1$) optimized using PW - DFT (PBE-TS) (b). Comparison of theoretically calculated (harmonic approximation DFPT PBE-TS) and experimental vibrational spectra of lovastatin according to the data of neutron (IINS) and optical terahertz spectroscopy (data by Nowak *et al*. Acta Poloniae Pharmaceutica in Drug Research, Vol. 72 No. 5 (2015) pp. 851-866) (c). The most important vibrational modes of lovastatin contributing to the INS and THz-TDS spectra. The eigenvectors obtained from the harmonic PBE-TS calculations are shown in the projection of one molecule.

In the LOV molecule three main parts can be distinguished – lactone ring (lct), naphthalene fragment (nph) and methylbutanoate chain (mbt). The molecules are linked by hydrogen bonds O···HO (**Fig. 25**). Hydrogen bonds bind lactone rings (methyl group) with methylbutanoate chains (carbonyl group). The second carbonyl group of lactone rings is unbound.

In collaboration with the Adam Mickiewicz University (Poznan, Poland), atomic and molecular dynamics of lovastatin has been studied by ^{1}H NMR and inelastic neutron scattering complemented by theoretical ab-initio calculations using the PW-DFT method. A consistent molecular dynamics model has been obtained, which can be later used to describe the dynamics of other alternative drug forms and tendencies to amorphization. It has been found that the molecular dynamics of lovastatin is determined by the motions of methyl groups and the conformational disorder in the methylbutanoate fragment. The vibrational dynamics of lovastatin was analyzed focusing on the energy transfer range with low wave numbers, which was experimentally studied by neutron (INS) and terahertz (THz-TDS) spectroscopy. The theoretical calculations made it possible for the first time to describe with a high accuracy the phonon spectrum of lovastatin in this region (**Fig. 25**). It should be noted that the main contribution to the inelastic neutron scattering spectra is from vibrations of hydrogen-containing molecular groups, which are the most mobile ones for the movable mbt fragment contributing to the most intense vibrational mode. At the same time, the primary contribution to the terahertz spectra is from the most polar molecular groups containing oxygen and included in the lct fragment. The corresponding normal vibrational modes are shown in **Fig. 25**. The most intensive spectral features for THz-TDS are due to the modes related to the vibrations of hydrogen bridges O···O in a range of above 65 cm^{-1}, while the modes in a range of below 65 cm^{-1} are determined by the vibrations of the whole lct fragment. This set of modes is of a general nature without intending to be bound to a particular LOV compound and can be used in further studies of statins.

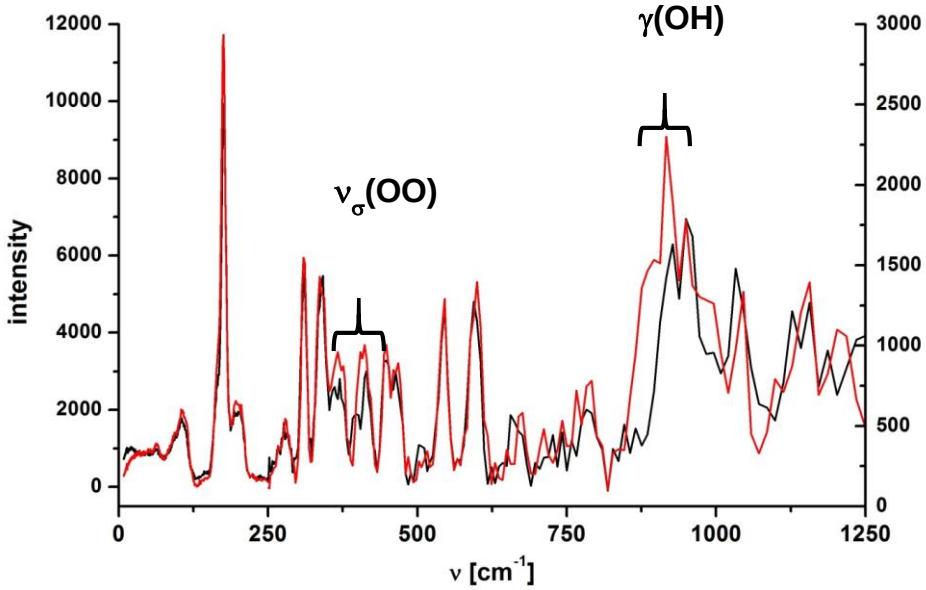

Fig. 26. Spectra of inelastic scattering (NERA, IBR-2, JINR) from polymorphic forms of o-hydroxy-acetophenone (red line) and its mono-deuterated analogue. The left and right Y-scales correspond to the spectral ranges of 0-250 cm^{-1} and 250-1250 cm^{-1}.

The experimental and theoretical investigations of the dynamics of a nitrated derivative of ortho-hydroxy acetophenone have been carried out. To estimate the barriers of the conformational changes and folding, the potential barriers for the nitro group rotation and hydroxyl group isomerization were calculated. Two polymorphic forms of this compound were obtained by slow and rapid evaporation of the polar and nonpolar solutions, respectively. Both polymorphs were investigated by means of infrared, Raman and neutron spectroscopy (**Fig. 26**), nuclear quadrupole

resonance, differential scanning calorimetry, and theoretical calculations using the DFT method were performed as well. In one of the polymorphs phase transitions were detected. The position of the nitro group and its influence on the crystal structure were analyzed by X-ray diffraction. A full spectrum analysis of the vibrational spectra for the interpretation of the two conformations was performed. On the basis of the obtained data the nature of the phase transition has been explained [34].

3.8. Applied research

Among traditional applied investigations in the NICM Department are the experimental studies of internal stresses and texture of rocks and minerals, determination of internal stresses in bulk materials and products, including construction materials and components of machines and devices. For the most part, these investigations are carried out using neutron diffraction.

On the FSD diffractometer, experiments to study the distribution of residual stresses in welds after using various welding methods have been performed (**Fig. 27)**. These studies have been carried out in collaboration with the Institute of Electronics, BAS (Sofia, Bulgaria) and Brandenburg University of Technology (Germany). Residual stresses in a toothed gear of a sports car transmission gearbox after electron beam welding have been studied. It has been found that in the weld region and adjacent heat-affected zone (HAZ) the residual stresses and microstrains have minimum values. In the region remote from the weld the residual stresses are rather large, and their maximum levels reach values of about 500 MPa, which may point to non-optimal parameters of the beam welding.

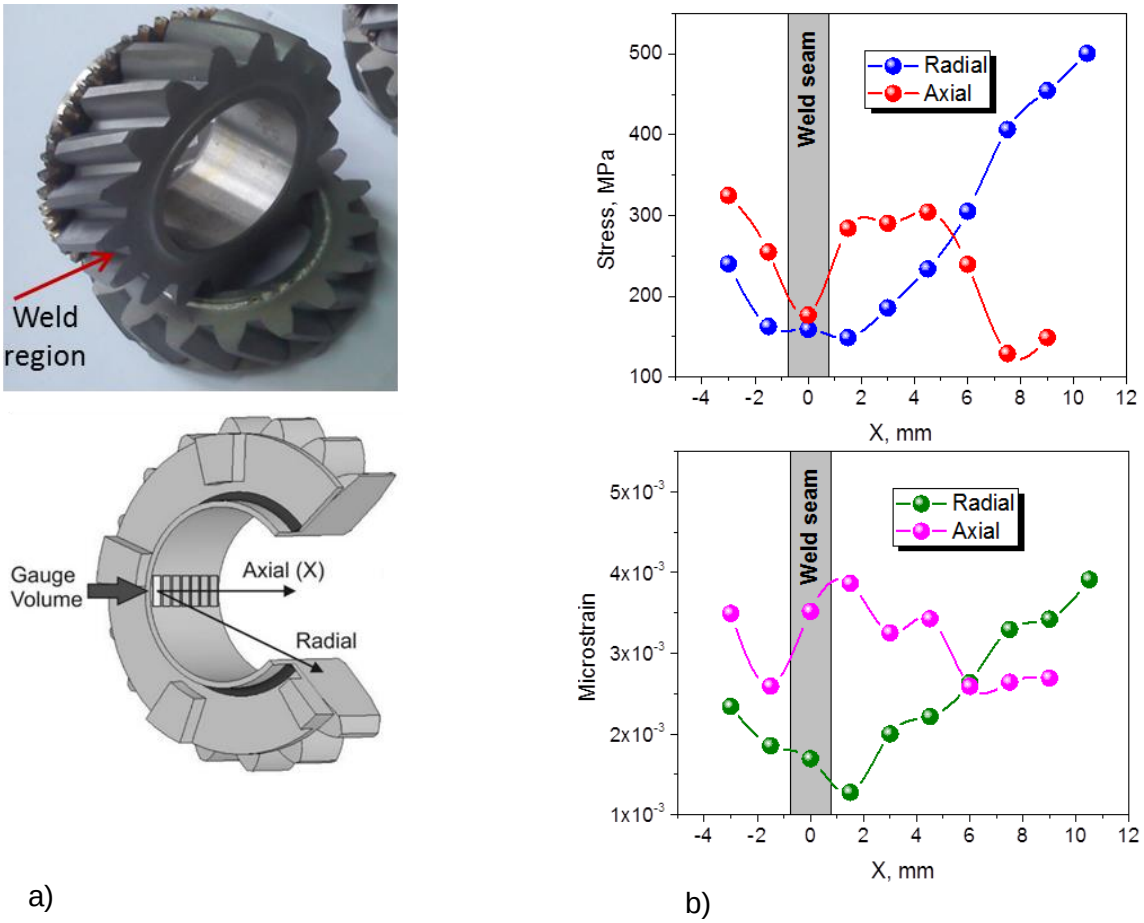

Fig. 27. a) Photo of toothed gears welded by electron beam welding and scheme of the measurement of residual stresses in the toothed gear. b) Distribution of residual stresses (top) and microstrains (bottom) in the toothed gear welded by electron beam welding.

A detailed study of residual stresses has been performed for a plate of size 100x100x10 mm of structural steel S355J2+N welded by laser beam welding (**Fig. 28**). The distribution of residual stresses along the scan coordinate X is of an alternating character, and the maximum-largest is the component of the stress tensor σ_x (~ 400-460 MPa) directed along the weld line and having mainly stretching character in the heat-affected zone. The analysis of the behavior of the peak widths near the weld has shown that the peak broadening depends on the direction [hkl] in the crystal, which is a typical manifestation of the orientation factor of dislocations in respect to the scattering vector. In the given sample the maximum level of microstrains in the material reaches $4.8 \cdot 10^{-3}$, and the position of the maximum in the microstrain distribution coincides with the location of the weld center. Using the obtained data on microstrains the dislocation densities in the material have been calculated.

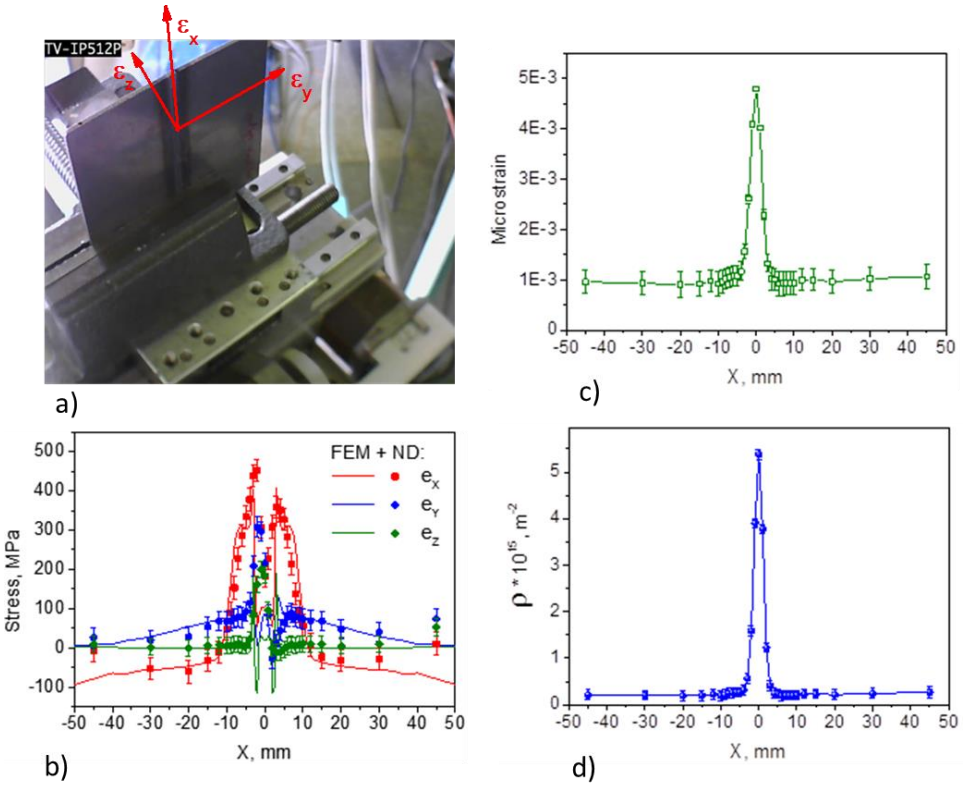

Fig. 28. The sample under study (plate welded by LBW) during the experiment at FSD (a). The arrows indicate the strain tensor components. Experimentally measured distribution of residual stress tensor components in the plate (symbols) welded by LBW (b). For comparison, the results of numerical simulation using the finite element method FEM (solid lines) are presented. Distribution of microstrains in the crystal lattice (c) and dislocation densities (d) obtained from the diffraction data in the plate welded by LBW.

In addition to the neutron diffraction experiments and in the framework of the existing cooperation numerical calculations have been performed by the finite element method - FEM (group of Prof. V.Mikhailov, Brandenburg University of Technology, Germany). The comparison of the neutron data and calculations using FEM shows a good agreement, which supports the validity of the developed theoretical model of the laser welding process. This information can serve as a basis for developing specific technical recommendations to achieve the desired level and profile of residual stresses.

On FSD, experiments to study the distribution of residual stresses in welds after using various welding methods have been continued. In 2016, residual stresses were measured in a massive (thickness ~ 20 mm) sample from structural steel S355J2+N welded with combined

multipass welding: 1st pass – metal welding in shielding gases (MSG-welding), 2nd and 3rd passes – submerged arc welding (SAW-welding), **Fig. 29**.

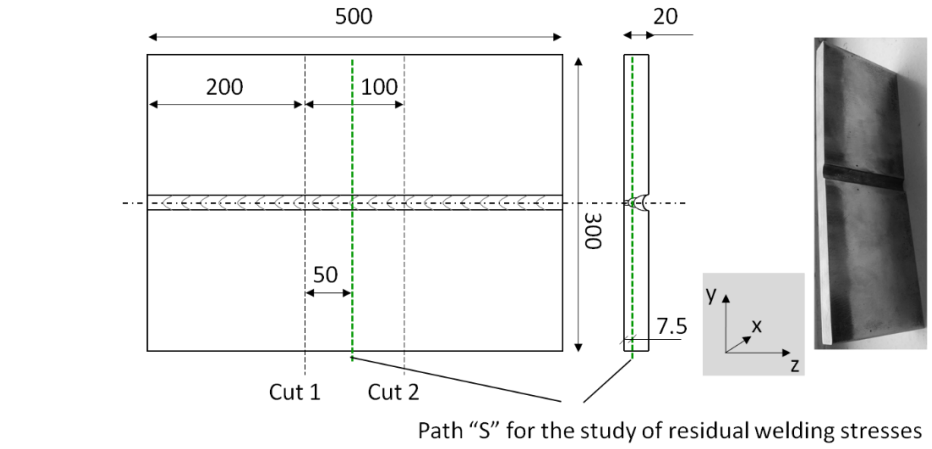

(a)

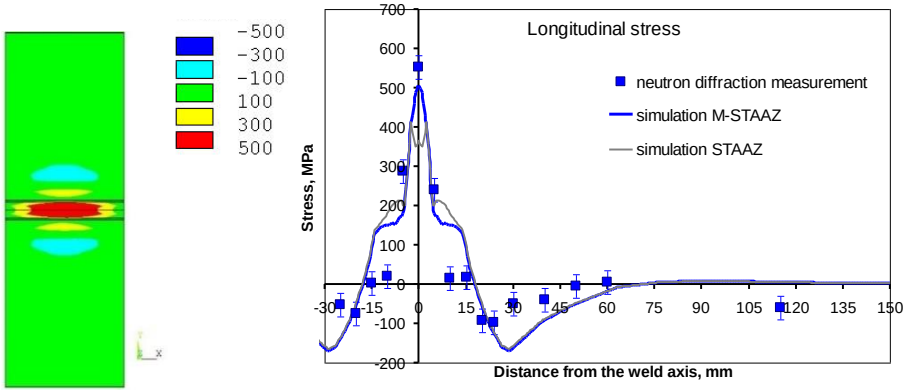

(b)

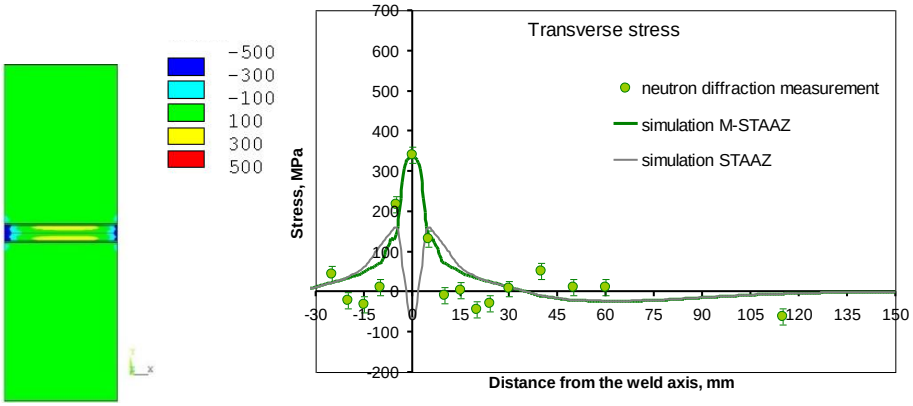

(c)

Fig. 29. Sample cut from a thick (~ 20 mm) plate welded with multi-pass submerged arc welding (SAW-welding). "S" is a scan-line in neutron measurements. Arrows indicate the strain tensor components (X, Y, Z) (a). Full map of distribution of the longitudinal component (σ_X) in the tensor of residual stresses calculated by the finite element method (FEM) and the comparison of the experimentally measured σ_X-values along the scan-line "S" with the results of numerical modeling by the finite element method FEM (solid line) (b) . Full map of distribution of the transverse component (σ_Y) in the tensor of residual stresses calculated by the finite element method (FEM) and the comparison of the experimentally measured σ_Y-values along the scan-line "S" with the results of the numerical modeling by the finite element method FEM (solid line) (c).

In neutron experiments with new radial collimators in the middle part of the sample the residual stress tensor components were measured in a wide X-range across the weld, which were further used to determine the residual stress values (**Fig. 29**). The maximum component is the longitudinal stress tensor component σ_x (~ 550 MPa) directed along the weld which is of the stretching character in the center of the weld. The level of the transverse component of the stress tensor σ_y is significantly lower (~350 MPa), and the level of the normal component σ_z does not exceed 180 MPa.

In addition to the experiments on neutron diffraction, numerical calculations by the STAAZ method have been performed in the framework of the existing cooperation with the research group of Prof. V. Mikhailov (Brandenburg University of Technology, Germany). The comparison of the neutron data and FEM calculations has shown good agreement, indicating the reliability of the developed theoretical model for the multi-pass welding process. This information can serve as a basis for the development of specific technical recommendations to achieve the desired level and profile of residual stresses.

On FSD, a series of TRIP-composites with austenitic matrix and different content of reinforcing ceramic phase of zirconium dioxide ZrO_2 partially stabilized by magnesium (Mg-PSZ) have been investigated at various degrees of plastic deformation (uniaxial compressive load), **Fig. 30**. The study has been done in collaboration with the Freiberg University of Mining and Technology (Freiberg, Germany). At the load values above 650 MPa, the formation of two phases in the austenitic matrix was observed: cubic α'-martensite and hexagonal ε-martensite. The content of ε-martensite reached ~15% for all samples under deformation up to σ = 1100 MPa and then remained almost unchanged until the maximum load values of σ = 1580 MPa. In contrast, the α'-martensite phase exhibited a monotonic increase in the load range from 950 to 1580 MPa. In the ceramic sample of pure zirconium dioxide (100% ZrO_2) two phases were observed: cubic (f ≈ 55%) and tetragonal (f ≈ 45%). The residual deformation of the crystal lattice of the austenitic matrix is of compressive character and increases up to ~10^{-3}. In this case, the crystal lattice deformation in α'- and ε-martensites is more complex and reflects the redistribution of the load between the phases.

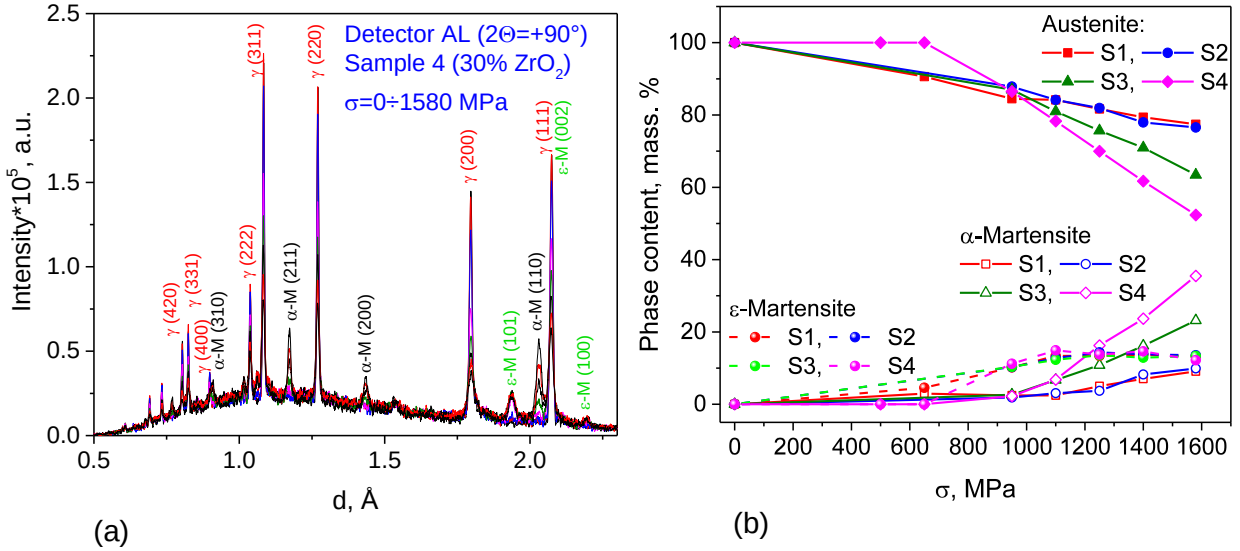

Fig. 30. The change in the diffraction spectra of the TRIP-composites as a function of plastic deformation (a). The change in the phase mass content in the TRIP composites depending on the degree of plastic deformation (b).

Furthermore, under the deformation in the range from 650 to 1580 MPa a noticeable broadening of the diffraction peaks with increasing plastic deformation was observed, which was caused by the variation in the contrast factor of dislocations. For the austenitic matrix the

dislocation densities were evaluated from the peak broadening. They reached the values in the range of $12 \div 20 \cdot 10^{14}$ m^{-2} depending on the content of zirconium dioxide in the composite.

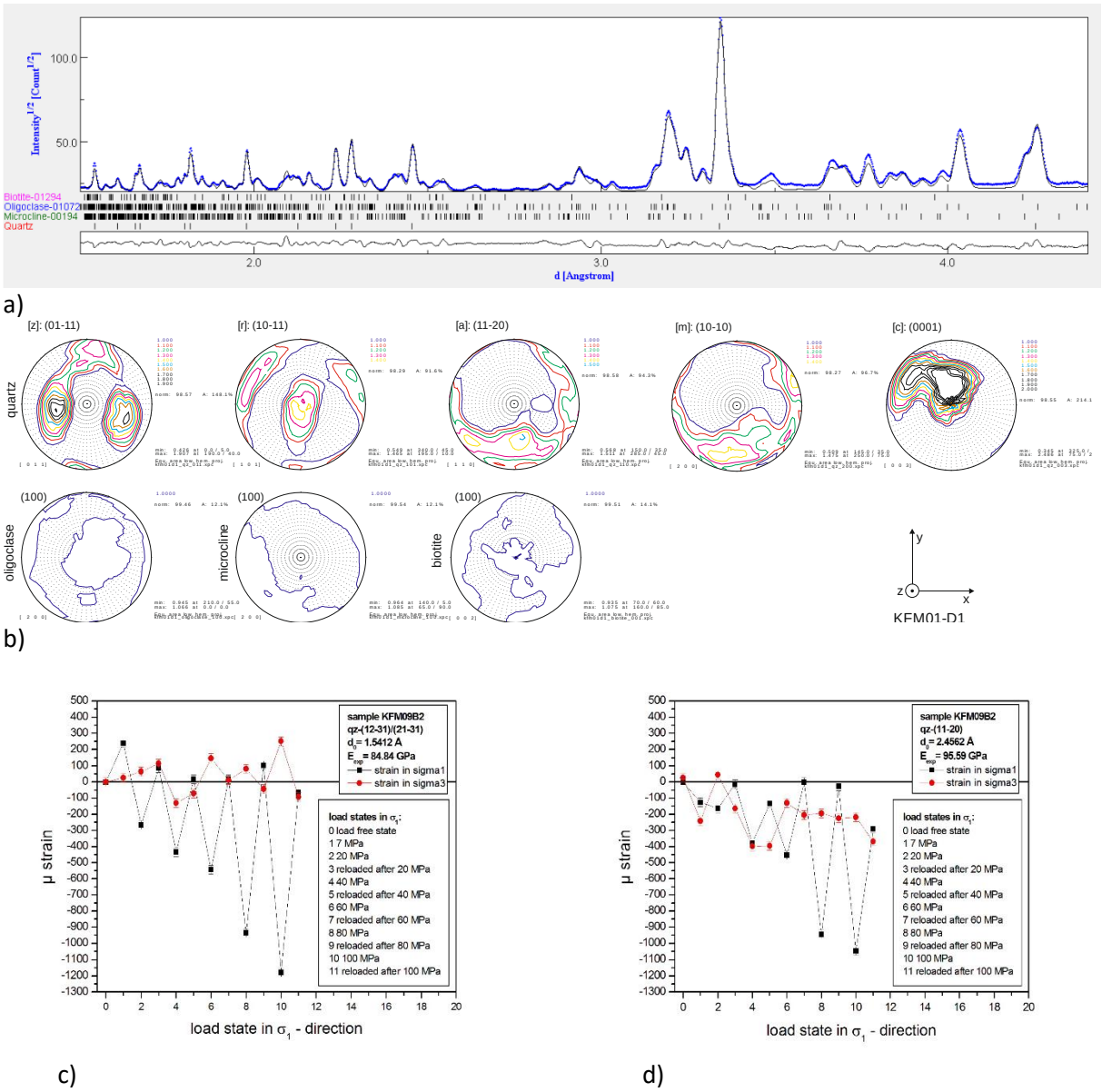

Fig. 31. Normalized TOF neutron diffraction spectra of granite sample obtained with the SKAT diffractometer. The Figure shows the experimental points (blue) and calculated profiles (black) as well as the positions of the diffraction peaks calculated by the MAUD program (a). Textures of quartz (top), oligoclase, microlin and biotite (bottom) (b). Applied and internal stresses of quartz (12-31) and (11-20) (c, d).

On the SKAT/EPSILON diffractometer *in situ* deformation experiments have been conducted with a granite sample from the Forsmark region (Sweden) containing quartz, plagioclase and biotite. A cylindrical sample (d = 30 mm, l = 60 m) was subjected to cyclic uniaxial loading in the range from 20 to 140 MPa. The measurements were conducted at 7 load levels, for each level the sample was reloaded. Applied and internal stresses were determined from the shift of the diffraction lines in the range of up to d = 5.1 Å. In addition, the acoustic emission measurements have been carried out, the combination of which with neutron experiments is needed for better understanding of reasons for the Kaiser effect. The quartz texture in the granite sample is well developed and characterized by one maximum in the pole figure [0001] near the z-axis and 120° pole density distribution of other lattice directions around the [0001] cluster (**Fig. 31**). This

gives grounds to suggest post-kinematic crystallization. In contrast, the texture of other phases is very weak (**Fig. 31**). The measured internal stresses were compared for the milled (< 62 μm) and annealed powder of the sample without stresses. During the internal stress measurements the cylindrical sample under study was rotated around the *z* axis with a step of 15° in the *xy* plane. The measured residual stresses were in the range from -1×10^{-3} to 1.2×10^{-3}.

The texture and microstructure of the pristine and retrogressed samples of eclogite and surrounding metasediments have been investigated to gain insights into the deformation processes in the palaeo-subduction channel of the Tauern region (Austria), **Fig. 32** [35]. The texture features and deformation processes in omphacite and glaucophane have been analyzed. The presence of a plastic deformation cycle in the metamorphism of eclogite and blueschist facies associated with the subduction and exhumation of rocks has been established.

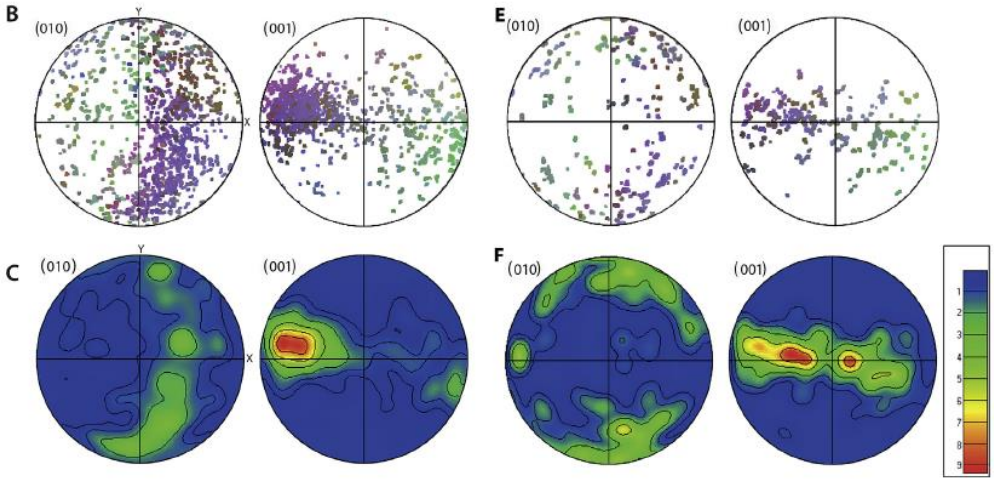

Fig. 32. Pole figures for eclogite rocks obtained with the SKAT diffractometer.

On the SKAT diffractometer the texture in a number of samples of high-strength vessel steels has been studied by thermal neutron diffraction (**Fig. 33**). The inhomogeneity of the texture across the thickness of a steel slab was investigated. Due to a large thickness (300 mm) of the slab the crystallization proceeds under various temperature conditions, therefore a strong morphological inhomogeneity can be observed across the thickness of the material. A set of 1368 (19×72) diffraction spectra was obtained from which complete direct pole figures (PF) with a grid size of 5˚×5˚ were derived. For each sample three pole figures (200) (110) (211) for α-Fe were obtained. It was revealed that the crystallographic structure changes only slightly across the thickness of the slab. From this it follows that the change in the morphological structure across the thickness of the high-strength steel slab is not related to a change in the crystallographic texture. In addition, the texture of rolled samples with different degrees of deformation has been studied as well. It has been found that the intensity of texture increases with the degree of rolling. Pole figures have been obtained for a low-temperature bainite phase with a bcc crystal lattice. The pole figure (110) for this phase corresponds to the pole figure (111) for the virtual high-temperature austenitic phase with an fcc lattice (typical texture of rolled copper). The high-temperature phase (austenite) is destroyed during quenching as a result of the phase transition. However, the revealed relationships between the pole figures of low-temperature (bainite) and high-temperature (austenite) phases provide an insight into the texture of the austenite destroyed during the phase transition.

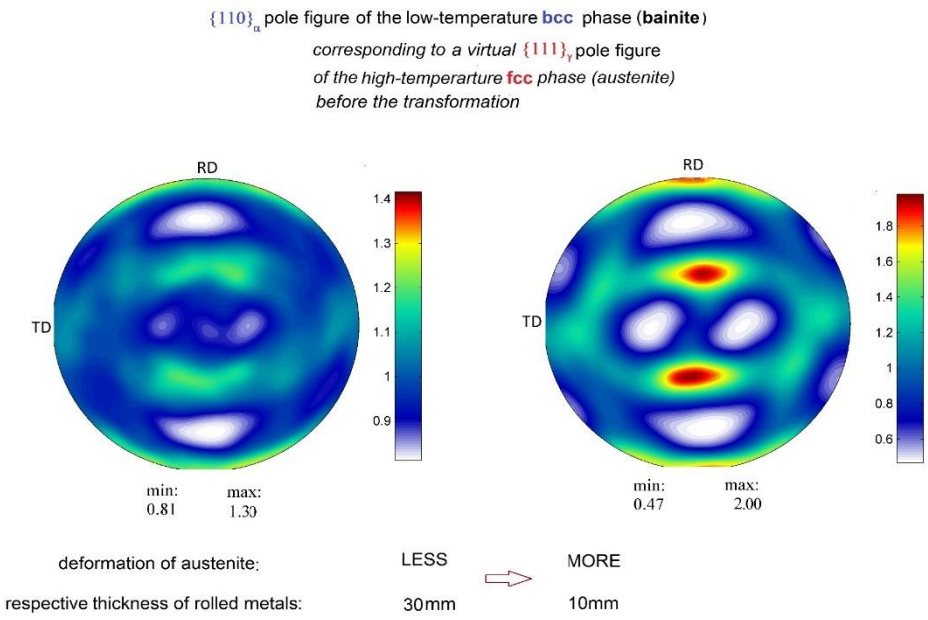

Fig. 33. Pole figures of low-temperature bainite phase with a bcc structure.

A new approach has been developed for a quantitative comparison of pole figures with the same crystallographic indexes, but measured for different samples. The approach is based on the consideration of the measured pole figures as specific implementations of a certain orientation distribution, i.e., as samples from a general ensemble of orientations. Thus, for the first time in the texture analysis a statistically valid measure for the quantitative comparison of pole figures has been introduced. This measure is the probability that the samples belong to the same orientation distribution and follows the statistics calculated within the Kolmogorov-Smirnov statistical test. The application of the introduced measure has been demonstrated on numerical examples for materials with cubic and hexagonal symmetry, as well as for real experimental data (pole figures of wheel steel). Also, using numerical examples, the peculiarities of the new approach have been demonstrated in comparison with the traditional calculation of the RP value when comparing pole figures [36].

The work has been done on the development of the methodology for evaluating the amount of residual austenite in high strength steels using the neutron diffraction method. The neutron diffraction spectra were measured on the texture instrument SKAT at FLNP JINR in order to eliminate the influence of the texture on the results. The measurements of calibration samples with the known austenite content were made. Using the results from the measurements of these samples, the calibration lines were obtained and applied to determine the fraction of residual austenite in the samples of medium-carbon steels (0.3 to 0.4%) with a tensile strength of 1500 MPa and 1700 MPa at different annealing temperatures (150 to 400ºC) following the hardening treatment [37].

On the EPSILON diffractometer, *in-situ* experiments to study the dependence of deformation on the load on a cylindrical sample of sandstone have been carried out (**Fig. 34**). A load of up to 56.33 MPa was applied during 9 stages to determine the Young's modulus for the crystallographic planes of quartz (01-11), (10-11), (11-20), (01-12)/(10-12). These results are consistent with the Hooke's law [38]. Instead of traditional fitting of diffraction data using the Rietveld method, an elastomechanical model has been developed to describe the stress-strain behavior, taking into account the changes in the pore space as a result of compaction of sediments associated with the change in the shape of quartz grains. This model was used to calculate the displacement of the diffraction peaks in the Voigt or Reuss approximations and their combinations. It has been established that the developed model can simulate with a high accuracy the diffraction

data under load using the data measured without load including both the displacement of peaks and their half-width changes [39].

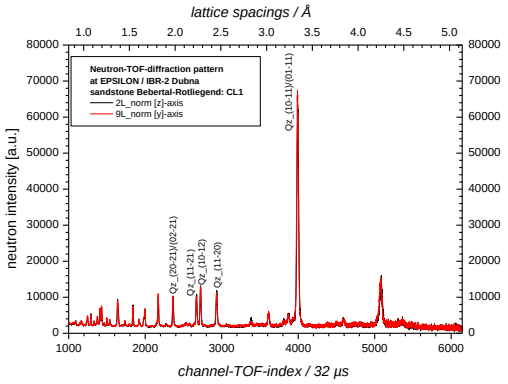

(a)

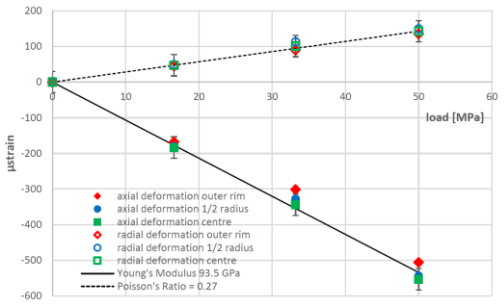

(b)

Fig. 34. Neutron diffraction spectra of sandstone measured on the EPSILON diffractometer (a). Dependence of microstresses on the load at various deformation types (b).

On the EPSILON diffractometer the experiments have been conducted to determine the magnitude and distribution of internal stresses caused by tensile embrittling destruction in the course of phased "Brazilian" creep tests for a pure marble sample (>95% $CaCO_3$). A comparison of internal stresses measured before and during phases of mechanical loading has been made. The obtained data are important for studying the mechanisms of rock destruction.

The internal stresses occurring as a result of elasto-plastic deformation and residual stresses after removing the mechanical load in metal-matrix composite alloys Al/SiC_p have been studied by neutron diffraction (EPSILON diffractometer) and synchrotron radiation techniques. The experimental results were compared with the elasto-plastic deformation model to determine the parameters responsible for the deformation of the Al matrix — critical allowable shear stress and hardening parameter. The analysis of data has shown that during the tensile test the Al matrix undergoes plastic deformation, and the SiC phase remains elastic. A self-consistent model allows one to correctly predict stresses in the SiC phase, but it overestimates the calculated values of the lattice strains in the Al matrix, which can be connected with the initial thermal stresses.

In collaboration with the Institute of archaeology, RAS, the internal organization of a series of objects of cultural heritage (antique coins, bracelets, crosses, etc.) has been studied at the facility of neutron radiography and tomography. As an example, **Fig. 35** illustrates the results of the study of an ancient bracelet, XIV century AD, from a recently discovered treasure in the city of Tver. A corrosion-coated part of the bracelet was investigated. Neutron tomography revealed the bracelet decor items made by gold-on-copper plating. The differences in the interaction of neutrons with gold and copper made it possible to reveal a decorative pattern on the bracelet hidden under corrosion.

Fig. 35. Photo of a fragment of the ancient bracelet from the treasure found in the city of Tver (left) and its 3D image reconstruction from neutron tomography data (right).

4. MAIN METHODOLOGICAL ACHIEVEMENTS

Work to develop the final configuration of the new DN-6 diffractometer was continued. In cooperation with the SC Department a second ring detector consisting of 96 independent helium counters has been manufactured. The first successful methodological and scientific experiments with a new two-detector system have been carried out (**Fig. 36**).

In 2015, the user program has started to be implemented on the GRAINS reflectometer. In accordance with the list of submitted proposals for the second half of 2015, more than ten experiments on electrochemical interfaces, magnetic colloidal systems, polymer solutions and melts, lipid solutions and others have been carried out at GRAINS. Among the interested organizations are the research centers of Russia (MSU, PNPI, NRC KI), Slovakia (IEP SAS), Ukraine (KNU), Hungary (WRCP HAS), Tajikistan (IC ASRT). In particular, the possibilities of neutron reflectometry experiments for electrochemical interfaces under potential have been considered in the framework of comprehensive studies combining various complementary methods of synchrotron radiation and thermal neutrons [40]. The main emphasis was placed on the optimization of experimental conditions (substrate, electrode, solvent) to detect the formation of a transitional layer (so-called solid electrolyte interphase, SEI) on the model electrode and to obtain its characteristics (thickness and density) depending on the applied potential. To eliminate the influence of uncontrolled oxidation of metal electrodes on the results of experiments, the regulated oxidation of titanium and nickel films deposited on a glass substrate has been investidated (**Fig. 37**). The study has been carried out in collaboration with the Department of Chemistry of Moscow State University (Moscow, Russia), Petersburg Nuclear Physics Institute, NRC "Kurchatov Institute" (Gatchina, Russia) and the Faculty of Physics of the Taras Shevchenko National University of Kiev (Kiev, Ukraine).

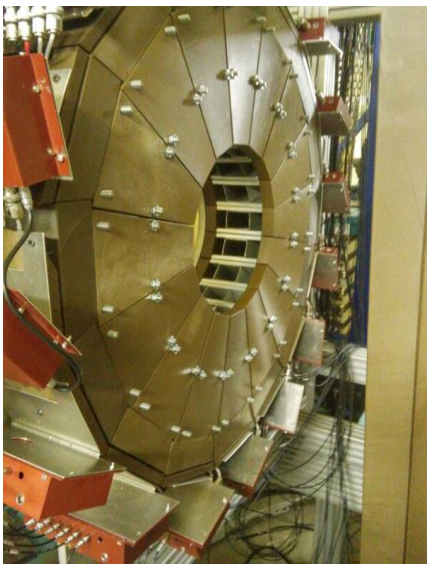

a)

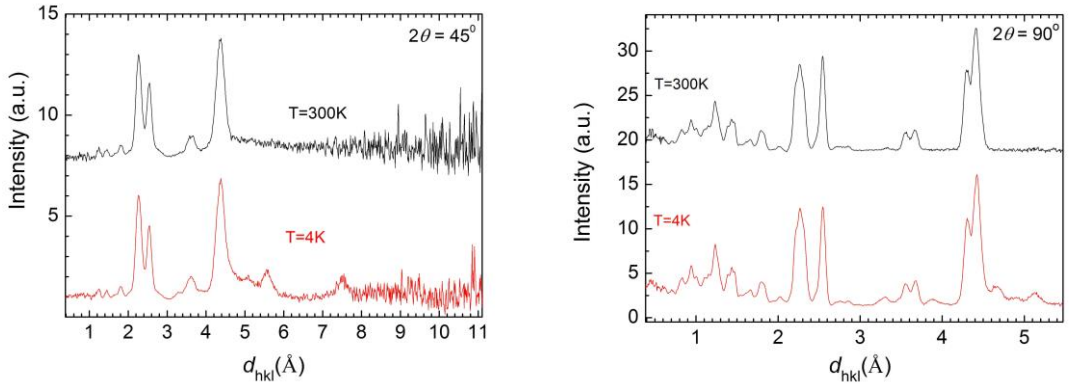

(b) (c)

Fig. 36. New neutron ring detector at the DN-6 diffractometer (a). Diffraction spectra of $LiMn_2TeO_6$ obtained at scattering angles 2θ = 45° (b) and 90° (c). Exposition time – 10 min.

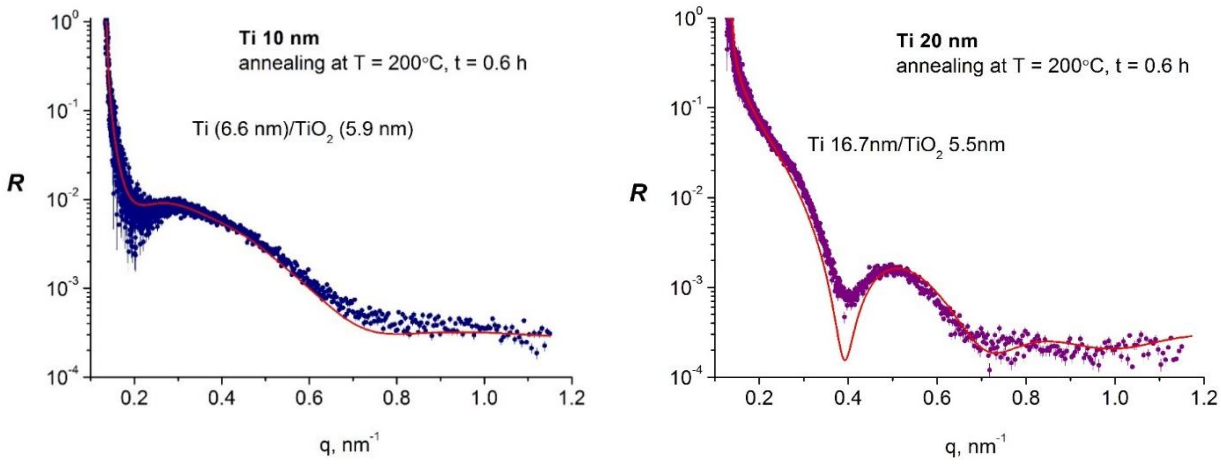

Fig. 37. Experimental reflectivity curves (GRAINS, IBR-2) for model metal (Ti) films of different thicknesses on a glass substrate oxidized using a special procedure (PNPI, NRC KI). The solid lines show the simulation results with the indication of the obtained thicknesses for the film and the oxide layer.

In 2016, special cells for *in-operando* reflectometry experiments with electrochemical interfaces and a thermostatic cell with a temperature of up to 150°C were designed and successfully tested on the GRAINS instrument (**Fig. 38**). An automatic mobile platform for the polarizer has been successfully put into operation at the GRAINS instrument for experiments with polarized neutrons.

(*a*)

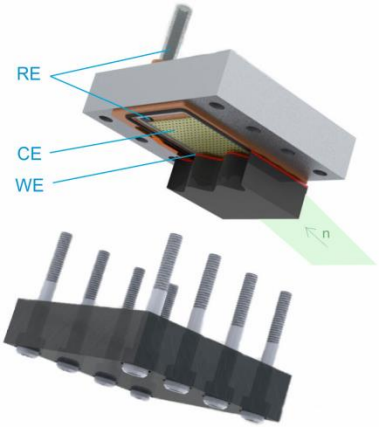

Fig. 38. Special three-electrode electrochemical cell (a) and thermostatic (up to 150°C) cell (b) for neutron reflectometry; automatic mobile platform with polarizer (c).

(*b*)

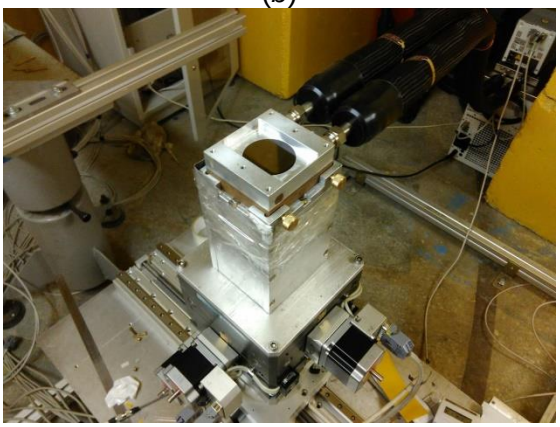

(*c*)

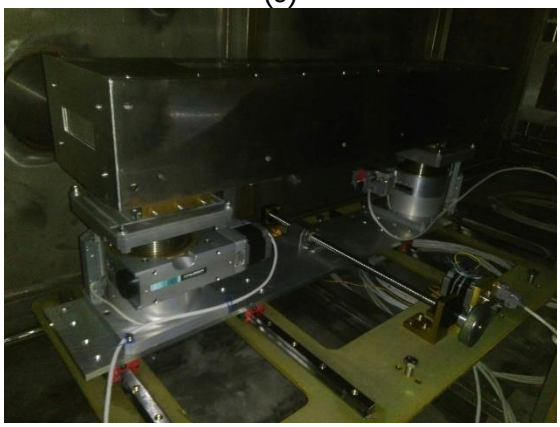

The realization of the project aimed at creating a basic configuration of the diffractometer on beamline 6a for neutron diffraction studies of transition processes in real time (RTD diffractometer - Real Time Diffractometer) has been completed [41]. The diffractometer (**Fig. 39**) is designed to study irreversible transition processes with characteristic times ranging from fractions of a second to tens of minutes. In favorable cases, the time resolution of RTD will be fractions of a millisecond. The developed detector system (small-angle detector, detectors at medium scattering angles of 30° - 90° and a detector at large scattering angles in combination with the available wavelength range of 0.5-20 Å) makes it possible to obtain diffraction spectra over a wide range of interplanar spacings (d_{min}, d_{max}) = (0.5 - 300) Å. A triaxial goniometer and two-coordinate PSD with an active area of 225x225 mm and spatial resolution of 2x2 mm are used for investigations with single crystals and multilayer structures.

A new mirror neutron guide (designed and manufactured by SwissNeutronics, Switzerland) has been installed on the HRFD diffractometer. New mirror sections have been mounted in the available vacuum housing with the entrance (behind Fourier chopper) and exit (in front of sample position) points remaining unchanged (total length of 18.8 m), **Fig. 40**. The neutron guide has been designed to be plane-parallel in the horizontal plane (window width 15 mm) and have a parabolic convergence in the vertical plane (heights of the entrance and exit windows are 200 mm and 100 mm, respectively). The Ni/Ti supermirror glass coating has a critical index m = 1.75.

In addition, on HRFD, the operation of a new Fourier chopper (**Fig. 40**) installed in August of 2016 to replace the old chopper has been started. The Fourier chopper has been mounted on a

movable platform to move/remove the chopper into/from the beam. This option is required in *in-situ* experiments performed on the HRFD diffractometer and provides an additional double increase in the flux for the high intensity mode.

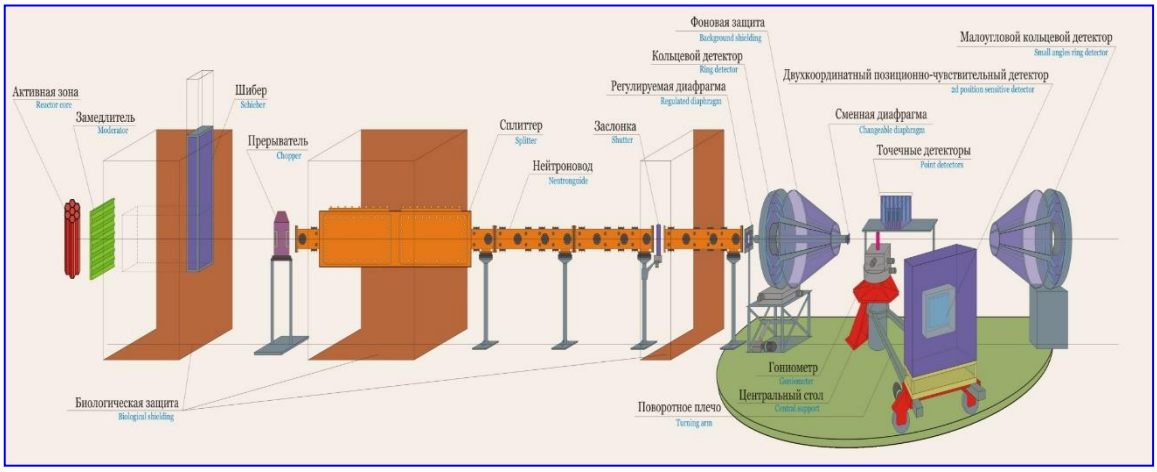

Fig. 39. Basic components of the RTD refractometer at the IBR-2 reactor. Shown from left to right are: reactor core and moderator, biological shielding, chopper to reduce the background between the reactor pulses, "splitter" to split the neutron beam into two beams, mirror neutron guide with a shutter to shut the beam, adjustable diaphragm at the exit of the neutron guide, central platform with a sample position and detectors. Four detector units are used: 2D PSD on a rotating platform, two ring detectors at small and large scattering angles and a battery of ^{3}He-counters near $2\theta = 90°$.

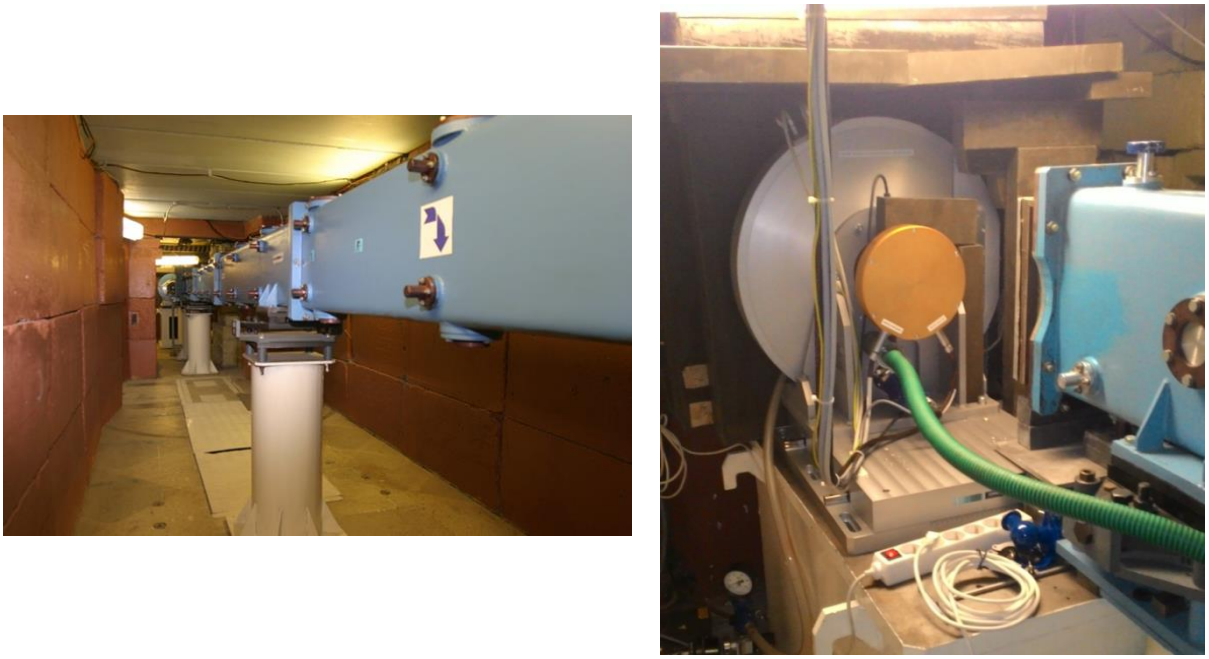

Fig. 40. New mirror neutron guide with vertical parabolic convergence (at left) and new Fourier chopper (at right) in the working position at the HRFD diffractometer.

The qualitative comparison of the effective scattering spectra from vanadium for the old and new neutron guides has shown that the overall spectrum shape has changed insignificantly, but a considerable shift towards shorter wavelengths by ≈0.6 Å has occurred (**Fig. 41**). The gain factor for the neutron flux was determined from the ratio of the intensities of the diffraction peaks from a standard sample of Al_2O_3 (**Fig. 41**). It can be seen that in the wavelength range from 2 to

7 Å its value varies from 2.2 to 2.7. At lower wavelengths, the new neutron guide gives even greater increase in the flux.

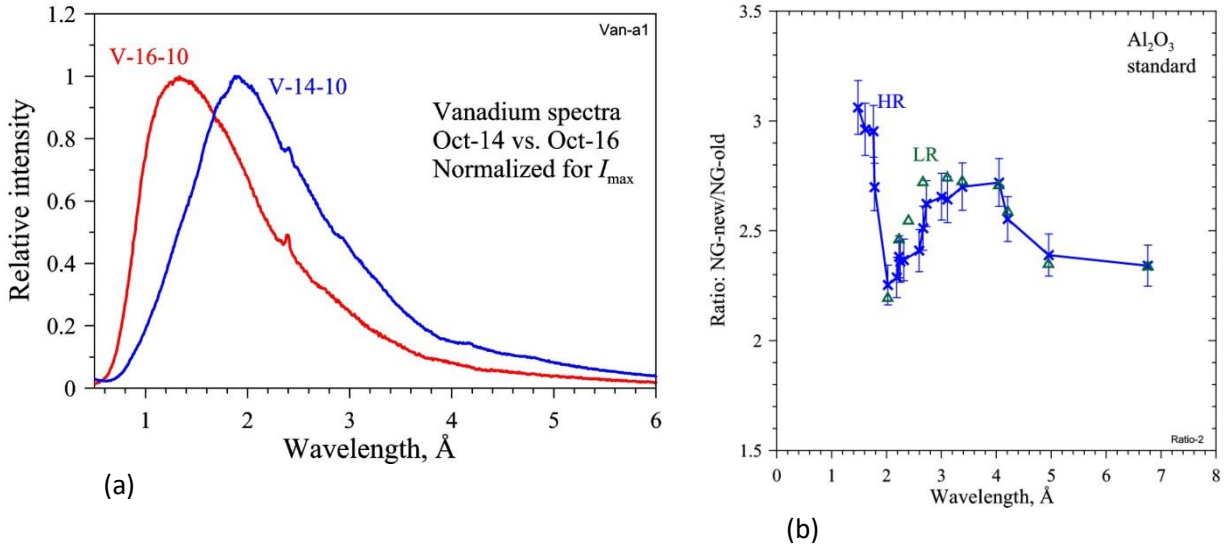

Fig. 41. Qualitative comparison of effective spectra for old (V-14-10) and new (V-16-10) neutron guides using scattering from vanadium (a). Gain factor for the flux for the new neutron guide determined by comparing intensities of diffraction peaks from a standard Al_2O_3 sample as a function of wavelength (b). Points measured from spectra of high (HR) and low (LR) resolution, i.e. using correlation analysis and without it, respectively.

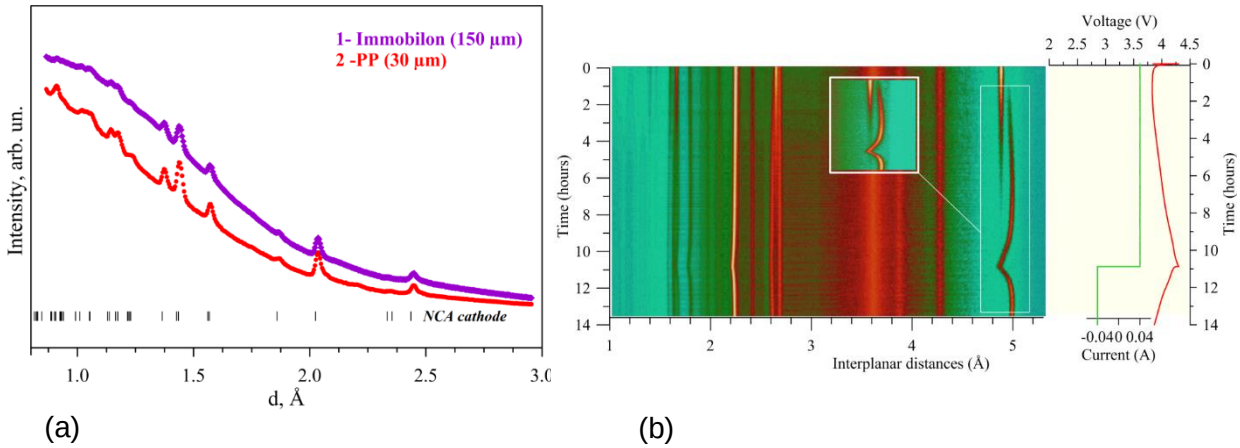

Fig. 42. Comparison of neutron scattering from electrochemical cells with PVDF Immobilon and usual polypropylene separators (a). Immobilon (despite partial replacement of hydrogen with fluorine) is worse than normal separator because of a larger amount of absorbed electrolyte and resulting incoherent scattering. The evolution of the diffraction spectra obtained with the electrochemical cell with conventional electrolyte and separator during the first "forming" cycle (b). As a cathode, Li(Ni,Co,Al)O2 was used, as an anode – lithium-7 isotope. The marked region of diffraction peak 003 from the cathode clearly illustrates the cathode activation process over the entire electrode volume: intensity of gradually disappearing peak (top down) is directly proportional to the amount of inactive cathode material. After cell (battery) charging the entire volume of the cathode material is electrochemically active.

A series of *in-situ* and *in-operando* neutron diffraction experiments using specially designed electrochemical cells have been carried out to determine optimal (from the viewpoint of neutron scattering) auxiliary materials for model current sources. Basic requirements to the materials are minimum incoherent scattering, minimum neutron absorption, ease of use in the

assembly of the cell, in-store availability. An optimal separator, electrolyte and anode material have been selected (**Fig. 42**). The paper on the results of the work is under preparation. The demand for this work is testified by an increasing number of applications for experiments at the RTD and HRFD instruments with the use of the developed electrochemical cells.

(а) (б)

Fig. 43. FSD Fourier diffractometer on IBR-2 beamline 11: a) sample position on the HUBER goniometer; b) testing machine LM-20 with a steel sample.

(a) (b)

Fig. 44. New wide-aperture radial collimators for the FSD Fourier diffractometer, beamline 11A of the IBR-2 reactor (a). Bulk sample under study on the HUBER goniometer at FSD. Small scattering volume (gauge volume) within a sample is cut by the radial collimators mounted on special adjusting frames (b).

At FSD a uniaxial mechanical testing machine LM-20 has been installed, which significantly expands the range of possible experiments with the diffractometer. This device is intended to study samples at an external uniaxial load directly in the neutron beam. In 2015, several test neutron diffraction experiments with the application of tensile and compressive loads on

austenitic and ferritic steel samples were successfully performed at FSD (**Fig. 43**). In the autumn of 2015 first experiments with a testing machine LM-20 began to be performed on the request of external users. In future, this device is planned to be used at FSD on a regular basis.

Two new wide-aperture radial collimators (by JJ X-Ray, Denmark) have been installed at the FSD diffractometer, **Fig. 44**. To position the collimatiors, special tables that allow one to adjust the collimators in the scattered beam and to move/remove them into/from the beam if necessary, have been designed.

The new radial collimators cover the entire angle range of ±20° in the scattering plane, thus allowing the use of all available elements of ASTRA detectors, which makes it possible to significantly increase the luminosity of experiments and perform measurements with thick samples.

On FSD, work to improve algorithms on obtaining diffraction spectra from "raw" data has been continued. In the list mode, a program has been developed to filter detection events and provide the same method of pulse duration discrimination as that implemented in the electronics of the ASTRA detectors at FSD. In addition, two new experimental operation modes of the Fourier chopper at FSD (Dirichlet and Blackman frequency windows) have been introduced, which will allow one to explore different dynamic aspects in the operation of the Fourier chopper and improve its control system.

On IBR-2 beamline 13 the work on the development of a Fourier diffractometer FSS is in progress in cooperation with the SC Department (**Fig. 45**). In 2015, operational control boxes of a shutter and beam stopper, light alarm system, power supply and control system of the Fourier chopper were installed, an experimenter's control cabin was mounted, and a mirror neutron guide in the steel casing was assembled with the participation of specialists from PNPI. In November 2015, at FSS the first trial opening of the beam was held, during which radiation conditions on the beamline were evaluated, neutron beam profiles were obtained and first diffraction spectra were collected.

In 2016, the components of the Ost and West detectors were delivered to the beamline. Modules of a Huber goniometer were mounted and adapted to the table of FSS. A Fourier-chopper was installed on a platform and underwent idle testing. Crates with the detector and acquisition electronics were put in place (**Fig. 45**). The state of the mirror coating in a section of the FSS neutron guide was studied with the GRAINS reflectometer, which revealed a significant damage of the mirror coating and the necessety to replace the sections of the neutron guide in the immediate future. The calculations of the new geometry for the Ost detector, as well as the detector assembly and connection were performed. First test measurements with the Ost detector in the TOF-mode have been carried out and demonstrated the performance capability of all detector elements and the need for its further adjustment (selection of operating voltage, detection thresholds, etc.).

A spin neutron interferometer of a new type based on the splitting of neutron waves reflected from a magnetic mirror has been studied. In the setup an initially unpolarized neutron beam passes through a system of two mirrors placed in a perpendicular magnetic field. A precession of the neutron magnetic moment as a periodic wavelength dependence for the intensity of neutrons passing through the system of two magnetic mirrors has been observed (**Fig. 46**). With increasing magnetic field up to 200 Oe the precession of the neutron beam polarization decays because of magnetic field inhomogeneities. The interferometer can be a part of a spin-echo spectrometer where the influence of magnetic field inhomogeneities and neutron beam divergence are eliminated. In particular, it can be used to study a static inhomogeneous state with a micron-size correlation length and the dynamics of media with correlation times at a microsecond level, as well as to measure the width of neutron wave packets.

Fig. 45. Fourier-diffractometer FSS on IBR-2 beamline 13 (from top to bottom and from left to right): operational control boxes of a shutter and beam stopper; entrance door to the bunker (beam exit location); glass mirror neutron guide sections before installation in a housing; neutron guide installed in a steel housing and control electronics of the Fourier chopper; experimenter's control cabin mounted on the biological shielding of beamlines № 13-14; detector Ost (without shielding) after installation and alignment of 12 PMTs with glued ^{6}Li glasses; at the sample position, modules of the HUBER goniometer are installed and adapted to the FSS table; TOF spectra from standard α-Fe sample measured by each of 12 PMTs of the 90^{o}-detector Ost at FSS.

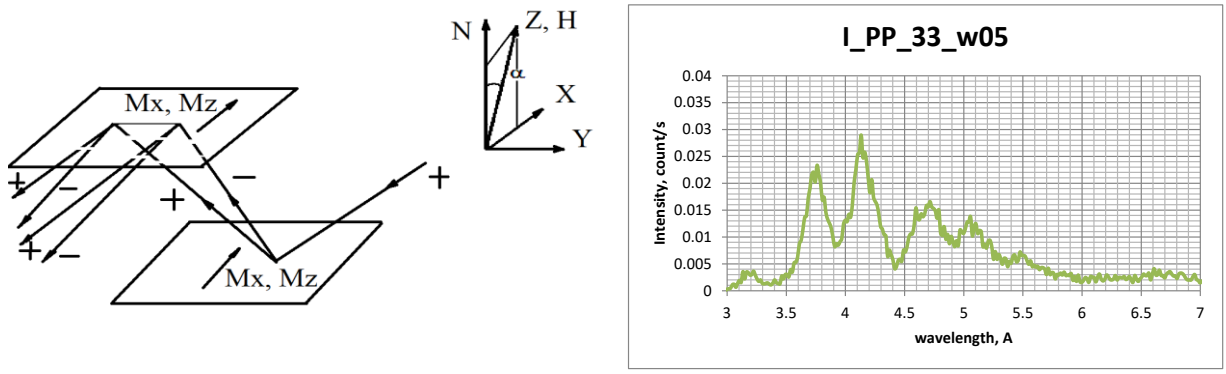

Fig. 46. Operating principle of the neutron spin interferometer of a new type (left) and spectrum of neutrons passing through the interferometer under a magnetic field of 33 Oe (right).

A method to study weakly magnetic films using the polarized neutron channeling has been developed (**Fig. 47**). The magnetic induction of a weakly magnetic layer has been measured. The structure Ta(3 nm) / $Ni_{0.67}Cu_{0.33}$(15 nm) / $TbCo_5$(150 nm) / $Ni_{0.67}Cu_{0.33}$(50 nm) / Si(substrate), in which the waveguide layer is made of a material ($TbCo_5$) with small saturation magnetization of about 200 G has been investigated. Such materials containing rare earth elements are widely used for the development of new methods for magnetic recording. However, because of the weak saturation magnetization these materials cannot be studied by standard reflectometry of polarized neutrons, which is used for materials with magnetization of more than 1000 G. In experiments, a polarized neutron beam falls at some grazing angle on a three-layer waveguide structure where the resonance amplification of the neutron wave in the average weakly magnetic layer occurs. The neutron wave phase in the resonance depends on the neutron spin direction, channel width and magnetic induction in a channel. Along with it, the grazing angles of the incident beam for spins (+) and (-) differ, and the difference in the squared sines of these angles directly gives the magnetic induction in the layer at its values of less than 100 mT. With increasing B, other factors start to determine the non-linear dependence. The prospects of this method for neutron measurements in research of weakly magnetic materials have been concluded to be good.

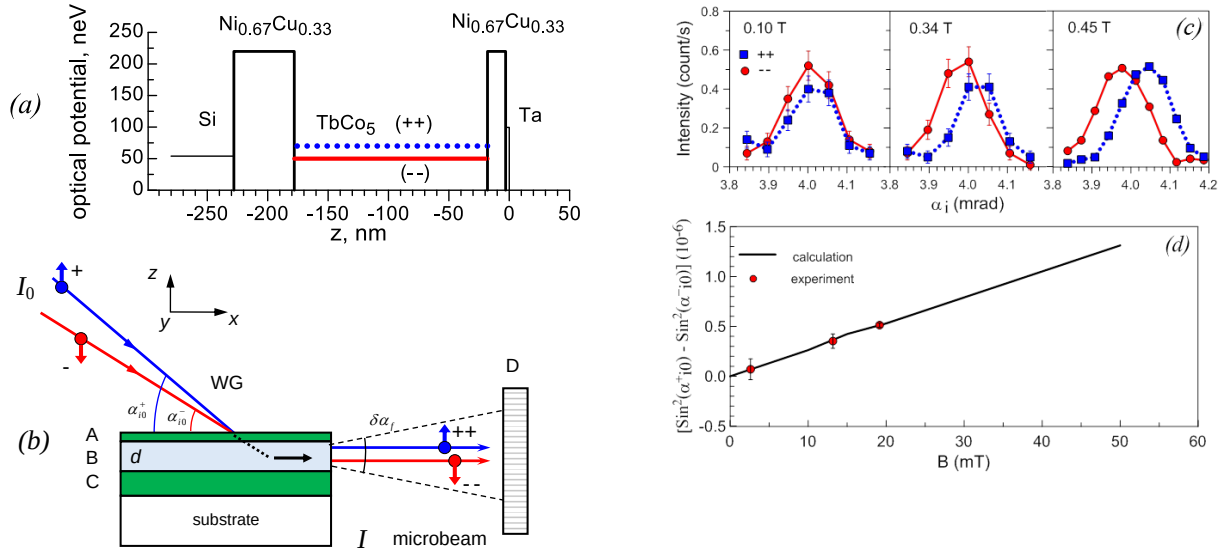

Fig. 47. Optical potential profile for the nanostructure Ta(3 nm) / $Ni_{0.67}Cu_{0.33}$(15nm) / $TbCo_5$(150nm) / $Ni_{0.67}Cu_{0.33}$(50nm) / Si(substrate) (a), scheme of the experiment (b) parts of the spectrum of scattered neutrons at different magnetic fields (c) and difference of squared sines of grazing angles as a function of magnetic field induction (d).

On the REMUR reflectometer, a spectral width of the microbeam emitted from the end of a flat waveguide has been investigated as a function of the angular divergence of the incident beam, **Fig. 48** [42]. It has been shown that the spectral width of the microbeam decreases with diminishing angular divergence of the incident beam. By extrapolating the linear dependence in the zero divergence point of the initial beam and subtracting the reactor pulse duration, the spectral width of the resonance has been experimentally evaluated. The agreement of this value with the theoretical estimate testifies that the description of the resonance properties of the waveguide system is correct. The knowledge of the spectral width of the microbeam makes it possible to evaluate the wavelength resolution limit by probe microscopy. This method uses the Larmor precession of the spin of neutrons in the microbeam passing through the sample and scanning it with a high spatial resolution.

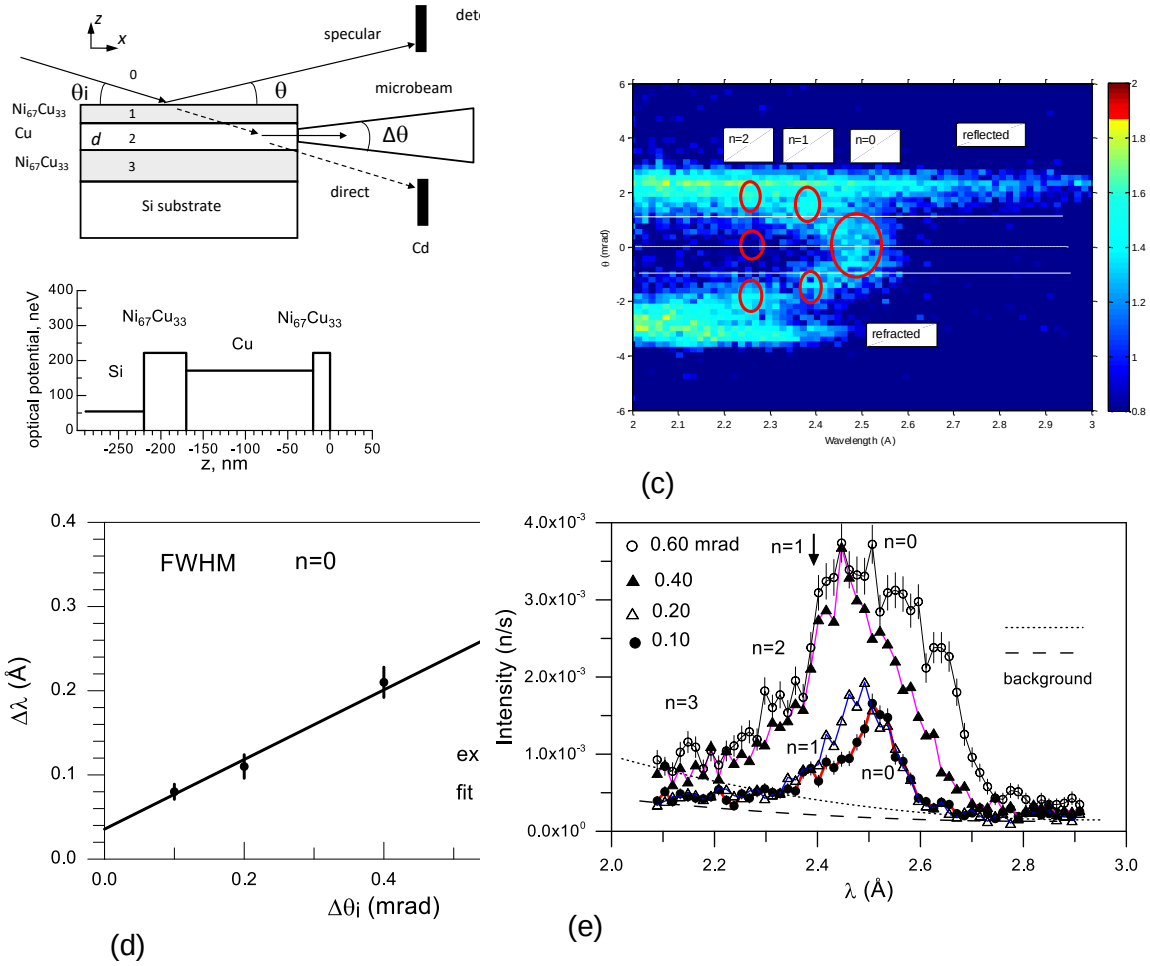

Fig. 48. Scheme of experiment (a). Neutron optical potential of sample depending on *z*-coordinate perpendicular to sample layers (b). 2D-dimensional neutron counting map depending on wavelength and scattering angle at fixed grazing angle of incident beam of 3.69 mrad. Ellipses show the maxima of transmitted microbeams for resonances of orders n = 0, 1, 2 (one, two and three maxima over scattering angle, respectively) (c). Microbeam wavelength resolution for resonance order n = 0 and its dependence on angular divergence of incident beam (points - experiment, vertical dashes - experimental errors). Solid line shows linear fit (d). Integral microbeam intensity around sample horizon depending on neutron wavelength at different angular divergence of incident beam: 0.60, 0.40, 0.20 and 0.10 mrad. Marked peaks correspond to resonance orders n = 0, 1, 2, 3 (e).

The REFLEX reflectometer has been reconstructed into a small-angle spin-echo spectrometer (SESANS) with linearly increasing magnetic fields. On beamline 9, a new mirror neutron guide has been installed and a beam shutter has been placed in a new position closer to the moderator. As a result, the incident neutron flux at the sample has increased to 10^6 n / cm^2 / c, which is 100 times better than the old value (**Fig. 49**). The work was carried out with the financial support in the framework of the BMBF-JINR agreement.

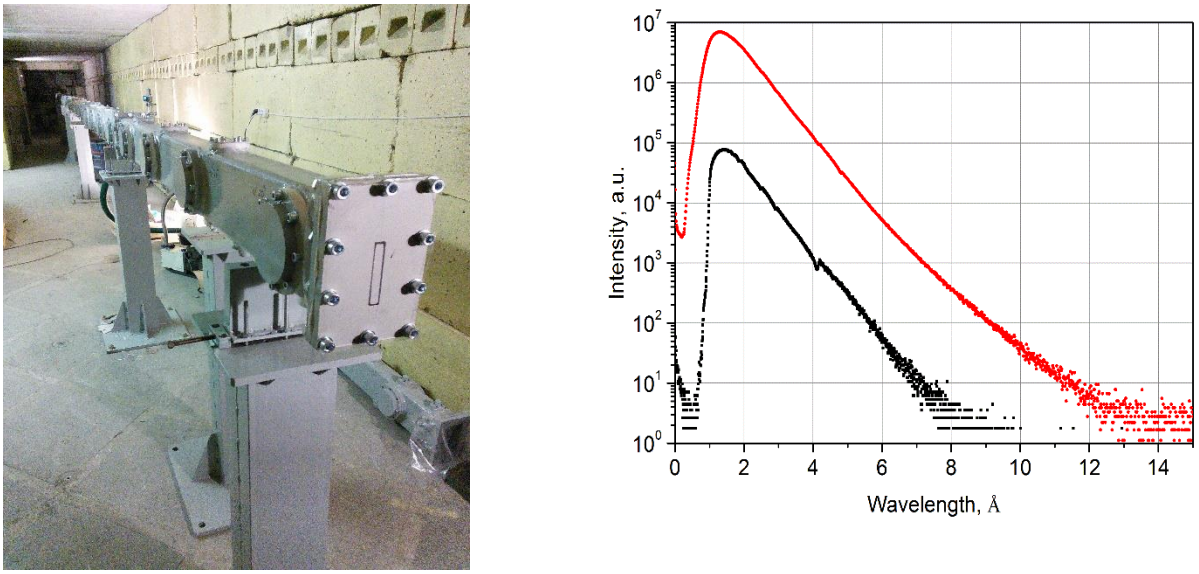

Fig. 49. New mirror neutron guide of the small-angle scattering spin-echo spectrometer on beamline 9 of IBR-2 (at left). Spectral distribution of the incident neutron flux density at the sample position with the new neutron guide (red symbols) and in the old configuration (black symbols), at right.

In addition, the study of the operating modes of the SESANS spectrometer with linearly increasing magnetic fields which is under construction at beamline 9 of IBR-2, has been continued using Monte Carlo simulations (VITESS software package) with the parameters: distance between spin rotators in each arm – 60 cm, thickness of spin rotators a = 2 cm, period of sawtooth pulses T = 1 ms, pulse amplitude B = 500 Oe, inclination of spin rotators relative to the instrument axis $\alpha = 60°$. The TOF spectrum had the wavelength range of 1-15 Å, and the polarization of the beam before entering the first arm of the setup was directed along the Z-axis and was 100% in the entire wavelength range. The scattering object was a set of homogeneous monodisperse spheres. To determine the working intervals in the spectrum $\Delta\lambda$ meeting the necessary criteria, the simulation of the polarization as a function of neutron wavelength $P_z(\lambda)$ was carried out in the absence of the sample. The working plateaus with the length $\Delta\lambda$ covering about 10 time-of-flight channels with 64 ms width are narrow but sufficient for measurements. To simulate the scattering curves, neutrons with wavelengths from the plateaus were used. Neutrons from different working intervals form different scattering curves corresponding to different operation modes of the instrument *n* (**Fig. 50**). The results of the simulation of the SESANS experiment in the VITESS package fully coincide with the analytical calculations, which confirms the correctness of the virtual instrument.

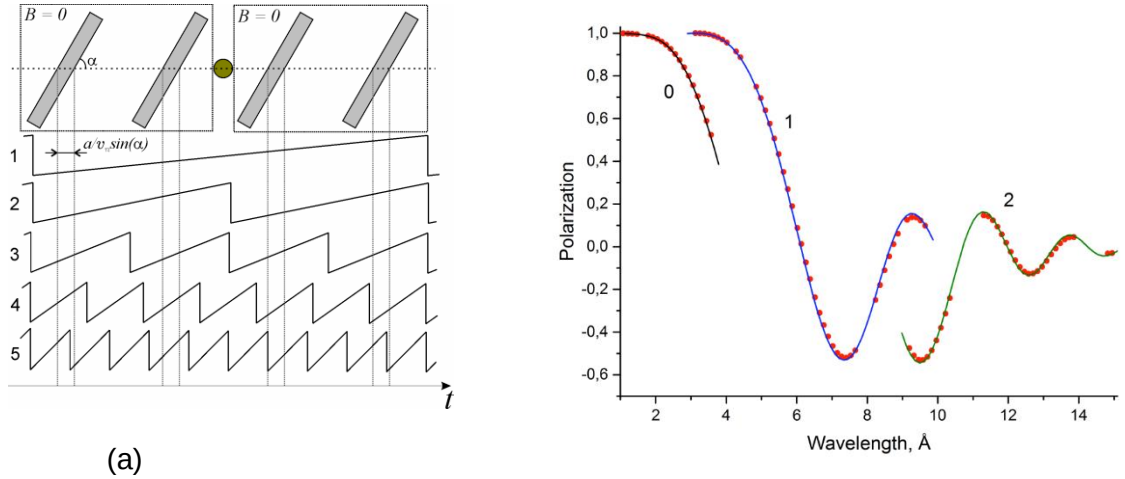

(a) (b)

Fig. 50. Time diagram for neutrons of different velocities: one sawtooth field pulse covers neutron time of flight through all four spin rotators (1); only two spin rotators (2); only one spin rotator (3); only one spin rotator and few pulses for time of flight between rotators (4); neutron hits a jump in magnetic field as it passes through at least one spin rotator (a). SESANS signal obtained for scattering from spheres with radius of 100 Å. Scattering curves clearly show formation of three different dependences corresponding to different modes of setup operation. Solid lines – analytical calculations (b).

The obtained result means that the obtaining of data on the object under study in the considered method is related to the necessity to separately consider different parts of the scattering curves obtained in one measurement. Further technical development of the technique based on the possibility of the broadening of the field pulses under a constant time gradient can reduce the number of modes to two or even one. It is clear that this development will require more powerful power supplies and perfect cooling systems for the coils of spin rotators.

On the neutron radiography and tomography spectrometer simulation energy-selective radiography experiments have been conducted [43]. In the experiments a CCD-camera-based detector was used. The frequency of the camera was synchronized with the reactor pulse frequency. Using the camera response delay relative to the start of reactor pulses and the exposure time variation, neutron images of various metal materials (aluminum, steel, lead, copper) have been obtained in the neutron wavelength ranges of 0.2-2, 2-3.7, 3.8-8 Å. A change was observed in the contrast of images of the materials in the ranges under study (**Fig. 51**), which offers good prospects for further development of energy-selective radiography and tomography at the IBR-2 reactor.

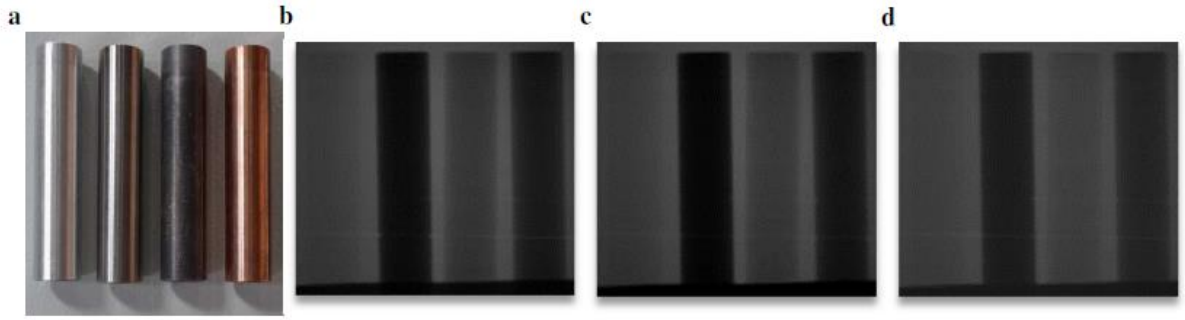

Fig. 51. Photo of cylindrical samples (aluminum, steel, lead, copper) (a) and their neutron images obtained in the wavelength ranges of 0.2-2 Å (b), 2-3.7 Å (c), 3.8-8 Å (d).

5. Financing

Planned budget

	2015 kUSD	2016 kUSD	2017 kUSD
Materials	421.6	450	531.2
Equipment	632.4	675	796.8
Research under contracts	20.0	20.0	20.0
ISTC	158.7	158.7	158.7
Total	1232.7	1303.7	1506.7

Additional sources of financing – 900 kUSD per year, including:
BMBF - JINR Agreement,
South Africa - JINR Agreement,
AER - JINR Agreement,
RSF Grants,
RFBR Grants,
IAEA Grants.

References

1. S.V.Ovsyannikov, M.Bykov, E.Bykova, D.P.Kozlenko, A.A.Tsirlin, A.E.Karkin, V.V.Shchennikov, S.E.Kichanov, H.Gou, A.M. Abakumov, R.Egoavil, J.Verbeeck, C.McCammon, V.Dyadkin, D.Chernyshov, S. van Smaalen, and L.S. Dubrovinsky "Charge ordering transition in iron oxide Fe_4O_5, involving competing dimer and trimer formation", Nature Chemistry, v. 8, p. 501 (2016).
2. D.P.Kozlenko, N.T.Dang, S.E.Kichanov, E.V.Lukin, A.M.Pashayev, S.G.Jabarov, L.S.Dubrovinsky, H.-P.Liermann, W.Morgenroth, A.I.Mammadov, R.Z.Mekhtieva, V.G.Smotrakov, and B.N.Savenko "Competing magnetic states in multiferroic YMn_2O_5 at high pressure", Physical Review B, v. 92, p. 134409 (1-7) (2015).
3. D.P. Kozlenko, N.T. Dang, T.L. Phan, S.E. Kichanov, N.V. Dang, T.D. Thanh, L.H. Khiem, S.H. Jabarov, T.A. Tran, T.V.Manh, A.T.Le, B.N. Savenko "The Structural, Magnetic and Vibrational Properties of Ti-doped $BaMnO_3$" Journal of Alloys and Compounds, accepted (2016).
4. N.V. Kosova, I.A. Bobrikov, O.A. Podgornova, A.M. Balagurov, A.K. Gutakovskii Perculiarities of structure, morphology, and electrochemistry of the doped 5-V spinel cathode materials $LiNi_{0.5-x}Mn_{1.5-y}M_{x+y}O_4$ (M=Co, Cr, Ti; x+y = 0.05) prepared by mechanochemical way. Journal of Solid State Electrochemistry 20, 235 (2016).
5. A.M.Balagurov, I.A.Bobrikov, S.V.Sumnikov, V.Yu.Yushankhai, N.Mironova-Ulmane, Magnetostructural phase transitions in NiO and MnO: Neutron diffraction data, JETP Lett. 104 (2016) 88 - 93.
6. S.Ya. Istomin, V.V. Chernova, E.V. Antipov, M.V. Lobanov, I.A. Bobrikov, V.Yu. Yushankhai, A.M. Balagurov, K.Y. Hsu, J.-Y. Lin, J.M. Chen, J.F. Lee, O.S. Volkova, A.N. Vasiliev "Wide range tuning of Mo oxidation state in $La_{1-x}Sr_xFe_{2/3}Mo_{1/3}O_3$ perovskites" European Journal of Inorganic Chemistry, v. 2016 (18), pp. 2942-2951 (2016).
7. A.I.Gusev, A.S.Kurlov, I.A.Bobrikov, A.M.Balagurov "$V_8C_{7-\delta}$ Superstructure in Nonstoichiometric Vanadium Carbide Powders" JETP Letters, 2015, Vol. 102, No. 3, pp. 154–160.
8. A.M.Balagurov, I.A.Bobrikov, B.Mukhametuly, S.V.Sumnikov, I.S.Golovin, Coherent

cluster atomic ordering in the Fe-27Al intermetallic compound, JETP Lett. 104 (2016) 539–545.

9. N.M.Belozerova, S.E.Kichanov, Z.Jírak, D.P.Kozlenko, M.Kačenka, O. Kaman, E.V.Lukin, B.N.Savenko “High pressure effects on the crystal and magnetic structure of nanostructured manganites $La_{0.63}Sr_{0.37}MnO_3$ and $La_{0.72}Sr_{0.28}MnO_3$”, Journal of Alloys and Compounds, v. 646, pp. 998-1003 (2015).
10. M.V.Avdeev, Petrenko V.I., Gapon I.V., Bulavin L.A., Vorobiev A.A., Soltwedel O., Balasoiu M., Vekas L., Zavisova V., Kopcansky P. “Comparative structure analysis of magnetic fluids at interface with silicon by neutron reflectometry”, Appl. Surf. Sci., v. 352, pp. 49–53 (2015).
11. M.Kubovcikova, I.V.Gapon, V.Zavisova, M.Koneracka, V.I.Petrenko, O.Soltwedel, L.Almasy, M.V.Avdeev, P.Kopcansky. On the adsorption properties of magnetic fluids: impact of bulk structure. JMMM 427 (2017) 67–70.
12. M.Rajnak, Petrenko V.I., Avdeev M.V., Ivankov O.I., Feoktystov A., Dolnik B., Kurimsky J., Kopcansky P., Timko M. “Direct observation of electric field induced pattern formation and particle aggregation in ferrofluids”, Applied Physics Letters, v. 107, p. 073108 (2015).
13. A.V.Nagornyi, Petrenko V.I., Avdeev M.V., Yelenich O.V., Solopan S.O., Belous A.G., Gruzinov A.Yu., Ivankov O.I., Bulavin L.A. Structural aspects of magnetic fluid stabilization in aqueous agarose solutions. JMMM 431 (2017) 16 - 19.
14. J.Majorosova, V.I.Petrenko, Siposova K., Timko M., Tomasovicova N., Garamus V.M., Koralewski M., Avdeev M.V., Leszczynski B., Jurga S., Gazova Z., Hayryan Sh.,Hu Chin-Kun, Kopcansky P. On the adsorption of magnetite nanoparticles on lysozyme amyloid fibrils. Coll. Surf. B, 2016, V. 146, pp. 794–800.
15. V.Gdovinova, Tomasovicova N., Batko I., Batkova M., Balejcikova L., Garamus V.M., Petrenko V.I., Avdeev M.V., Kopcansky P. Interaction of magnetic nanoparticles with lysozyme amyloid fibrils. JMMM 431 (2017) 8 - 11.
16. Petrenko V.I., Avdeev M.V., Bulavin L.A., Almasy L., Grigoryeva N.A., Aksenov V.L. Effect of surfactants excess on the stability of low-polarity ferrofluids probed by small-angle neutron scattering. Crystallography reports, 2016, V. 61, Issue 1, pp. 121-125.
17. R.A.Eremin, Kholmurodov Kh.T., Petrenko V.I., Rosta L., Grigoryeva N.A., Avdeev M.V. On the microstructure of organic solutions of mono-carboxylic acids: Combined study by infrared spectroscopy, small-angle neutron scattering and molecular dynamics simulations. Chemical Physics v. 461, pp. 1-10 (2015).
18. O.V.Tomchuk, Volkov D.S., Bulavin L.A., Rogachev A.V., Proskurnin M.A., Korobov M.V., Avdeev M.V. “Structural characteristics of aqueous dispersions of detonation nanodiamond and their aggregate fractions by small-angle neutron scattering”, Journal of Physical Chemistry C, v. 119, pp. 794-802 (2015).
19. M.V.Avdeev, Tomchuk O.V., Ivankov O.I., Alexenskii A.E., Dideikin A.T., Vul' A.Ya. On the structure of concentrated detonation nanodiamond hydrosols with a positive ζ potential: analysis of small-angle neutron scattering. Chemical Physics Letters, 2016, V. 658, P. 58-62.
20. Yu.I.Prylutskyy, Cherepanov V.V., Kostjukov V.V., Evstigneev M.P., Kyzyma O.A., Bulavin L.A., Ivankov O., Davidenko N.A. and Ritter U. Study of the complexation between Landomycin A and C60 fullerene in aqueous solution. RSC Adv., 2016, V. 6, pp. 81231-81236.
21. S.Prylutska, Panchuk R., Gołuński G., Skivka L., Prylutskyy Yu., Hurmach V., Skorokhyd N., Borowik A., Woziwodzka A., Piosik J., Kyzyma O., Haramus V., Bulavin L., Evstigneev

M., Buchelnikov A., Stoika R., Berger W., Ritter U., Scharff P. C60 fullerene enhances cisplatin anticancer activity and overcomes tumor cells drug resistance. Nano Res., 10(2) (2017) 652-671.

22. N.Jargalan, Tropin T.V., Avdeev M.V., Aksenov V.L., Investigation and modeling of evolution of UV-Vis spectra of C60/NMP solution. Nanosystems: physics, chemistry, mathematics, 7(1) (2016) 99-103.
23. M.V.Avdeev, Rulev A.A., Bodnarchuk V.I., Ushakova E.E., Petrenko V.I., Gapon I.V., Tomchuk O.V., Matveev V.A., Pleshanov N.A., Kataev E.Yu., Yashina L.V., Itkis D.M. Monitoring of Lithium Plating by Neutron Reflectometry. Applied Surface Science, (2017) in press.
24. T.B.Feldman, A.I.Ivankov, T.N.Murugova, A.I.Kuklin, P.V.Shelyakin, M.A.Yakovleva, V.I.Gordeliy, A.V.Belushkin, M.A.Ostrovsky "Study of visual pigment rhodopsin supramolecular organization in photoreceptor membrane by small-angle neutron scattering method with contrast variation", Proceedings of the Russian Academy of Sciences, v. 465, № 5, pp. 1-5, 2015 (in Russian).
25. I.M.Byvshev, Vangeli, I. M., Murugova, T. N., Ivankov, O. O., Kuklin, A. I., Popov, V. I., Yaguzhinsky, L. S. On the existence of two states of OXPHOS system supercomplex in heart mitochondria. Biochimica et Biophysica Acta - Bioenergetics, 1857, e35-e36 (2016).
26. M. Zhernenkov, D. Bolmatov, D. Soloviov, K. Zhernenkov, B. P. Toperverg, A. Cunsolo, A. Bosak & Y. Q. Cai. Revealing the mechanism of passive transport in lipid bilayers via phonon-mediated nanometre-scale density fluctuations. Nature Communications, 7, 1-9 (2016).
27. D.Lombardo, P.Calandra, D.Barreca, S.Magazu, M.A. Kiselev. Soft Interaction in Liposome Nanocarriers for Therapeutic Drug Delivery. Nanomaterials 6, 125 (2016).
28. N.Kučerka, Dushanov E., Kholmurodov Kh., Katsaras J., Uhríková D. Cation-containing lipid membranes – experiment and MD simulations. European Pharmaceutical Journal, 2016, accepted.
29. Ordon M., Yu.Gorshkova, M.Ossowska-Chruściel, Lithocholic acid derivative in the dimethyl sulfoxide presence: Morphology and phase transitions, Thermochimica Acta 643 (2016) 1–12.
30. Y.V.Kulvelis, S.S.Ivanchev, O.N.Primachenko, V.T.Lebedev, E.A.Marinenko, L.N.Ivanova, A.I.Kuklin, O.I.Ivankov, D.V.Soloviov, Structure and properties optimization of perfluorinated short side chain membranes for hydrogen fuel cells using orientation stretching. RSC Advances, 6, 108864–108875 (2016).
31. L.Bulavin, N.Kutsevol, V.Chumachenko, D.Soloviov, A.Kuklin, A.Marynin, SAXS Combined with UV-vis Spectroscopy and QELS: Accurate Characterization of Silver Sols Synthesized in Polymer Matrices. Nanoscale research letters, 11(1), 1-8 (2016).
32. T.V.Tropin, J.W.P.Schmelzer, V.L.Aksenov. Modern aspects of the kinetic theory of glass transition. Physics – Uspekhi, 59 (1) pp.42-66 (2016).
33. K. Łuczyńska, K. Drużbicki, K. Łyczko, J. Cz. Dobrowolski, 'Experimental (X-ray, 13C CP/MAS NMR, IR, RS, INS, THz) and Solid-State DFT Study on (1:1) Co-Crystal of Bromanilic Acid and 2,6- Dimethylpyrazine', Journal of Physical Chemistry B, v. 119, p. 6852-6872 (2015).
34. Ł. Hetmańczyk, D. Chudoba, A. Filarowski et al. To the question of conformational equilibrium and polymorph's states in the solid state and under the matrix condition. J. Chem. Phys., submitted (2016).
35. R.Keppler, Stipp, M., Behrmann, J.H., Ullemeyer, K. & Heidelbach, F. Deformation inside a

paleosubduction channel – Insights from microstructures and crystallographic preferred orientations of eclogites and metasediments from the Tauern Window, Austria. J. Struct. Geol. 82, 60-79 (2016).

36. T. Lychagina, & Nikolayev, D. Quantitative comparison of the measured crystallographic textures. J. Appl. Cryst. 49 (4), 1290-1299 (2016).
37. D. Nikolayev, & Lychagina, T., Zisman, A.A. & Yashina, E. Directly verifiable neutron diffraction technique to determine retained austenite in steel. Materials Science and Engineering A., submitted (2016).
38. Ch.Scheffzük, Müller, B.I.R., Breuer, S., Altangerel B. & Schilling, F.R. Applied Strain Investigation on Sandstone Samples Using Neutron Time-of-Flight Diffraction at the Strain Diffractometer EPSILON, IBR-2M Dubna. Mongolian J. Physics, submitted (2016).
39. S.Breuer, Schilling, F.R., Scheffzük, Ch. & Müller, B.I.R. Forward Modeling Neutron Time-of-Flight Diffraction Data for Uniaxial Load Conditions by Using the Example of Sandstone. J. Appl. Cryst., submitted (2016).
40. D.M.Itkis, Velasco-Velez J.J., Knop-Gericke A., Vyalikh A., Avdeev M.V., Yashina L.V., “Probing of electrochemical interfaces by photons and neutrons in operando”, ChemElectroChem, v. 2, p. 1427–1445 (2015).
41. A.M.Balagurov, A.I.Beskrovnyy, V.V.Zhuravlev, G.M.Mironova, I.A.Bobrikov, Д.Neov, S.G.Sheverev, Neutron diffractor for real-time studies of transient processes at the IBR-2 pulsed reactor. Journal of Surface Investigation, X-ray, Synchrotron and Neutron Techniques, v.10, i.3, (2016) pp. 467-479.
42. S.V.Kozhevnikov, V.K.Ignatovich, F.Radu, Neutron resonances in planar waveguides, JETP, 123 (6) (2016) 950-956.
43. E.V.Lukin, D.P. Kozlenko, S.E. Kichanov, A.V. Rutkauskas, G.D. Bokuchava, B.N. Savenko “First attempts on energy-selective neutron imaging at IBR-2”, Physics Procedia, v. 69 (2015), p. 271 - 274.

Appendix 1

List of organizations collaborating with the NICM Department.

Collaboration:

Country or international organiza tion	**City**	**Institute or Laboratory**
JINR	Dubna	BLTP, VBLHEP, LRB, FLNR, DLNP, LIT
Azerbaijan	Baku	IP ANAS, AzTU
Argentina	Bariloche	CAB CNEA
Belarus	Minsk	BSU, IAP NASB, INP BSU, SPMRC NASB, RI PCP BSU, NC PHEP BSU, RIPChP BSU
	Grodno	SUG
Bulgaria	Sofia	IMS BAS, ISSP BAS, IE BAS, IEES BAS, INRNE BAS
Czech Republic	Prague	CTU, IG ASCR, IMC ASCR, IP ASCR
	Rez	NPI ASCR
Egypt	Cairo	EAEA,CU
France	Grenoble	IBS
	Saclay	LLB
Germany	Berlin	HZB, BAM
	Bayreuth	Univ.
	Bochum	RUB
	Halle	MLU
	Hamburg	DESY
	Gottingen	Univ.
	Geesthacht	HZG
	Darmstadt	TU Darmstadt
	Dortmund	TU Dortmund
	Dresden	TU Drezden
	Kiel	CAU, IFM-GEOMAR
	Karlsruhe	KIT
	Leipzig	UoC
	Rostock	Univ.
	Stuttgart	MPI-FKF
	Freiberg	TUBAF, IMF TUBAF
	Julich	FZJ
Hungary	Budapest	Wigner RCP
	Szeged	US
India	Panchgaon	Amity Univ.
Italy	Trento	UniTn

Japan	Nagano	Shinshu Univ.
	Minato	Keio Univ.
Kazakhstan	Almaty	INP
	Rudny	RII
Latvia	Riga	ISSP UL, IPE
Moldova	Chisinau	IC ASM
Mongolia	Ulaanbaatar	IPT MAS, MUST
Norway	Trondheim	NGU
Poland	Warsaw	INCT
	Białystok	UB
	Wroclaw	WUT, UW
	Krakow	JU, NINP PAS, AGH
	Lublin	UMCS
	Poznan	AMU
	Седльце	UPH
	Szczecin	WPUT
Russia	Moscow	GC RAS, IA RAS, IBMC, IC RAS, IEPT RAS, IGEM RAS, IGIC RAS, IMET RAS, INMI RAS, IPCE RAS, ITEP, IPE RAS, ISPM RAS, NNRU “MEPhI”, MIET, MITHT, MSU, NIKIET, NRC KI, SINP MSU, SC “VNIINM”
	Moscow, Troitsk	HPPI RAS, ISAN, INR RAS
	Belgorod	BelSU
	Dolgoprudny	MIPT
	Gatchina	PNPI RAS
	Yekaterinburg	IMP UB RAS, USU
	Kazan	KSTU
	Kaliningrad	IKBFU
	Krasnoyarsk	IP SB RAS, SibFU
	Nizhny Novgorod	UNN, IPM RAS
	Perm	ICMM UrB RAS, ITCh UrB RAS
	Petrozavodsk	IG KarRC RAS
	Podolsk	GIDROPRESS
	Rostov-on-Don	RIP SFU
	St. Petersburg	IPTI RAS, SPbSU
	Sterlitamak	SSPI
	Tomsk	NPI TPU
	Tula	TSU
	Chernogolovka	ISSP RAS

Romania	Bucharest	IFIN-HH, INCDIE ICPE-CA, NIMP, ISS, UB, UPB, UMF, UTM
	Baia Mare	TUCN-NUCBM
	Constanța	UOC
	Craiova	UC
	Cluj-Napoca	I.N.C.D.T.I.M., RA BC-N, UBB
	Pitesti	SCN
	Timisoara	LMF CCTFA, UPT, UVT
	Iasi	NIRDTP, UAI, UAIC
Serbia	Belgrade	INS “VINCA”
	Novi Sad	UNS
Slovak Republic	Bratislava	CU
	Kosice	IEP SAS
South Africa	Pretoria	Necsa
Spain	Madrid	CENIM-CSIC
Switzerland	Villigen	PSI
	Zurich	ETH
Taiwan	Hsinchu	NSRRC
Tajikistan	Dushanbe	IChem ASRT
United Kingdom	Didcot	RAL
Ukraine	Kiev	IPMS NASU, NTSU, ISC NASU
	Kharkov	IERT NASU, KFTI NASU
	Donetsk	DonIPE NASU, DonNU
Uzbekistan	Tashkent	INP UAS
Vietnam	Hanoi	IOP VAST
	Da Nang	DTU

Appendix 2

List of prizes awarded to the Department employees in 2015 – 2017.

International prizes

Prize "Stefan Procopiu" of the Romanian Academy of Sciences in Physics, 2015, D.P. Kozlenko.

JINR Prizes

2015

I prize in nomination **'**Scientific and technical applied research' for a series of studies:

"Structure diagnostics and investigations of powders and liquid suspensions of detonation nanodiamonds by small angle scattering of thermal neutrons"

Authors: M.V. Avdeev, V.L.Aksenov, O.I. Ivankov, A.V. Rogachev, O.V. Tomchuk, L.A. Bulavin, L. Rosta, V.M. Garamus, N.N. Rozhkova, E. Osawa.

2016

I prize in nomination **'**Experimental Physics Research' for a series of studies:

"Magnetic phenomena in intermetallic compounds RCo2: studies of the limits of the itinerant electron metamagnetism concept"

Authors: D. Kozlenko, E. Lukin, S. Kichanov, A. Rutkauskas, B. Savenko, E. Burzo, P. Vlaic, Dang Ngoac Toan.

Appendix 3

List of grants allocated for investigations conducted in the Department in 2015-2017.

№	Organization	Period	Title	Leader
1.	RFBR	2014-2016	RFBR grant 14-02-00353 "Structural Mechanisms of Polymorphic Phase Transitions in Complex Molecular Crystals"	A.V. Belushkin
2.	RFBR	2015-2017	RFBR grant 15-02-03248 "Microscopic mechanisms for the realization of the magnetoelectric effect in oxide multiferroics: structural studies at high pressures"	D.P. Kozlenko
3.	IAEA	2012-2015	Research Contract “Development of Neutron Imaging Facility for Cultural Heritage Objects Analysis at the IBR-2 reactor”	D. P. Kozlenko
4.	RSF	2014-2016	Grant RNF 14-12-00896, "Real time - in situ neutron structural analysis of materials and processes in small-sized electric current sources",	A.M. Balagurov
5.	RFBR	2014-2016	RFBR grant 14-29-0409_ofi_m "Neutron and X-ray (synchrotron) complementary studies of the real structure of electrode materials",	A.M. Balagurov
6.	RFBR	2015	RFBR grant 15-33-51160_mol_nr "Application of the neutron diffraction method for studying ion transport processes and structural transformations in lithium intercalated complex oxides and phosphates of transition metals (Fe, Ti, V, Co, Mn)"	A.M. Balagurov
7.	RFBR	2014-2016	RFBR grant 14-42-03585_ r_centr_a "Neutron diagnostics of microstructure, defects and mechanical properties of functional and nanostructured construction materials"	G.D. Bokuchava
8.	RFBR	2015-2017	RFBR grant 15-08-06418_a "Application of neutron stress-diffractometry for investigations of residual stresses in construction materials and welded joints"	G.D. Bokuchava
9.	RFBR	2014-2016	RFBR grant 14-22-01054_ofi_m "Investigations of structural stability of biorelevant nanosystems, including magnetic systems, in bulk	M.V.Avdeev

			and interphases by synchrotron radiation and neutron scattering methods"	
10.	RSF	2014-2016	Grant RNF 14-12-00516 "Development of small-angle scattering methods and study of vesicles and nano-drugs on neutron and synchrotron sources"	M.A. Kiselev
11.	RFBR	2014-2016	RFBR grant 14-04-91333 NNIO_a "Investigations of the influence and functions of various subclasses of ceramides on the nanostructure and dynamics of model lipid membranes Stratum Corneum"	M.A. Kiselev
12.	RFBR	2014-2016	RFBR grant 14-02-00688 "Structure and permeability of lipid skin membranes - neutron and synchrotron studies"	M.A. Kiselev